



TECHNISCHE  
UNIVERSITÄT  
WIEN

## Dissertation

# The High-Entropy Concept for Ceramic Thin Films

carried out for the purpose of obtaining the degree of Dr.techn., submitted at TU  
Wien, Faculty of Mechanical and Industrial Engineering, by

**Dipl.-Ing. Alexander Kirnbauer**

Mat.Nr.: 1027195

Friedlbrunnngasse 14, 7301 Deutschkreutz, Austria

under the supervision of

Univ.Prof. Dipl.-Ing. Dr.mont. Paul Heinz Mayrhofer  
Institute of Materials Science and Technology, E308

Vienna, April 2020

*Reviewed by*

---

**Jochen Schneider**

Lehrstuhl für Werkstoffchemie

RWTH Aachen

Kopernikusstrasse 10,

52074 Aachen, Deutschland

---

**Robert Franz**

Lehrstuhl für funktionale Werkstoffe und  
Werkstoffsysteme

Montanuniversität Leoben

Roseggerstraße 12 / Max-Tendler-Straße 9,

8700 Leoben

This work was supported by the Austrian COMET Program (project K2 XTribology, no. 849109 and project K2 InTribology, no. 872176) and Plansee Composite Materials GmbH.

### *Affidavit*

I declare in lieu of oath, that I wrote this thesis and performed the associated research myself, using only literature cited in this volume.

---

*Date*

---

*Signature*

# Acknowledgements

I would like to express my sincerest gratitude to **Univ.Prof. Paul Heinz Mayrhofer** for giving me the chance to write a PhD Thesis within his research group. It is an exceptional honour to be part of Paul's group for about 7 years now and I am very glad to have such a great and distinguished person not just as group leader and supervisor but also as a friend. It was a pleasure to work under your guidance and I am thankful for all the discussions at 7am or even earlier whether regarding research or private things. Thank you, **Paul**.

I would also like to thank **Christian** Koller for his help during the last three years. Although he left the university he always had time to discuss results, help me with the interpretation of results and the exhausting work of writing manuscripts. Thank you Christian for your help and friendship over the last 7 years.

Another big "Thank You" goes to **Helmut** Riedl, although I am not part of your CD-Lab you always had time to discuss ongoing work, facility issues, ideas for investigations as well as results. Thanks for your help your guidance and your friendship not just during the work but also outside the university.

Thanks to **Rainer** Hahn, my former office colleague, who always had some interesting ideas not just regarding materials science. Thanks for the fruitful discussions the help with computer software, data analysis and of course fracture toughness tests. Last but not least thank you also for your friendship I had a really great time with you in the past 6 years.

A really big "Thank You" goes to **Philipp** Ertelthaler and **Stefan** Rißlegger, without you two our lab, the facilities, and the "Klinkerbeidrunde" would not be the same. I would even say nothing of it would work as perfect as it does with you! Thanks to both of you for your help with "Ylvi"- and "Senta"- services and everything else that you fixed for all of us in our lab. Also, I want to thank you for your friendship, the afterwork beers, and the nights out, sometimes lasting to the next morning.

Thanks to **Lukas “LukiLuki” Zauner** for your help whenever I needed some support. The lab work is much more fun if you are part of it. Thank you for all your help and the great time after work when you became “**SchlukiLuki**” :-).

Thank you to all my current and former colleagues **Bernhard, Elias, Fedor, Matthias, Vincent, Andreas, Antonia, Christoph, Julian, Lukas L., Nikola, Oliver, Stefan K., Thomas G.**, and the whole **Thin Film Materials Science Division**, I had a great time with you during work, at conferences as well as after work and at every party we had in the last years.

I would also like to thank my dedicated bachelor students, **Bernhard** Girsule, **Christoph** Spadt, **Lena** Dorner and **Matthias** Selinger. Although, the work and coordination were not always easy I had a great time with all of you.

Most importantly, I would like to thank my **parents** and my whole **family** for their support during my whole studies, and especially in the tough times during my PhD Thesis. Last but not least, I would like to thank all my friends, especially from the “Musikverein Deutschkreutz” the time with you, at weddings, “Blasmusiktreffen” or “Frühschoppen” was always great and let me, at least for some time, not think about work and deadlines. And not to forget my contemporaries of the “Gummibärenbande 07”, our annual “Glühweinausschank” and the skiing holiday have always been amazing.

# Table of Contents

<b>Abstract</b> .....	<b>I</b>
<b>Kurzfassung</b> .....	<b>III</b>
<b>List of Figures</b> .....	<b>V</b>
<b>List of Abbreviations and Symbols</b> .....	<b>VIII</b>
<b>1 Introduction</b> .....	<b>1</b>
<b>2 Theoretical Background</b> .....	<b>3</b>
2.1 Thermodynamic Basics .....	3
2.2 Material Properties .....	7
2.2.1 Chemical Bonding.....	7
2.2.2 Defects.....	9
2.3 Strengthening Mechanisms.....	14
2.3.1 Strain Hardening .....	14
2.3.2 Solid Solution Strengthening .....	15
2.3.3 Precipitation Hardening .....	16
2.3.4 Grain Refinement Strengthening .....	17
2.4 Diffusion .....	18
2.5 Softening Mechanisms.....	20
2.5.1 Recovery .....	21
2.5.2 Recrystallisation .....	21
2.6 Thermal Stability.....	22
2.6.1 Decomposition .....	22
2.6.2 Oxidation .....	24
<b>3 Material Systems</b> .....	<b>27</b>
3.1 High-Entropy Alloys .....	27
3.2 Transition Metal Nitrides .....	29
3.3 Transition Metal Borides.....	30

3.4	Transition Metal Oxides .....	31
3.5	High-Entropy Ceramics .....	32
<b>4</b>	<b>Deposition of Thin Films.....</b>	<b>34</b>
4.1	Physical Vapour Deposition.....	34
4.1.1	Magnetron Sputtering .....	36
4.1.2	Cathodic Arc Evaporation .....	38
4.2	Nucleation and Growth.....	39
4.3	Structure Zone Diagram .....	42
<b>5</b>	<b>Investigative Methods.....</b>	<b>45</b>
5.1	Structural Analyses .....	45
5.1.1	X-Ray Diffraction .....	45
5.1.2	Electron Microscopy.....	48
5.1.2.1	Scanning Electron Microscopy .....	48
5.1.2.2	Transmission Electron Microscopy.....	50
5.2	Chemical Analyses .....	52
5.2.1	Energy Dispersive X-Ray Spectroscopy .....	52
5.2.2	Atom Probe Tomography .....	53
5.3	Mechanical Investigations.....	54
5.3.1	Nanoindentation .....	55
5.3.2	Micro-Cantilever Bending Tests.....	56
5.4	Thermal Analyses.....	57
5.4.1	Vacuum Annealing .....	57
5.4.2	Differential Scanning Calorimetry.....	58
<b>6</b>	<b>References.....</b>	<b>59</b>
<b>7</b>	<b>Contribution to the Field.....</b>	<b>66</b>
7.1	First Author Publications.....	66
7.2	Thesis-Related Co-Author Publications .....	69
7.3	Further First Author Publication.....	70

<b>8</b>	<b>Publications.....</b>	<b>71</b>
	<b>Publication I: Mechanical properties and thermal stability of reactively sputtered multi-principal-metal Hf-Ta-Ti-V-Zr nitrides.....</b>	<b>72</b>
	<b>Publication II: Toughness of Si alloyed high-entropy nitride coatings.....</b>	<b>82</b>
	<b>Publication III: High-entropy oxide thin films based on Al-Cr-Nb-Ta-Ti.....</b>	<b>86</b>
	<b>Publication IV: Thermal stability and mechanical properties of sputtered (Hf,Ta,V,W,Zr)-diborides.....</b>	<b>92</b>
	<b>Publication V: High entropy ceramic thin films; A case study on transition metal diborides.....</b>	<b>103</b>

# Abstract

The utilisation of hard protective coatings is a growing topic in the field of materials science. Among the reams of possible material combinations, transition metal nitrides (TMNs) are commonly used for thin films in industry to protect tools, or surfaces, which are subject to harmful environmental conditions. Within this class of materials, TiN, TiAlN, and CrAlN can be considered the most important. Nevertheless, forming quaternary compounds, especially with refractory metals like Ta, Mo, or W proved to be a successful strategy to improve TMNs with respect to their thermal stability, oxidation resistance, and tribological properties. Additionally, borides of transition metals are also in the focus of research as they exhibit outstanding mechanical properties like high melting points and superhardness ( $H > 40$  GPa). Furthermore, also oxide coatings are investigated as they are promising candidates as oxidation resistant coatings.

A novel alloying concept, so-called high-entropy alloys (HEAs), has gained particular attention within the last decade. Such materials are defined as alloys with five principal elements in equiatomic or near-equiatomic composition, leading to a configurational entropy of at least  $1.5R$  ( $R$  being the universal gas constant). Due to this special composition, compared to conventional alloys (one principal element and several minor elements), properties, like hardness, strength, and toughness are often superior to those of conventional alloys. In parallel to HEAs, also high-entropy ceramics (HECs) moved into the focus of research. These consist of a solid solution of 5 or more binary nitrides, carbides, oxides, or borides and are believed to exhibit enhanced properties due to the four core effects of HEAs (high entropy; lattice distortion; sluggish diffusion; and cocktail effect). The main subject of this thesis is the investigation of structure and mechanical properties of thin films based on the high-entropy materials concept, with particular emphasis on the thermal stability—which, according to the Gibbs free energy, should be improved in the high temperature regime.

In this PhD thesis the high-entropy concept applied to nitride, boride, and oxide thin films is investigated. All the coatings investigated were synthesised by (reactive) magnetron sputtering using a single powder-metallurgically produced target, with an equimolar composition of the respective elements or compounds. For the investigation of nitrides, the targets consisted of (Hf, Ta, Ti, V, Zr) or (Al, Ta, Ti, V, Zr) and were sputtered in a mixture of Ar and  $N_2$ . The boride coatings were prepared either using a compound target consisting of ( $HfB_2$ ,  $TaB_2$ ,  $VB_2$ ,  $W_2B_5$ ,  $ZrB_2$ ) or using a  $ZrB_2$  target and placing pieces of  $HfB_2$ ,  $TaB_2$ ,  $TiB_2$ ,  $VB_2$  on the racetrack. Furthermore, oxide coatings



were prepared using a target consisting (Al, Cr, Nb, Ta, Ti) which was sputtered in a mixture of Ar and O<sub>2</sub>. All the coatings were investigated by X-ray diffraction (XRD), scanning electron microscopy, and nanoindentation. Additionally, vacuum annealing treatments and subsequent XRD and nanoindentation were carried out for every material system. Detailed investigations by transmission electron microscopy (TEM) and atom probe tomography were done for (Hf,Ta,Ti,V,Zr)N and (Hf,Ta,V,W,Zr)B<sub>2</sub>.

The results show that all the investigated material systems are relatively insensitive to the change of deposition parameters, like reactive gas flow, bias voltage, and substrate temperature. This is especially noteworthy for the oxides, as commonly used oxide coatings such as (Al,Cr)<sub>2</sub>O<sub>3</sub> show a strong dependency on the oxygen flow rate ratio regarding their structure and properties. The mechanical properties, of all the coatings in as-deposited state, show values comparable to binary or ternary coatings. Nevertheless, all investigated materials systems show enhanced thermal stability compared to their respective constituent binaries or ternaries. The structural stability as well as the hardness can be maintained to significantly higher temperatures, leading to the conclusion that diffusion driven processes are strongly retarded in ceramics with a high-entropy metals sublattice.

# Kurzfassung

Die Nutzung von Hartstoffschichten, hergestellt mittels physikalischer Dampfphasenabscheidung (engl.: physical vapour deposition (PVD)), als Schutz für Werkzeuge und Komponenten in Hochtemperaturanwendungen ist ein wachsendes Feld im Bereich der Werkstoffwissenschaften. Von den unzähligen möglichen Schichtzusammensetzungen, haben sich Nitride der Übergangsmetalle (engl.: transition metal nitrides, TMNs) als eine der am weitest verbreiteten Materialklassen herausgestellt. Solche Nitride werden vor allem für Schneidwerkzeuge und zum Schutz von Komponenten die in schädlichen Umgebungen eingesetzt werden verwendet. Innerhalb der Klasse der Nitride haben sich Titanitrid und Titanaluminiumnitrid basierte Schichten in der industriellen Anwendung etabliert. Das hinzulegieren von Refraktärmetallen, wie z.B.: Ta, Mo, oder W zeigte sich als erfolgreiche Strategie zur weiteren Verbesserung, hinsichtlich der Härte, der thermischen Stabilität sowie der Oxidationsbeständigkeit der genannten Nitride. Zusätzlich zu Nitriden, gelangen auch Boride der Übergangsmetalle immer mehr in den Fokus der Forschung, da diese sehr hohe Härte, hohe Schmelzpunkte und damit hohe Temperaturbeständigkeit besitzen. Zudem werden auch Oxidschichten die mittels PVD hergestellt werden als Oxidationsschutz verwendet.

In den letzten 15 Jahren hat sich ein neues Legierungskonzept, sogenannte Hochentropielegierungen, in der Forschung als neues Feld etabliert. Diese Legierungen setzen sich aus mindestens 5 Elementen zu gleichen oder nahezu gleichen Anteilen zusammen. Die gleiche Verteilung der Elemente, führt bei Legierungen zu einer Konfigurationsentropie von  $1.5R$ , wobei  $R$  die universelle Gaskonstante ist. Diese spezielle Zusammensetzung und die daraus resultierende hohe Konfigurationsentropie, führt im Weiteren zu verbesserten Eigenschaften wie hoher Härte, hoher Temperaturbeständigkeit und guter Oxidationsbeständigkeit solcher Legierungen, im Vergleich zu konventionellen Legierungen die aus einem oder zwei Hauptelementen bestehen.

Parallel zu Hochentropielegierungen werden auch Hochentropiekeramiken untersucht. Diese setzen sich aus 5 binären Keramiken wie z.B.: Nitriden, Carbiden, Oxiden oder Boriden die ebenfalls aufgrund ihrer speziellen chemischen Zusammensetzung besondere Eigenschaften aufweisen können da diese ebenfalls von den 4 Kerneffekten von Hochentropielegierungen (Hochentropieeffekt, starke Gitterverzerrung, träge Diffusion, und der sogenannte Cocktail-Effekt) profitieren.

Das Ziel dieser Dissertation ist es, das Hochentropiekonzept auf Nitride, Oxide und Boride die mittels PVD hergestellt werden anzuwenden und diese hinsichtlich ihrer thermischen Stabilität und mechanischen Eigenschaften zu untersuchen. Alle Schichten die untersucht wurden, wurden mittel (reaktivem) Magnetronspütern, unter der Verwendung von einem pulvermetallurgisch hergestellten Target, synthetisiert. Für die Untersuchungen an Nitride wurden Targets aus (Hf,Ta,Ti,V,Zr) und (Al,Ta,Ti,V,Zr) in jeweils äquiomarer Zusammensetzung verwendet und in einer Gasmischung aus Argon und Stickstoff zerstäubt. Die untersuchten Oxide wurden aus einem Target bestehend aus (Al;Cr,Nb,Ta,Ti) in einer Atmosphäre aus Argon und Sauerstoff hergestellt. Weiters wurden Boride entweder aus einem einzelnen pulvermetallurgisch hergestellten Target bestehend aus (HfB<sub>2</sub>, TaB<sub>2</sub>, VB<sub>2</sub>, W<sub>2</sub>B<sub>5</sub>, ZrB<sub>2</sub>) bzw. durch platzieren von HfB<sub>2</sub>, TaB<sub>2</sub>, TiB<sub>2</sub>, VB<sub>2</sub> Stücken auf dem Sputtergraben eines ZrB<sub>2</sub> Target. Alle hergestellten Schichten wurden mittel Röntgendiffraktion, Rasterelektronenmikroskopie, Transmissionselektronenmikroskopie und Nanohärtemessungen untersucht. Weiters wurden ausgewählte Proben mittels elastischer Rückstreuungsanalyse, sowie Atomsondentomographie im Detail untersucht.

Die Ergebnisse aller untersuchten Schichten, zeigen, dass die Herstellung von Hochentropiekeramiken wenig durch das ändern von Beschichtungsparametern, wie Substrattemperatur, Bias-Spannung oder Reaktivgasfluss, beeinflusst wird. Das ist vor allem im Bereich der Oxide erwähnenswert, da die Struktur und Eigenschaften von konventionell angewendeten Oxiden wie (Al,Cr)<sub>2</sub>O<sub>3</sub> eine signifikante Abhängigkeit der Beschichtungsparameter zeigen. Auch wenn die mechanischen Eigenschaften direkt nach der Herstellung vergleichbar mit jenen von binären oder ternären Schichten ist, zeigt sich nach der Wärmebehandlung durch Vakuumglühen, dass alle untersuchten Schichten signifikant verbesserte Härtewerte und Struktureigenschaften. Diese erhöhte thermische Stabilität lässt sich auf die träge Diffusion, die aufgrund des hochentropischen Metalluntergitters in diesen Materialien herrscht, zurückführen.

# List of Figures

Fig. 1: Illustration of Gibbs free energy depending on the arrangement of atoms showing a metastable (position B) and a stable (position A) system, taken with the permission of [50].	4
Fig. 2: Schematic illustration of the evolution of Gibbs free energy $\Delta G_{\text{mix}}$ for negative (a and b) and positive enthalpy of mixing $\Delta H_{\text{mix}}$ (c and d) and different $-T\Delta S$ values (high and low temperatures), adapted from [50].	6
Fig. 3: Classification of hard ceramic materials according to their bonding character, taken with permission from [50].	8
Fig. 4: Illustration of the three main bonding types: metallic bonding, ionic bonding, and covalent bonding, taken with permission from [50], originally from [51].	9
Fig. 5: Illustration of point defects (a) vacancy, (b) smaller substitutional atom, (c) larger substitutional atom, (d) smaller interstitial atom, and (e) larger interstitial atom, redrawn with permission from [52].	10
Fig. 6: Illustration of line defects: (a and c) edge dislocation and (b and d) screw dislocation, redrawn with permission from [52].	11
Fig. 7: Schematic illustration of (a) an edge dislocation and (b) a screw dislocation with relative orientations of dislocation line and Burgers vector, redrawn with permission from [52].	12
Fig. 8: Illustration of 2-dimensional lattice defects including: grain boundaries, phase boundaries, and stacking faults, taken with permission from [52].	13
Fig. 9: Illustration of solid solutions (a) interstitial solid solution, (b) substitutional solid solution, and (c) ordered solid solution, reproduced with permission from [52].	15
Fig. 10: Schematic illustration of grain refinement hardening by the Hall-Petch effect, redrawn after [55].	17
Fig. 11: Illustration of different diffusion mechanisms (a) substitutional mechanism and ring mechanism and (b) interstitial mechanism, reconstructed with permission from [52].	18
Fig. 12: Schematic binary phase diagram A–B with a distinct miscibility gap and the corresponding trend of the Gibbs free energy at a certain temperature T, adapted from [50], originally from [64,65].	23
Fig. 13: Evolution of chemical composition during decomposition by nucleation and growth (left) and spinodal decomposition (right) taken with permission from [50].	24

Fig. 14: Schematic illustration of diffusion-controlled oxide scale growth. $M^{n+}$ indicating metal cations, $V^{n-}$ cation vacancies, $e^-$ electrons, $h^+$ electron holes, and $O^{2-}$ oxygen anions [66], originally from [67].	25
Fig. 15: Illustration of different rate laws relevant for oxidation of metals and films, taken with permission from [50], originally from [71].	26
Fig. 16: Schematic illustration of NaCl-structured TMNs showing the fcc sublattice occupied by the transition metal (blue spheres) and the octahedral interstices occupied by nitrogen (yellow spheres), visualised with VESTA [96,97].	30
Fig. 17: Schematic illustration of a) $\alpha$ - $AlB_2$ - structure (B, grey spheres and Al, red spheres) b) $\omega$ - $W_2B_5$ -structure (B, grey spheres and W, green spheres) adapted from [43].	31
Fig. 18: Schematic illustration of (a) $\alpha$ - $Al_2O_3$ -structure (Al, blue spheres and O, red spheres) and (b) rutile- $TiO_2$ -structure (Ti, grey spheres and O, red spheres).	32
Fig. 19: Schematic voltage-current characteristics for plasma discharge PVD relevant regimes are marked with grey background, taken with permission from [50], originally from [125].	35
Fig. 20: Schematic illustration of a magnetron sputter process, taken with permission from [126].	37
Fig. 21: Schematic illustration of an arc evaporation process including essential components, taken with permission from [50].	38
Fig. 22: Schematic diagram of the trends of the various contributors of the Gibbs free energy in respect of the nucleus radius.	40
Fig. 23: Illustration of the three basic growth modes occurring in thin films: (a) Frank-van der Merwe, (b) Volmer-Weber, and (c) Stranski-Krastanov adapted from [125].	42
Fig. 24: Structure zone diagrams after a) Messier[129] and b) Thornton [130], adapted from [50].	43
Fig. 25: Advanced structure zone diagram according to Anders [133].	44
Fig. 26: Schematic illustration of the two most common XRD arrangements used to investigate thin films and powders, Bragg-Brentano (left) and Grazing Incidence (right), taken with permission from [50].	46
Fig. 27: Schematic illustration of a XRD pattern including basic information used to determine crystal structure, lattice parameters, phase composition, and grain size, taken with permission from [50], originally from [136].	47
Fig. 28: Illustration of the basic setup of a scanning electron microscope [138].	49

---

Fig. 29: Schematic illustration of basic electron-matter interaction processes during SEM investigations, taken with permission from [50], originally from [139]. .....49

Fig. 30: Illustration of two TEM operation modes a) electron diffraction and b) bright field imaging taken with permission from [50], originally from [140]. .....51

Fig. 31: Schematic illustration of electron atom interaction (left) and characteristic X-rays depending on the energy loss of the incident beam with energy  $E_0$  (right) taken with permission from [50], originally from [139]. .....52

Fig. 32: Illustration of the basic components and the operating principle of atom probe tomography, adapted from [141]. .....54

Fig. 33: Schematic illustration of a load-displacement curve of a nanoindentation test,  $P_{max}$  indicating the maximum load applied at the highest indentation depth  $h_{max}$ , and  $h_r$  being the residual displacement taken with permission from [50], originally from [142]. .....55

Fig. 34: SEM images of a micro-cantilever bending test (a) free-standing cantilever with initial notch and picoindenter and (b) cross-section of fractured cantilever .....56

Fig. 35: Schematic illustration of a standard annealing treatment cycle. ....57

# List of Abbreviations and Symbols

APT.....	Atom probe tomography
BB.....	Bragg-Brentano
BF.....	Bright field
CAE.....	Cathodic arc evaporation
CCA.....	Complex concentrated alloys
CCD.....	Charge-coupled device
CVD.....	Chemical vapour deposition
EDS.....	Energy dispersive X-ray spectroscopy
FIB.....	Focused ion beam
GID.....	Grazing incidence diffraction
HEA.....	High-entropy alloys
HEB.....	High-entropy borides
HEN.....	High-entropy nitrides
HEO.....	High-entropy oxides
PVD.....	Physical vapour deposition
SAED.....	Selected area electron diffraction
SEM.....	Scanning electron microscope
SZD.....	Structure zoned diagram
TEM.....	Transmission electron microscope
TMB.....	Transition metal borides
TMN.....	Transition metal nitride
TMO.....	Transition metal oxides
XRD.....	X-ray diffraction
b.....	Burgers vector (m)
c.....	Speed of light (m/s)
d.....	Grain size (m)
d.....	Resolution (m)
d.....	Spacing between atomic lattice planes (m)
h.....	Planck constant (Js)
k.....	Boltzmann constant (J/K)
n.....	Refraction index (-)
n.....	Integer (-)
p.....	Pressure (Pa)
r.....	Particle radius (m)
r*.....	Critical particle radius (m)
w.....	Probability of occurrence of a microstate (-)
x <sub>i</sub> .....	Mole fraction of i-th element (%)

$\alpha$ .....	Half Aperture Angle ( $^{\circ}$ )
$\gamma$ .....	Surface energy ( $\text{J/m}^2$ )
$\epsilon$ .....	Strain (%)
$\theta$ .....	Diffraction angle ( $^{\circ}$ )
$\lambda$ .....	Wave length (m)
$\nu$ .....	Frequency (1/s)
$\rho$ .....	Dislocation density ( $1/\text{m}^2$ )
$\sigma$ .....	Tensile stress (Pa)
$\tau$ .....	Shear stress (Pa)
$\tau_0$ .....	Peierls stress (Pa)
D.....	Diffusion coefficient ( $\text{m}^2/\text{s}$ )
$D_0$ .....	Diffusion constant ( $\text{m}^2/\text{s}$ )
E.....	Young's modulus (Pa)
G.....	Gibbs free energy (J) or (J/mol) *
$G_{\text{mix}}$ .....	Gibbs free energy of mixing (J/mol) *
G.....	Shear modulus (Pa)
$G_N$ .....	Nucleation energy (J)
$G_S$ .....	Energy needed for formation of new surface (J)
$G_V$ .....	Energy gain by formation of new volume ( $\text{J/m}^3$ )
H.....	Enthalpy (J) or (J/mol) *
$H_{\text{mix}}$ .....	Mixing enthalpy (J/mol) *
N.....	Number of atomic lattice sites (-)
$N_V$ .....	Number of equilibrium vacancies (-)
$Q_D$ .....	Activation energy for diffusion (J/mol)
$Q_V$ .....	Formation energy of one vacancy (J/mol)
R.....	Universal gas constant (J/mol K)
S.....	Entropy (J/K) or (J/mol K) *
$S_{\text{mix}}$ .....	Mixing entropy (J/mol K) *
$S_{\text{config}}$ .....	Configurational entropy (J/K) or (J/mol K) *
T.....	Absolute temperature (K)
U.....	Internal energy (J/mol) *
V.....	Volume ( $\text{m}^3/\text{mol}$ ) *

\* For simplicity reasons every symbol is written in capital letters and no difference between extensive and intensive physical quantities is made



# 1 Introduction

The demand on materials, which can extend the lifetime of tools and components, is everlasting. The aim to improve the performance of tools is always present since humankind first developed tools. Beginning in the stone age humans started to improve their tools and weapons to increase productivity and to defend their selves against enemies or wild animals using stone and wood. With increasing performance of the tools, native metals like gold, silver and copper were used to make decoration and especially copper was used for tools and weapons. With the first alloy, namely bronze, a first milestone in improving materials by alloying was set. The next significant milestone in the development and enhancement of the performance of tools started with mining and converting iron ore to iron. This was the basement for the invention of steel the most important alloy in history. Since this time the concept of alloying, to enhance the performance of bulk materials regarding their hardness, toughness, and workability, is omnipresent. Not just steel but in the last 40 years also Al, Ti, or Ni are improved by alloying and therefore converted to extreme temperature resistant, tough or hard materials.

Within the last two decades a completely new concept of alloying was developed. Whereas conventional alloys like the aforementioned bronze, steel, Al-, Ti-, or Ni-base alloys consist, of one predominant element and several others in a minor composition, recently developed alloys consist of multi-principal elements. These multi-principal element or multicomponent alloys also known as high-entropy alloys, which were invented in the past 15 years, contain 5 or even more elements in an equiatomic or at least near-equiatomic composition [1–3]. Therefore, these alloys exhibit outstanding properties, like hardness, yield strength, or fracture toughness compared to alloys based on one or two metals [1, 4–16].

To further improve the performance of bulk materials, the surface can be modified by applying hard protective coatings. The application of protective coatings is nowadays a well-established approach to improve the properties and increase the lifetime of tools and components and thereby also the efficiency. Especially cutting tools and components for high-temperature applications, such as gas turbine blades or combustion engine pistons, are subject to oxidation, corrosion and/or mechanical load. Very common and widely applied coatings for such applications are Ti-Al – based

nitrides [17,18]. Such nitrides have been studied and improved over several decades by adding refractory metals such as Mo [19,20], Ta [21–24], W [25], and Zr [26]. Furthermore, the addition of rare earth metals such as La and Ce can improve the thermal stability and the oxidation resistance of these coatings [27,28]. As observed from further studies, alloying helps to further improve the properties of TMNs. Therefore, also the high-entropy concept was applied to nitrides by Chen et al. [29], which was then also picked up by many other researchers [30–37].

Another group of materials used as protective coatings and in high-temperature applications are transition metal borides (TMB), which count to the class of ultra-high temperature ceramics [38–40]. Many TMBs exhibit superhardness ( $H > 40$  GPa) which make them very suitable as protective coatings for cutting applications. Therefore, binary or even ternary TMBs have gained attraction in the field of thin film materials research [41–44]. Nevertheless, these materials have to be further improved regarding their oxidation resistance to broaden the field of possible applications.

The last group of ceramic coatings applied as protection for bulk materials are (transition metal) oxides. These materials are very useful to protect bulk materials against oxidation, as they are the most effective diffusion barriers for oxygen if they exhibit a dense microstructure. Especially,  $\alpha$ - $\text{Al}_2\text{O}_3$  exhibits outstanding chemical, mechanical, and thermal properties [45–48]. Although, alumina thin films are very suitable as protective coatings their synthesis is very difficult and just possible at rather high temperatures which might not be possible for temperature sensitive substrates.

The scope of this thesis is to combine the two above-mentioned material concepts, namely high-entropy alloys and PVD coatings. The aim is to enhance the performance of hard coatings by applying the high-entropy concept and the accompanied core effects on one hand and obtaining advantages of coating deposition also into high-entropy materials on the other hand. Therefore, several coatings were deposited by magnetron sputtering. Within this thesis several different nitrides, oxides, and borides were synthesised in a lab-scaled sputter deposition facility and investigated regarding their mechanical properties and thermal stability.

## 2 Theoretical Background

To get a better understanding of the presented results and the relationship between different material properties and their dependency on bonding states, defects, temperature, and exposure to oxygen, the most important factors and properties will be described by the following subchapters.

### 2.1 Thermodynamic Basics

The stability of certain phases of materials can basically be explained by the Gibbs free-energy:

$$G = H - TS \quad \text{Eq. 1}$$

In *Eq. 1*,  $G$  is the Gibbs free-energy,  $H$  the free enthalpy,  $T$  the absolute temperature and  $S$  the entropy.

The enthalpy  $H$  can be described as the sum of the internal energy  $U$ —being the energy required to create the system—and the system's pressure multiplied by its volume [49], compare *Eq. 2*.

$$H = U + pV \quad \text{Eq. 2}$$

Basically, a system can be considered to be stable if the Gibbs free energy has a minimum. In this regard it has to be differentiated between a stable system and a metastable system. A metastable state is characterised by a local minimum of  $G$  which occurs when the first derivative  $dG = 0$  but not being the lowest energy state of the system, position B in Fig. 1. The global minimum of a system, position A in Fig. 1, represents the stable state of the system. If a system is in a metastable state it has to overcome a certain energy barrier (e.g. in form of temperature input) to reach the stable state, compare Fig. 1.

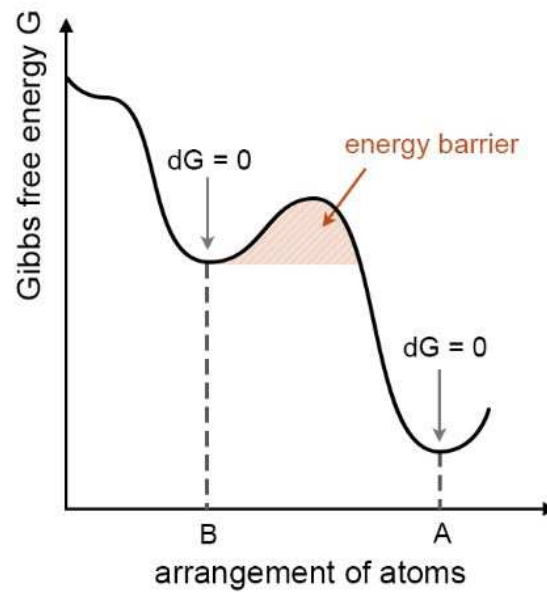


Fig. 1: Illustration of Gibbs free energy depending on the arrangement of atoms showing a metastable (position B) and a stable (position A) system, taken with the permission of [50].

Especially by PVD phases in a metastable state can easily be synthesised because of the high prevailing cooling rates. However, during annealing or input of heat by the application of, e.g. cutting tools, the desired metastable phase will transform into its stable one and therefore change the properties of the material.

The transformation from one phase to another always leads to a decrease in Gibbs free energy:

$$\Delta G = G_2 - G_1 < 0 \quad \text{Eq. 3}$$

Considering the mixture of two species A and B the of a certain phase can be estimated by the Gibbs free energy of mixing:

$$\Delta G_{mix} = G_2 - G_1 \quad \text{Eq. 4}$$

Combining Eq. 1 and Eq. 4, leads to:

$$\Delta G_{mix} = \Delta H_{mix} - T\Delta S_{mix} \quad \text{Eq. 5}$$

The entropy basically describes the disorder of a system. The higher the degree of disorder, the higher is the entropy of a certain phase. By mixing several elements the disorder of the system increases meaning the mixing entropy  $\Delta S_{mix}$  is always positive and therefore, the term  $T\Delta S_{mix}$  always contributes to a stabilisation of the system which increases with increasing temperature. There are several terms which contribute to the overall mixing entropy, namely the configurational entropy, the vibrational entropy, magnetic dipole, and electronic randomness. As the configurational entropy is the predominant term of the overall entropy it can be assumed that:

$$\Delta S_{mix} \approx \Delta S_{config} \quad \text{Eq. 6}$$

Considering that the mixing entropy is nearly equal the configurational entropy the entropy difference of two systems (phases) can easily be calculated by the Boltzmann equation:

$$S_{config} = k \ln w \quad \text{Eq. 7}$$

In *Eq. 7*,  $k$  is the Boltzmann constant and  $w$  are the possibilities in which the atoms can be arranged within a certain system. Thus, considering the chemical composition, the configurational entropy of a system of  $n$  elements with a mole fraction of  $x_i$  can be calculated by:

$$S_{config} = -R \sum_{i=1}^n x_i \ln x_i \quad \text{Eq. 8}$$

Considering *Eq. 8*, where  $R$  is the universal gas constant and  $x_i$  the molar fraction of the elements, it is clear that for a mixture of  $n$  elements the configurational entropy reaches its maximum for an equimolar composition.

Coming back to the stability of certain phase also the difference of the respective enthalpies,  $\Delta H_{mix}$ , which can be positive or negative, has to be considered. It is defined as the energy released or absorbed when mixing element A and B. Thus, negative values for the mixing enthalpy describe an exothermic reaction, whereas positive values indicate that energy has to be provided (endothermic reaction). More precisely, the enthalpy describes which chemical bonds, either bonds between A

and B ( $H_{AB}$ ) or bonds between the same species ( $H_{AA}$ ,  $H_{BB}$ ), are energetically more favourable. Therefore, the mixing enthalpy can be calculated as follows:

$$\Delta H_{mix} = H_{AB} - \frac{1}{2}(H_{AA} + H_{BB}) \quad \text{Eq. 9}$$

Considering these equations, it is possible to distinguish between four different cases of the behaviour of  $\Delta G_{mix}$  depending on  $\Delta H_{mix}$  (positive or negative) and  $\Delta S_{mix}$  together with the prevailing temperature, see Fig. 2.

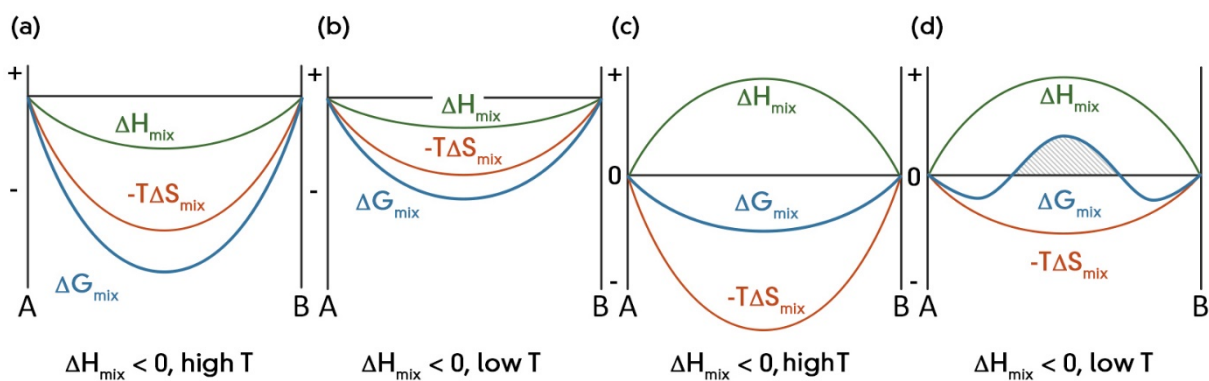


Fig. 2: Schematic illustration of the evolution of Gibbs free energy  $\Delta G_{mix}$  for negative (a and b) and positive enthalpy of mixing  $\Delta H_{mix}$  (c and d) and different  $-T\Delta S$  values (high and low temperatures), adapted from [50].

As the term  $-T\Delta S_{mix}$  is always negative and therefore contributes to a stabilisation of the system it is obvious that for negative values of  $\Delta H_{mix}$ , Fig. 2a and b, the system is always stable independent of the temperature. In contrast if the values of  $\Delta H_{mix}$  are positive the stability of a system strongly depends on the prevailing temperature. In the case of a high temperature, the term  $-T\Delta S_{mix}$  can “win” against the mixing enthalpy and therefore stabilise the system over the whole compositional range, Fig. 2c. If the temperature is low, it might be that there are compositions where the  $\Delta H_{mix}$  term is larger than  $-T\Delta S_{mix}$  leading to a sinusoidal form of  $\Delta G_{mix}$  and a certain compositional range where the system is metastable or unstable, see Fig. 2d. This compositional range, indicated by the grey shaded area in Fig. 2d, represents the miscibility gap of A and B for a certain temperature. Within this area the mixture of A and B is unstable at the given temperature, leading to a decomposition into two stable phases with different compositions than the primary phase.

## 2.2 Material Properties

Different materials exhibit different properties such as hardness, toughness, electrical conductivity, thermal conductivity, and many more. All of them are strongly depending on the atomic structure and the bonding type of the elements or compounds. Therefore, different material classes can be defined according to their preferred bonding state. Additional to the bonding state the imperfections of a crystalline material are a major factor which influences the properties of materials significantly. These occurring defects can either enhance or degrade properties like hardness, toughness, electrical conductivity, and many more. The different bonding types and defects as well as the respective arising properties will be described in the subsequent paragraphs.

### 2.2.1 Chemical Bonding

Each material class exhibits a characteristic bonding type, which is significantly responsible for the respective properties of each material class. Therefore, the classification of materials according to their chemical bonding is a convenient and common way. Nevertheless, most of the materials used in industry exhibit mixed bonds and therefore also their properties can be modified by modifying the bonding state of a specific material via alloying.

In solid materials there are three main bonding types *Covalent Bonding*, *Ionic Bonding*, and *Metallic Bonding*. According to these bonding types materials and their respective properties can be divided into three material classes, see Fig. 3.

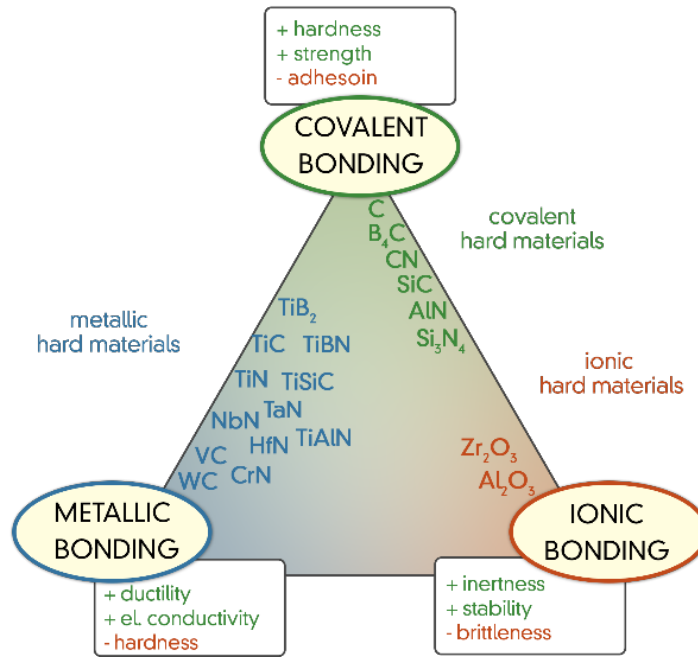


Fig. 3: Classification of hard ceramic materials according to their bonding character, taken with permission from [50].

**Covalent bonding:** These bonds are characterised by electron-pairs, see Fig. 4, shared by two atoms, in order to obtain a noble gas configuration. Materials with a high degree of covalent bonds have a high hardness, strength, and a high melting point. An example of a material exhibiting covalent bonds is diamond, the hardest (at least natural) material. In diamond each carbon atom is surrounded by 4 other carbon atoms forming a so-called  $sp^3$  hybrid orbital, leading to the highly directional covalent bonding and therefore the superior hardness.

**Ionic bonding:** In ionic materials, atoms with a small ionisation energy “donate” one or more electrons to atoms with a large electronegativity. Thereby, both ions—the positively charged cation and the negatively charged anion—obtain the noble gas configuration. The most prominent example of an ionic compound is rock salt, NaCl, in which each sodium atom donates one electron, to a chlorine atom. As a result,  $Na^+$  has a full shell (neon configuration) and also each  $Cl^-$  (argon configuration), see the corresponding illustration in Fig. 4. As the electrons are either fully removed or inserted, the bonding is completely non-directional. Due to the required charge-neutrality, ionic materials tend to form very regular crystal structures e.g. cubic structure, which lead to a very brittle behaviour, but due to the relatively large bonding energy also high melting points and a good hardness. Perfect ionic crystals are transparent and electrically insulating as they have no free electrons.



**Metallic bonding:** In metallic materials, the positively charged atomic cores (ions) are surrounded by delocalised electrons, also called electron gas or electron cloud, compare illustration in Fig. 4. As the electrons are freely mobile and not allocated to one specific core the bonding is non-directional. Due to these free electrons, metals are not transparent, because any photon can interact with many free electrons. A further consequence of the electron gas is that materials exhibiting metal bonds are also electrically conducting.

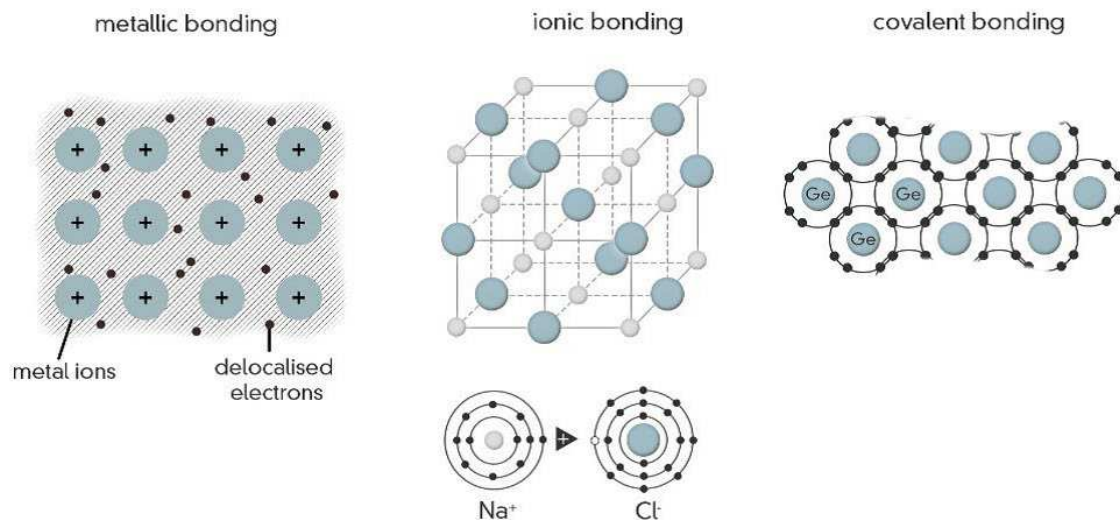


Fig. 4: Illustration of the three main bonding types: metallic bonding, ionic bonding, and covalent bonding, taken with permission from [50], originally from [51].

## 2.2.2 Defects

As already mentioned above, the imperfections or defects of materials are mainly responsible for their specific properties. There are several types of defects which all lead to an enhancement or degradation of the respective material property. The first class of defects are 0- dimensional defects or point defects. Another type of type of defects are 1- dimensional defects which are line defects. Area defects or 2-dimensional defects build the third class of material defects and 3-dimensional defects or volume defects are the last type. These defects and their influence on material properties will be described in the following paragraphs.

## Point Defects

Point defects or 0-dimensional defects are vacancies, interstitial, or substitutional atoms. **Vacancies** are simply lattice sites (usually occupied by atoms) where an atom is missing, see Fig. 5a. All solid materials consist vacancies as it is thermodynamically impossible to produce a material where every lattice site is occupied because vacancies increase the entropy of the material until a minimum energy level is reached. The number of equilibrium vacancies can be calculated by

$$N_V = N e^{-\left(\frac{Q_V}{kT}\right)} \quad \text{Eq. 10}$$

In Eq. 10,  $N_V$  is the number or equilibrium vacancies,  $N$  is the total number of atomic sites,  $Q_V$  is the activation energy needed to form a vacancy,  $k$  is the Boltzmann constant, and  $T$  the absolute temperature in K. As can be seen by Eq. 10, the number of vacancies increases exponentially with the temperature, leading to a vacancy concentration of about  $10^{-4}$  for metals for temperatures just below their melting point.

**Substitutional atoms** can either be smaller than the matrix atoms, see Fig. 5b, leading to tensile stresses in the vicinity of the foreign atom. Contrary, substitutional atoms which are larger than the matrix atoms, see Fig. 5c, cause compressive stresses around the foreign atom.

**Interstitial atoms** of course can also be smaller, Fig. 5d, or larger, Fig. 5e, than the matrix atoms. But in contrast to substitutional atoms, both of them lead to compressive stresses. As the name already suggests these atoms sit in the interstitial lattice sites, therefore the original lattice is strained causing the aforementioned compressive stresses in the region around the foreign atom.

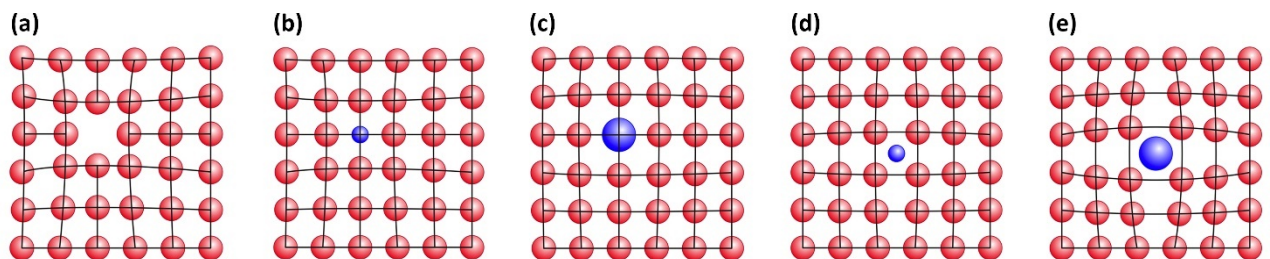


Fig. 5: Illustration of point defects (a) vacancy, (b) smaller substitutional atom, (c) larger substitutional atom, (d) smaller interstitial atom, and (e) larger interstitial atom, redrawn with permission from [52].

Pure metals consisting of only one element practically do not exist, as it is technically not possible to produce metals without any impurities. In the field of materials science such impurities are used on purpose to produce alloys. These can consist of an interstitial solid solution e.g.: steel (Fe-C) or a substitutional solid solution such as Fe-Cr. Additionally, an ordered solid solution can form if the foreign atom always sits on the same lattice site, an example for such an ordered phase is the  $\gamma'$ -phase in Ni-Al alloys ( $\text{Ni}_3\text{Al}$ ).

## Line Defects

Line defects or 1-dimensional defects are **dislocations**. There are basically two different types of dislocations, edge dislocations and screw dislocations, see Fig. 6.

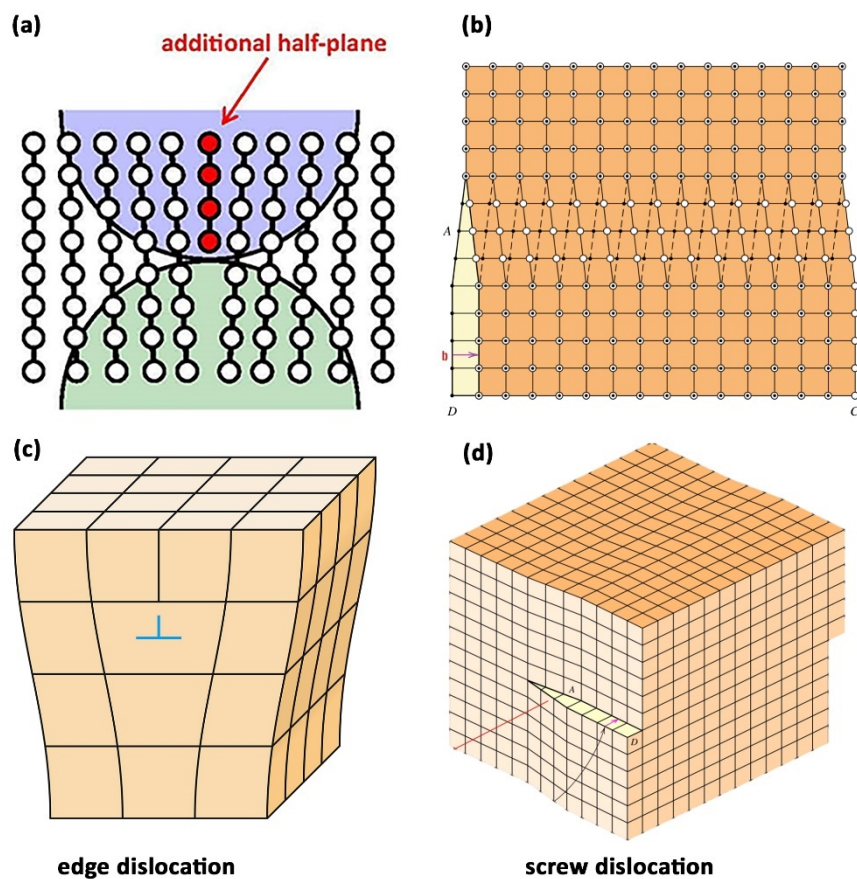


Fig. 6: Illustration of line defects: (a and c) edge dislocation and (b and d) screw dislocation, redrawn with permission from [52].

**Edge dislocations** are characterised by an additional half-plane introduced into the lattice, see Fig. 6a. This leads to either compressive stresses (blue area in Fig. 6a) or tensile stresses (green

area in Fig. 6a) in the vicinity of the dislocation. The line defined along the end of the extra half-plane is called dislocation line.

**Screw dislocations** have their name from the spiral path that is traced around the dislocation line (line A – B in Fig. 6b) by the atomic planes of atoms. They can be imagined as produced by a shear stress leading to a region of the crystal shifted by one atomic distance compared to the region below, see Fig. 6d.

The magnitude and direction of the lattice distortion associated with a dislocation is expressed by the so-called **Burgers vector**, marked as  $\vec{b}$  in Fig. 7. The nature of a dislocation (i.e. edge or screw) is also defined by the relative orientations of the dislocation line and the Burgers vector. For an edge dislocation, the Burgers vector is perpendicular to the dislocation line, see Fig. 7a, whereas for a screw dislocation they are parallel, see Fig. 7b. Dislocations observed in crystalline materials are generally are no pure edge or screw but mixed dislocations. Therefore, also the Burgers vector is usually neither perpendicular nor parallel.

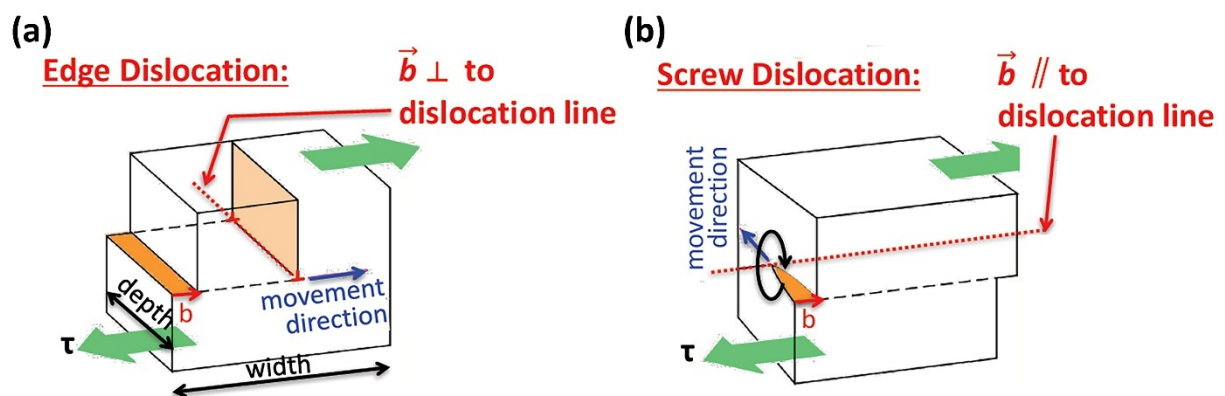


Fig. 7: Schematic illustration of (a) an edge dislocation and (b) a screw dislocation with relative orientations of dislocation line and Burgers vector, redrawn with permission from [52].

## Area Defects

Area defects or 2-dimensional defects are **boundaries or stacking faults**. These can be grain boundaries or phase boundaries, see Fig. 8.

**Grain boundaries** occur in polycrystalline materials and separate small grains or crystals having the same chemistry but different crystallographic orientation. These boundaries can be, depending on the lattice mismatch, low-angle grain boundaries or high-angle grain boundaries. Additional area defects are **stacking faults**, which occur if the stacking sequence of a certain crystal

structure is interrupted. For example, a face-centred cubic (fcc) structure has the stacking sequence A-B-C-A-B-C and so on if this sequence is changed to e.g. A-B-C-A-C-B a stacking fault is produced. Such stacking faults can lead to a special form of grain boundaries, so-called twin boundaries. Twin boundaries occur if a stacking fault is introduced and the stacking sequence is mirrored.

In contrast to grain boundaries, **phase boundaries** are areas separating grains not only differing in orientation but also in crystal structure or even in chemistry. Such boundaries are observed in multi-phased materials or after the decomposition of a homogenous solid solution into two or more phases.

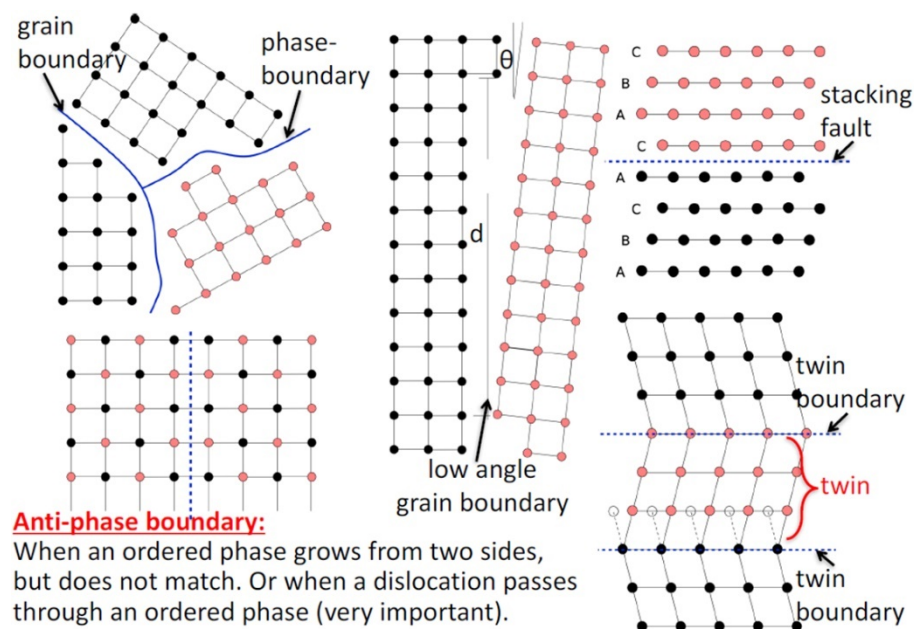


Fig. 8: Illustration of 2-dimensional lattice defects including: grain boundaries, phase boundaries, and stacking faults, taken with permission from [52].

## Volume Defects

In solid materials, there may be additional defects to those discussed above, which might have a huge influence on the material properties such as hardness and thermal stability. These 3-dimensional defects include pores, cracks, inclusions, and additional phases that may have been introduced into the material during the manufacturing process.

One example for volume defects in coatings or thin films are so-called droplets, which are macroparticles introduced during a deposition process (arc evaporation).



## 2.3 Strengthening Mechanisms

Materials which are subject to mechanical load, resulting in compressive, tensile, shear, or torsion stresses, can deform. The deformation can either be elastic (reversible), or plastic (permanent). Strength and hardness are the resistance against any form of deformation. The elastic deformation can be described by the Hooke's Law:

$$\sigma = E \cdot \varepsilon \quad \text{Eq. 11}$$

Hooke's Law (Eq. 11) describes the correlation between the elastic deformation  $\varepsilon$ , the occurring stress  $\sigma$  and the Young's modulus  $E$ . The Young's modulus is a material constant which equals the theoretical stress needed to elastically stretch a material to its doubled length. The higher the Young's modulus is the lower is the ability of a material to deform elastically. Therefore, materials considered as brittle such as ceramics, have a high Young's modulus, whereas materials considered as ductile, e.g. metals, exhibit a rather low Young's modulus.

In contrast to elastic deformation, plastic deformation either occurs by the mechanical twinning or by the movement of dislocations. Mechanical twinning usually occurs at low temperatures and at high deformation rates and only allows for small deformation. Additionally, mechanical twinning occurs less frequent, therefore, dislocation movement is the most important mechanism which leads to plastic deformation. To move dislocations a certain stress has to be applied. The stress needed to move a dislocation within a plane of atoms in the unit cell is called "Peierls stress". If the Peierls barrier is reached dislocations can move and the material can be plastically deformed.

To enhance the hardness and strength of materials, the dislocation movement has to be slowed down. There are several mechanisms which lead to a reduction in dislocation movement and therefore enhancing the hardness and strength of materials. These strengthening mechanisms and their underlying physical principles will be described in the following subchapters.

### 2.3.1 Strain Hardening

The strain hardening effect is based on the generation of dislocations. As dislocations are moving through the material under the influence of a driving shear stress, they are crossing each

other at some point. Due to local stress fields around the dislocations the force needed to further move the dislocation is increasing. As the dislocation density with increased plastic deformation is increasing, the number of collisions of dislocations also increases. Therefore, the higher the number of dislocations in a material, the harder it is to plastically deform it since the dislocation movement is hindered by the local stress fields of neighbouring dislocations. This hardening effect is also known as cold working as the plastic deformation, which increases the dislocation density, happens way below the melting point.

The increase of strength by the increase of the dislocation density can be described by the Taylor relation [53]:

$$\tau = \tau_0 + \text{const.} \cdot G \cdot b \cdot \sqrt{\rho} \quad \text{Eq. 12}$$

Within this relation,  $\tau$  is the stress needed to move dislocations,  $\tau_0$  is the Peierls stress,  $G$  the shear modulus,  $b$  the Burgers vector, and  $\rho$  the dislocation density. The Taylor relation makes clear that with increasing dislocation density the required stress to move dislocations is increasing.

### 2.3.2 Solid Solution Strengthening

Solid solution strengthening occurs due to the solution of atoms in a certain element matrix. The incorporation of such atoms can either lead to a substitutional solid solution by exchanging a matrix atom by a foreign atom or an interstitial solid solution by incorporation of an atom between the crystal lattice sites, see Fig. 9. Furthermore, a substitutional solid solution can either be randomly distributed, Fig. 9

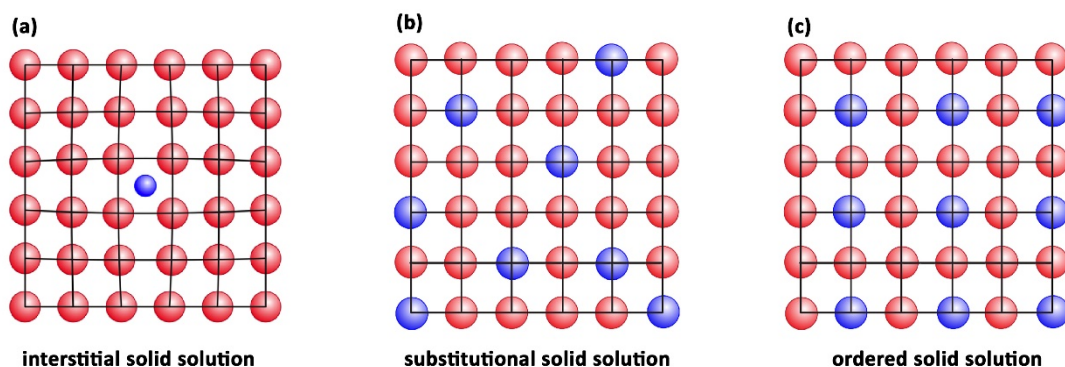


Fig. 9: Illustration of solid solutions (a) interstitial solid solution, (b) substitutional solid solution, and (c) ordered solid solution, reproduced with permission from [52].

The dissolved atoms lead to local stress fields in their vicinity which interact with the stress fields of dislocations and therefore the dislocation movement is hindered. The degree of strengthening can thereby be described by the Fleischer relation [54]:

$$\tau = \tau_0 + \text{const.} \cdot G \cdot \sqrt{c} \quad \text{Eq. 13}$$

In Eq. 13,  $\tau$  again is the required stress to move dislocations,  $G$  is the shear modulus, and  $c$  is the concentration of the alloying element. As the shear modulus is also depending on the amount of the alloying element, Eq. 13 is just a simplified version of the Fleischer relation. Additionally, to  $G$ , also the distance between alloying elements changes which further hinders the dislocation movement.

### 2.3.3 Precipitation Hardening

A supersaturated solid solution can form fine, homogeneously distributed particles (precipitates) of a second phase within the matrix which leads to a certain strength and hardness increase in alloys. This is achieved by suitable heat treatment causing the formation of these precipitates. This mechanism is referred to as precipitation hardening or age hardening.

Alloys can be strengthened by precipitation hardening if they consist of elements which can form intermetallic phases. Therefore, not every alloy exhibits the possibility of precipitation hardening. The mechanism of age hardening requires three steps. Step one is the formation of a supersaturated solid solution, meaning an alloying element is dissolved at high temperatures in the matrix element in an amount which would not be possible at low temperatures. The second step is subsequent quenching which forces the solute atom to stay within the alloy, leading to a supersaturated solid solution. Upon a following heat treatment, precipitations of an intermetallic phase form by decomposition. This heat treatment takes place at temperatures where diffusion is possible but below the temperature where the solubility limit of the dissolved element is reached. The amount and size of precipitations are strongly depending on the temperature and the annealing time. As the hardening effect is based on the hindering of dislocation movement by the



precipitations, the size and amount of them are major factors for the effectiveness of this strengthening mechanisms.

In precipitation hardened alloys two phenomena are observable depending on size and amount of precipitations. The first is that dislocations can “by-pass” the precipitations and the second one would be “cutting” of the particles. By-passing takes place if the particles are rather large and partly coherent or incoherent. If the particles are small and show coherent domains they will be cut. According to these two phenomena, fine and evenly dispersed particles lead to maximum strength.

### 2.3.4 Grain Refinement Strengthening

Grain refinement strengthening is based on the increase of the amount of grain boundaries which hinder the dislocation movement. The smaller the grains are, the more grain boundaries are within a material and therefore the dislocation movement is slowed down. This can be described by the Hall-Petch relation which is illustrated in Fig. 10.

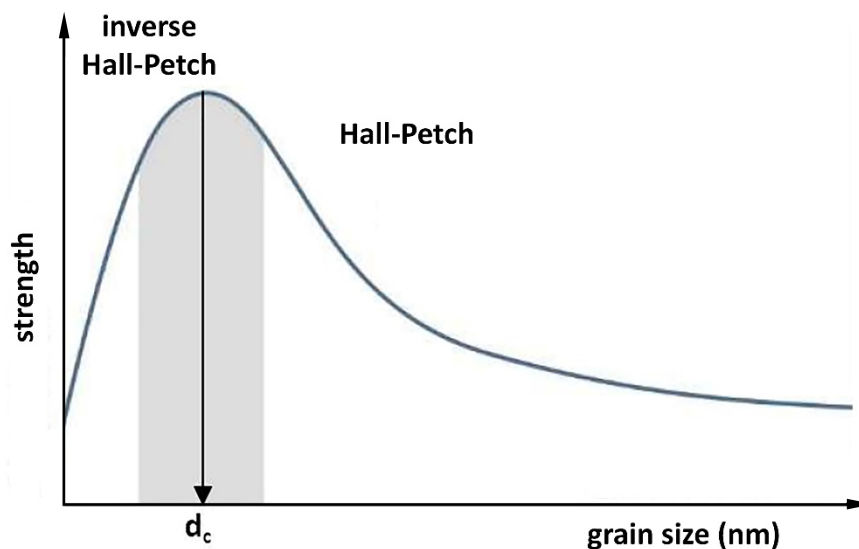


Fig. 10: Schematic illustration of grain refinement hardening by the Hall-Petch effect, redrawn after [55].

The increase in shear stress needed to move dislocations depending on the grain size is described by the Hall-Petch relation [55,56]:

$$\tau = \tau_0 + \text{const.} \cdot \frac{1}{\sqrt{d}} \quad \text{Eq. 14}$$

In Eq. 14,  $\tau$  is the shear stress required for dislocation movement,  $\tau_0$  again the Peierls stress, and  $d$  the grain size. With decreasing grain size, the volume fraction of the grain boundaries increases. This enables grains to glide on each other more easily which can also lead to an increase in ductility and not just hardness. If this mechanism becomes the dominating one the hardness again decreases, which is also known as inverse Hall-Petch effect. Therefore, there is a certain grain size  $d_c$  (compare Fig. 10) for which the strengthening mechanism has as maximum.

## 2.4 Diffusion

Diffusion can be described as the movement of atoms within a crystal lattice. There are several different mechanisms how diffusion can occur, see Fig. 11. Substitutional mechanism describes the movement from one lattice site to a neighbouring unoccupied site (vacancy), see Fig. 11a.

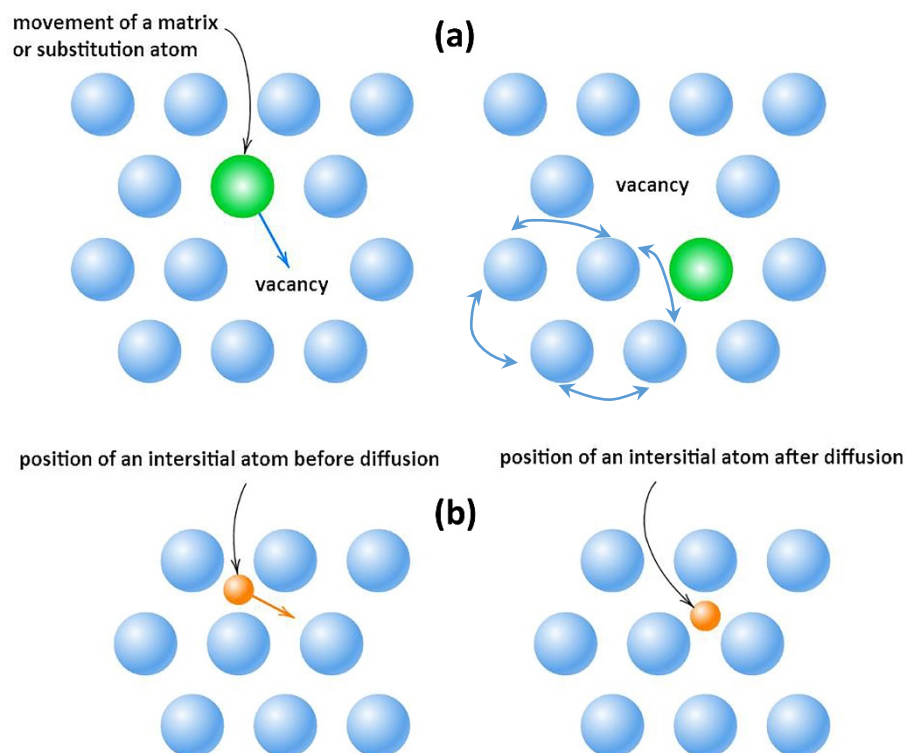


Fig. 11: Illustration of different diffusion mechanisms (a) substitutional mechanism and ring mechanism and (b) interstitial mechanism, reconstructed with permission from [52].

Direct exchange of atoms and ring mechanisms require an extremely high activation energy as several atoms have to move collectively and therefore heavily distort the lattice. Furthermore, interstitial mechanisms can take place, which means that an interstitial atom moves to a neighbouring unoccupied interstitial lattice site, see Fig. 11b.

Diffusion can occur through a crystal lattice but also on surfaces. Thereby the diffusion rate is much higher than the diffusion rate within the bulk material (1 – 2 orders of magnitude). Additionally, the diffusion over defects, such as grain boundaries and phase boundaries, is also increased compared to the diffusion rate across the bulk. Basically, the diffusion rate on the surface, over boundaries, and in the bulk is ranked by the respective diffusion coefficient:

$$D_{\text{surface}} > D_{\text{phase boundary}} > D_{\text{grain boundary}} > D_{\text{bulk}} \quad \text{Eq. 15}$$

The diffusion coefficient  $D$  for specific diffusion conditions can be calculated by:

$$D = D_0 \cdot e^{-\frac{Q_D}{RT}} \quad \text{Eq. 16}$$

In Eq. 16,  $D_0$  is the diffusion constant, which is frequency factor describing the total number of atom jumping attempts. Furthermore,  $Q_D$  is the diffusion activation energy, which is depending on the diffusion mechanism and several other factors,  $R$  is the universal gas constant, and  $T$  the absolute temperature. This equation shows that the diffusion coefficient and therefore the diffusion rate is strongly depending on the prevailing temperature. For example, at 0K the diffusion coefficient would also be zero and therefore no atom movement takes place, whereas with increasing temperature the mobility and therefore the diffusion coefficient and of course the diffusion rate increases.

Basically, the driving force for diffusion is the difference of the chemical potential, for stationary diffusion (steady state), the driving force can be described more precisely as the concentration gradient leading to Fick's first law of diffusion:

$$J = -D \cdot \frac{dc}{dx} \quad \text{Eq. 17}$$

Eq. 17 describes the diffusion flux  $J$  depending on the diffusion coefficient and the concentration gradient. Fick's first law shows that diffusion will always occur from regions of high concentration of one species to regions of low concentration.

Most of the practical diffusion processes are non-steady state, meaning the diffusion flux and the concentration gradient are time-dependent. This time dependence stems from the change of the concentration gradient—enrichment or depletion of diffusing species—with ongoing diffusion and therefore a change in the diffusion flux. The change of the concentration gradient depending on the diffusion time is described by Fick's second law:

$$\frac{\partial c}{\partial t} = D \cdot \frac{\partial^2 c}{\partial x^2} \quad \text{Eq. 18}$$

## 2.5 Softening Mechanisms

In contrast to strengthening mechanisms there are also mechanisms which decrease the hardness and strength of materials. There are two main mechanisms known as recovery and recrystallisation which are diffusion driven processes and therefore active at elevated temperatures. These two mechanisms as the name softening mechanisms already indicates act the exact opposite way as strengthening mechanisms by decreasing the dislocation density, decreasing defect density and/or increasing the grain size of precipitations or the material itself. Strain hardening as well as grain refinement strengthening are strongly affected by the softening mechanisms and high temperatures, respectively, whereas solid solution strengthening and precipitation hardening are still at least partly active also at higher temperatures. The ongoing processes and temperature regimes where softening takes place will be described in the following subchapters.

## 2.5.1 Recovery

Recovery is a softening mechanism occurring in any crystal which contains a non-equilibrium, high concentration of defects. By recovery a part of the stored internal deformation energy is relieved by rearranging of forming-induced defects (e.g., vacancies and dislocations). This occurs upon a heat treatment due to the increased mobility of atoms and the thereby higher diffusion rate. The result of the recovery process is a reduced vacancy concentration and a decrease of the dislocation density, leading to a significant decrease of internal stresses. Due to these processes the hardness and strength of a material partly decreases as the beneficial increase of dislocation density by strain hardening is inverted.

## 2.5.2 Recrystallisation

The recovered lattice still contains relatively high amount of grain boundaries and small grains keeping part of the strengthening mechanisms still active. In contrast to recovery—which has no incubation time, meaning as soon as the activation energy is reached recovery occurs—recrystallization takes place at a certain temperature ( $T_R \sim 0.4-0.5 T_m$ ) and after its incubation time. This incubation time is necessary because nucleation of recrystallization has to take place. This happens by coalescence of preferred sub-grains, leading to a reduction of the misorientation of neighbouring sub-grains by climbing of dislocations. The driving force for recrystallisation is the energy stored in dislocations. Minimizing this energy forces high-angle grain boundaries to move and form the recrystallised (stress- and strain-reduced) microstructure. This mechanism is known as primary recrystallisation which is often followed by grain growth. The driving force for grain growth is much lower than for recrystallisation. Therefore, grain growth and secondary recrystallisation (abnormal grain growth) take place at much higher temperatures. To reach secondary recrystallisation large grains—in the range of 2 – 3 times the size of the surrounding ones—are necessary. These grains can then grow abnormal fast at the expense of smaller grains, causing secondary recrystallisation. There is also a third form of recrystallisation taking place, for

example, in thin sheets where beneficially oriented crystals grow because a certain crystallographic plane is preferred due to its surface energy.

## 2.6 Thermal Stability

When materials are subject to high temperatures their structure or phase can change. If materials, consisting of a solid solution, are heated in an inert atmosphere it is likely that, if they are in a metastable state, decompose into their thermodynamically more stable constituents. If a reactive elements or compounds such as oxygen or acids are present metals or even ceramics as well as thin films tend to oxidation and corrosion [57–63]. The ongoing processes during decomposition and oxidation will be discussed in the following subchapters.

### 2.6.1 Decomposition

As described in 2.1 a system consisting of multiple elements can either be stable, metastable, or unstable. For the latter ones, decomposition can occur if the energy barrier, which has to be overcome to get to the stable state, is reached. There are two different decomposition mechanisms which can occur in materials depending on their initial state. This can either happen by nucleation and growth or by spinodal decomposition. The primary condition to observe decomposition is the existence of a miscibility gap and an initial composition either within the spinodal (spinodal decomposition) or the binodal (nucleation and growth).

A schematic illustration of a phase diagram exhibiting a miscibility gap of element A and B and the corresponding  $G - x$  curve with the local minima (stable concentrations) at a certain temperature is shown in Fig. 12.

The miscibility gap in the phase diagram is on the one hand defined by the spinodal (grey area in the phase diagram in Fig. 12) which is the sum of all inflexion points of the  $G - x$  curve. Within the spinodal a system is unstable, therefore already small fluctuations in the chemical composition are causing a decomposition. On the other hand, the miscibility gap is defined by the binodal. Between

the spinodal and the binodal a system is metastable and thus, has to overcome a certain energy barrier—formation of nuclei with the final chemical composition—to decompose into stable phases.

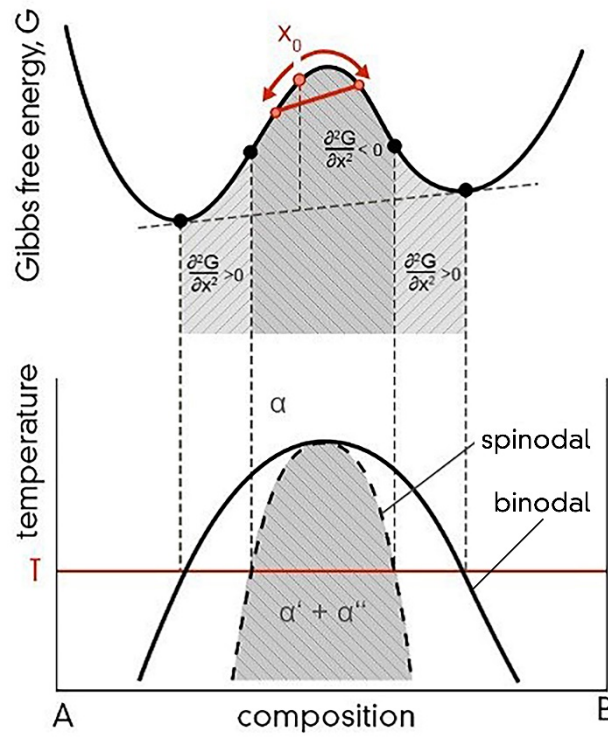


Fig. 12: Schematic binary phase diagram A–B with a distinct miscibility gap and the corresponding trend of the Gibbs free energy at a certain temperature  $T$ , adapted from [50], originally from [64,65].

The initial chemical distribution for both decomposition mechanisms is shown as a horizontal line in the top images in Fig. 13, indicated as  $x_0'$  and  $x_0$  for nucleation and growth, and spinodal decomposition, respectively. During the decomposition process both mechanisms show a completely different behaviour. Nucleation leads, as mentioned before, to nuclei already exhibiting their final chemical composition  $x_2$ —which is significantly differing from  $x_0'$ —these nuclei then grow until an equilibrium (stable) state of the chemical composition is reached. In contrast, spinodal decomposition shows a sinusoidal chemical distribution around the initial composition  $x_0$ . Thereby, the chemical composition of the precipitations changes until an equilibrium state with the surrounding matrix phase is reached. This form of decomposition is associated with diffusion against the concentration gradient also called “uphill diffusion”. This leads to an enrichment of the decomposing element in the precipitations whereas the matrix phase gets depleted. The driving force for spinodal decomposition is therefore not the concentration gradient, but the difference of the chemical potentials.

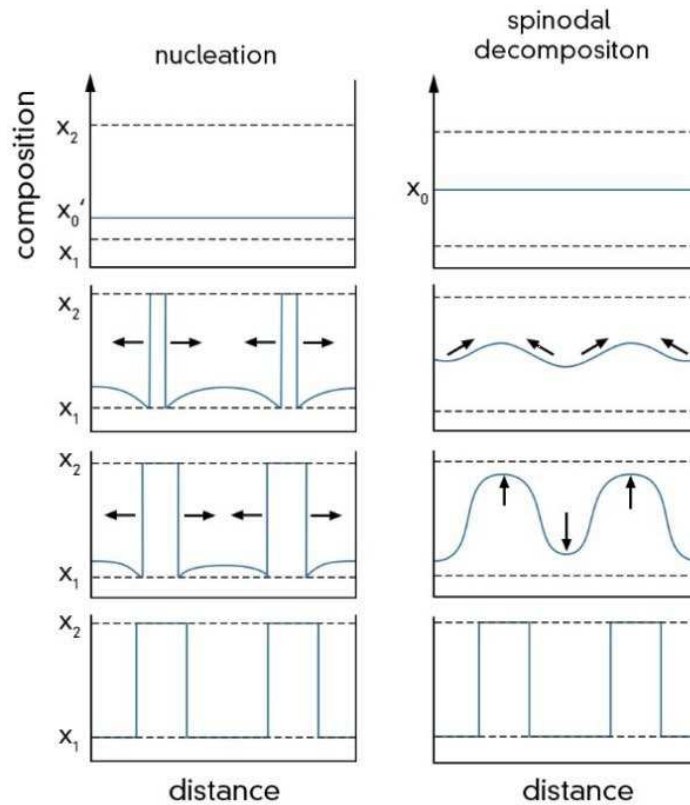


Fig. 13: Evolution of chemical composition during decomposition by nucleation and growth (left) and spinodal decomposition (right) taken with permission from [50].

## 2.6.2 Oxidation

If materials are exposure to oxygen containing atmosphere they will inevitably be oxidising. Generally, oxidation is chemical reaction, where metals (oxidising species) donate electrons and oxygen (oxidising agent) accepts them. The oxidation usually starts with the formation of an oxide layer on the outermost metal surface. As soon as an oxide layer is formed on the surface which is, in many cases, amorphous, the further scale growth is controlled by diffusion. Therefore, the process of oxidation is strongly depending on the prevailing temperature. The diffusion process of metals and oxygen ions is also depending on the material and scale morphology, leading to either outward diffusion of cations or inward diffusion of anions, see Fig. 14. As it is impossible to completely prevent materials from oxidation it is at least the aim to keep the oxidation process as slow as possible. The best oxidation resistance for materials is a fast and dense growing protective oxide scale. As the formation of such an oxide scale is accompanied with the generation of stresses,



the oxide scale eventually can get cracks. In this regard cation outward diffusion can help to heal the cracks of an oxide scale, whereas cation inward diffusion would lead to inner oxide growth and growth of cracks into the metal. To avoid this a dense oxide scale can lead to protection of the bulk material. One of the most prominent oxidation resistant layer is  $\alpha\text{-Al}_2\text{O}_3$  as the diffusion of oxygen is really slow and it is stable up to very high temperatures.

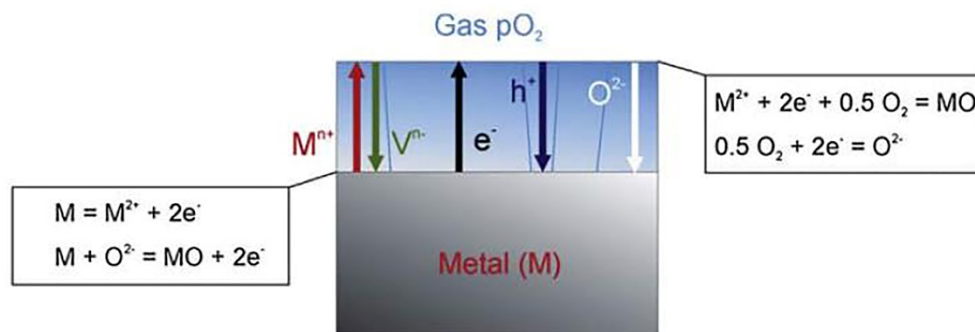


Fig. 14: Schematic illustration of diffusion-controlled oxide scale growth.  $\text{M}^{n+}$  indicating metal cations,  $\text{V}^{n-}$  cation vacancies,  $\text{e}^-$  electrons,  $\text{h}^+$  electron holes, and  $\text{O}^{2-}$  oxygen anions [66], originally from [67].

To classify the scale growth during oxidation, a convenient way is to measure the mass change. According to the, usually gain of mass, there are several different scale growth mechanisms and corresponding rate laws which are illustrated in Fig. 15.

**Linear growth** takes place whenever the oxide is not able to hinder the access of oxygen to the metal surface. Typically, linear growth occurs at high temperatures, e.g. iron at temperatures  $>1000\text{ }^\circ\text{C}$  shows this behaviour [68–71]. Metals which form volatile oxides in contrast, show a linear mass loss. This happens also at relatively high temperatures e.g. for W and Mo [72,73].

**Parabolic growth** occurs if the oxide layer covers the metal surface completely and acts as a diffusion barrier for metal and oxygen ions. The ion transport through the oxide scale becomes proportionally slower as the oxide layer gets thicker. The parabolic rate law is observed for most metals but strongly depends on the experimental conditions [69–71].

**Logarithmic growth** would be the slowest growth rate but only occurs at low temperatures and when a thin oxide layer covers the metal surface. After a rapid growth of the scale at the beginning of the oxidation process the rate becomes virtually zero as the temperature is usually low and therefore diffusion comparably slow.

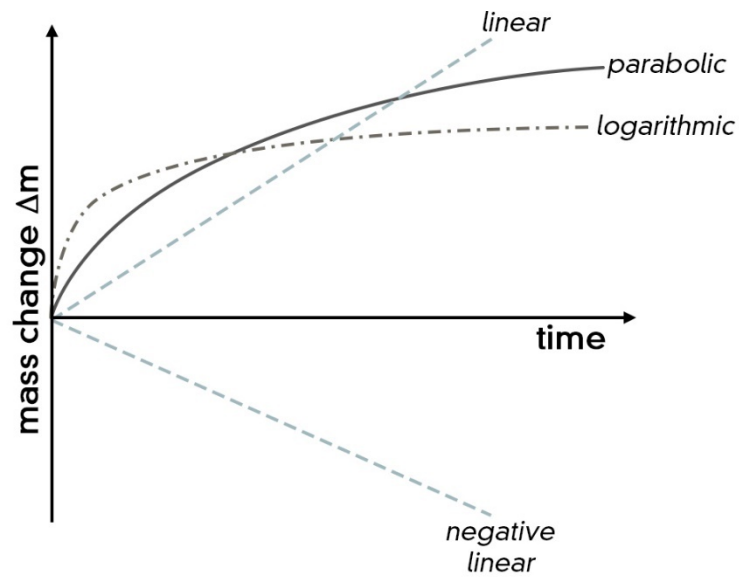


Fig. 15: Illustration of different rate laws relevant for oxidation of metals and films, taken with permission from [50], originally from [71].

## 3 Material Systems

The materials, investigated within this thesis, are mainly designed to act as protective coatings for tools and components which are subject to mechanical load, high temperatures, and hazardous environments. Different classes of materials such as nitrides, borides, and oxides are very often used for such applications. Within this thesis the concept of so-called high-entropy alloys is applied to the well-known field of protective ceramic coatings. The definition and advantages of HEAs as well as their properties and basic properties of commonly used nitrides, borides, and oxides will be discussed in the following subchapters.

### 3.1 High-Entropy Alloys

The improvement of materials by alloying is an omnipresent topic in the world of materials science. The latest invention regarding alloying are so-called high-entropy alloys which were first explored by Cantor et.al who named his first investigated alloys multicomponent equiatomic alloys [1]. Later Yeh, who connects the properties of such alloys to the high configurational entropy, introduced the term high-entropy alloys [2,74]. The two different names also lead to several definitions of these alloys. As the name multicomponent equiatomic alloys already suggests, the number of elements is undefined just the composition should be equiatomic [2]. In the case of alloys investigated by Cantor et.al the minimum number of constituent elements was five reaching to alloys consisting of 20 elements. High-entropy alloys in contrast are defined as alloys with a configurational entropy of at least  $\Delta S_{\text{config}} \geq 1.5R$  ( $R$  being the universal gas constant) [3]. To reach this limit five elements in a composition of 10 to 30 at.% are necessary (a five element equiatomic alloy would exhibit a  $\Delta S_{\text{config}}$  of  $1.61R$ ). Another definition, leading to an additional name for such alloys, is the definition by a compositional range. Such alloys should consist of at least five elements with a composition of 5 to 35 at.%, and are called compositionally complex or complex concentrated alloys (CCA) [75].

Nevertheless, such alloys, however they are called, can exhibit four core effects making them special and their properties significantly improve compared to conventional alloys. These effects,

namely the high-entropy effect, the severe lattice distortion, the sluggish diffusion, and the co-called cocktail effect can all be attributed to the unique chemical composition of such alloys.

The **high-entropy effect** as the name already suggests occurs due to the high configurational entropy present in the above-mentioned alloys. As previously discussed in chapter 2.1, the stability of a system increases with increasing entropy. The dominating part thereby is the configurational entropy which therefore is the only contribution used for the definition for HEAs. The entropy of a system increases with increasing number of elements and reaches a maximum for an equiatomic composition, compare *Eq. 8*. Furthermore, as can be seen by *Eq. 5* the stability of the system should increase even more with increasing temperature. Therefore, the high-entropy is considered to stabilise alloys at high temperatures making them applicable for high temperature applications. Furthermore, as a system has its maximum entropy when the elements are randomly distributed, the high-entropy effect should lead to the formation of solid solutions in simple structures like body-centred cubic (bcc) or face-centred cubic, instead of the formation of ordered structures or intermetallic compounds [2,76,77].

**Severe lattice distortion** occurs due to the mixture of several different elements which strongly differ in their atomic size. The degree of distortion of course corresponds to the respective elements. Nevertheless, the distortion is claimed to be more severe than in conventional alloys and therefore contributes to solid solution hardening leading to a higher hardness [76,78]. Furthermore, the lattice distortion leads to a decrease in electrical and thermal conductivity [76,78] as well as an increased activation energy for diffusion, which brings us to the third core effect.

High-entropy alloys exhibit **sluggish diffusion** due to the fact that for substitutional diffusion a significantly higher activation energy is required. This is on the one hand because several different elements are involved in this process meaning the chemical environment for every atom is different at every position. On the other hand, the lattice distortion and the therewith associated stresses make the diffusion even more difficult, as it would be in a stress-free lattice.

The last core effect is the **cocktail effect**, which was introduced by Prof. S. Ranganathan [79]. It simply describes a synergistic mixture in which the result is unpredictable and greater than the sum of parts [75].

Many different high-entropy alloys have been investigated in past 15 years. The most prominent HEA is of course the Cantor – alloy, CoCrMnFeNi, which forms a fcc solid solution [1]. Also HEAs based on refractory metals, exhibiting enhanced properties like hardness, toughness, and yield strength, are in the focus of bulk material research [15,16,80–86]. Furthermore, light-weight

HEAs or even so-called high-entropy steels are investigated within this wide range of possible compositions [87–91]. In summary the high-entropy concept gained a lot of attraction for researchers in the past years. Although, not every investigated composition exhibits enhanced properties just because of its entropy, the potential to produce materials with properties outperforming those of conventional alloys is definitely present. Nonetheless, as there are reams of possible compositions it is impossible to investigate every possible one and to find promising ones. Therefore, also computational high-throughput search is applied in the field of HEAs to preselect compositions and atomic ratios which might lead to an alloy with enhanced properties [92].

## 3.2 Transition Metal Nitrides

Among the reams of available and applied materials, transition metal nitrides (TMN) are the most important ones. Binary and ternary and TMNs such as Ti-N, Ti-Al-N are widely applied for cutting tools and inserts. Nowadays, additional alloying elements such as Ta, Zr, Mo or lanthanoids, further increase the performance of those coatings. Thin films alloyed with the aforementioned elements exhibit high hardness, high thermal stability and oxidation resistance, as well as an increased fracture toughness and are therefore they are highly suitable for high temperature applications [20,22,24,26–28,93–95]. Most TMNs crystallise in an face-centered cubic (fcc) crystal structure (B1, space group  $Fm\bar{3}m$  (225), NaCl-prototype) except TaN which has a hexagonal crystal structure in its stable form (space group  $P\bar{6}2m$  (189)). The most common structure for TMNs, the NaCl-prototype structure, is illustrated in Fig. 16.

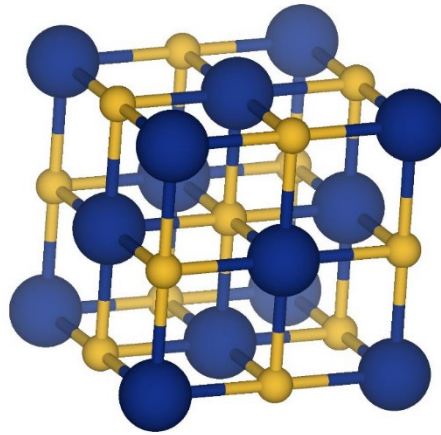


Fig. 16: Schematic illustration of NaCl-structured TMNs showing the fcc sublattice occupied by the transition metal (blue spheres) and the octahedral interstices occupied by nitrogen (yellow spheres), visualised with VESTA [96,97].

### 3.3 Transition Metal Borides

As transition metal borides (TMB), and here especially refractory borides such as  $\text{HfB}_2$ ,  $\text{TaB}_2$ , or  $\text{ZrB}_2$ , exhibit very high melting points, they count to the class of ultra-high temperature ceramics (UHTC). TMBs preferably crystallise in two different crystal structures the  $\alpha\text{-AlB}_2$ -structure (P6/mmm, space group no. 191) [98] or the  $\omega\text{-W}_2\text{B}_5$  structure (P6<sub>3</sub>/mmc, space group no. 194) [99], see Fig. 17. Borides are a rather unexplored class of materials. Especially in the field of thin films there is a vast number of binary borides which have not been investigated yet. Nevertheless, recent research has been done by computational high-throughput search to scan the properties of binary borides and combine them to ternaries to tune their properties [42–44,100]

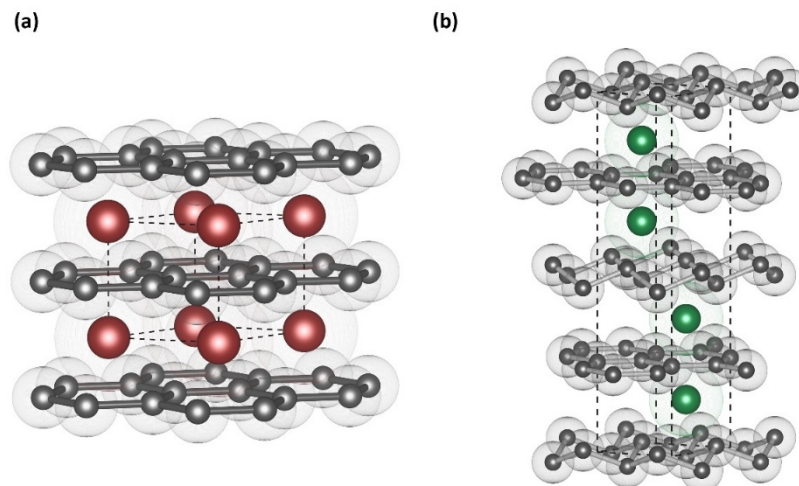


Fig. 17: Schematic illustration of a)  $\alpha$ - $AlB_2$ - structure (B, grey spheres and Al, red spheres) b)  $\omega$ - $W_2B_5$ - structure (B, grey spheres and W, green spheres) adapted from [43].

### 3.4 Transition Metal Oxides

In contrast to TMNs and TMBs, transition metal oxides (TMO) crystallise in many different crystal structures. Two prominent types of oxide structures are the corundum ( $\alpha$ - $Al_2O_3$ ) structure and the rutile ( $TiO_2$ ) structure, see Fig. 18. Alumina is very common used as protective coating but is mainly synthesised by chemical vapour deposition (CVD) as it requires high temperatures to grow. There are several other (cubic) modifications of  $Al_2O_3$  which are preferred at lower temperatures. Nevertheless, the corundum structure would be the desired one when aiming for  $Me_2O_3$  stoichiometry as it exhibits comparably high hardness and is the thermodynamically most stable configuration of  $Al_2O_3$ . The second oxide structure possible for many TMOs is the rutile structure [101]. Like  $\alpha$ - $Al_2O_3$ ,  $TiO_2$  also requires rather high synthesis temperatures to grow in the thermodynamically stable rutile structure. Synthesised at low temperatures  $TiO_2$  crystallises in the anatase structure which eventually transforms into rutile upon annealing. As anatase exhibits a significantly higher volume the transformation to rutile is accompanied with the generation of undesired stresses and ablation of coatings. Therefore, if aiming for  $Me_2O$  stoichiometry the desired crystal structure is the rutile-structure.



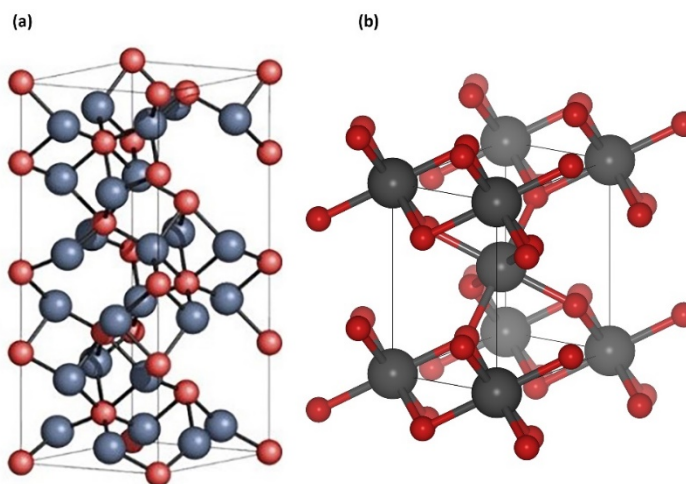


Fig. 18: Schematic illustration of (a)  $\alpha$ - $\text{Al}_2\text{O}_3$ -structure (Al, blue spheres and O, red spheres) and (b) rutile- $\text{TiO}_2$ -structure (Ti, grey spheres and O, red spheres).

### 3.5 High-Entropy Ceramics

The aforementioned high-entropy concept can also be applied for above described ceramics. This class of materials is defined as materials consisting of 5 binary ceramics e.g. nitrides, borides, oxides, or carbides [102]. Depending on the stoichiometry (metal to non-metal ratio) of the compound it can be assumed that for most of the relevant systems the non-metal part is at least 50 at.%. Based on this the configurational entropy of these compounds does not meet the required value of  $1.5R$  when calculated per atom, as the non-metal sublattice does not exhibit a configurational entropy. Nevertheless, these materials count to high-entropy materials as they have, within their material class, a high-entropy metal sublattice. Additionally, some researchers calculate the configurational entropy per formula unit, which then also leads to a value of  $1.61R$  when assuming an equimolar composition. In the field of high-entropy ceramics many different classes and compositions have been investigated as bulk materials and as thin films. For coatings, the most prominent material class investigated are high-entropy nitrides. These exhibit besides high hardness and oxidation resistance also promising properties for the use of diffusion barriers, which can be attributed to one of the four core effects, namely the sluggish diffusion [7,103–109]. In the field of borides, there is more research on the synthesis of bulk materials [110–113]. Although borides might also benefit from the high-entropy concept there is just one paper on HEB coatings,



however, showing promising results with a hardness in the as deposited state of  $47.2 \pm 1.8$  GPa [41]. Also even more investigated are HEOs where also a significant entropy stabilisation of the NaCl-structure is reported for a bulk material synthesised by mixing five oxide powders and then heating them up [114]. Further investigations on bulk HEOs also concentrate on electrical and thermal properties of spinel- fluorite, or perovskite-structured oxides also partly exhibiting entropy stabilisation [115–121]. In contrast, thin films based on the HEO concept are rarely investigated. Yeh et al. investigated (Al,Cr,Ta,Ti,Zr)-oxides which are amorphous in the as deposited state and crystallise in a multi-phased structure at 900 °C [122]. Additionally, Tsau et al. investigated the electrical resistivities of HEO thin films [123,124]. Consequently, the high-entropy concept for oxide thin films seems to be a possibility to significantly improve and tune the properties of oxide coatings for several applications.

## 4 Deposition of Thin Films

For the deposition of thin films and coatings several techniques were developed in the last decades. Basically, there are two different techniques, namely physical vapour deposition (PVD) and chemical vapour deposition (CVD). These two techniques differ in the way how the material which should be deposited is transferred to the vapour phase. Within these two categories of deposition methods, several different specified techniques are available. As the basic methods are the industrially most relevant they will be described in the subsequent chapters. Additionally, the magnetron sputtering and arc evaporation, the two most prominent PVD techniques will be described in detail.

### 4.1 Physical Vapour Deposition

In PVD processes the transfer from solid or liquid phases to the vapour phase in only happens by physical means. This can take place by a momentum transfer as it is the case for sputtering or by introducing thermal energy which transfers solids or liquids to vapour. Independent of the physical process which transforms the material to be deposited into the vapour phase, most PVD techniques are based on a plasma discharge, resulting in a characteristic voltage-current relationship, see Fig. 19.

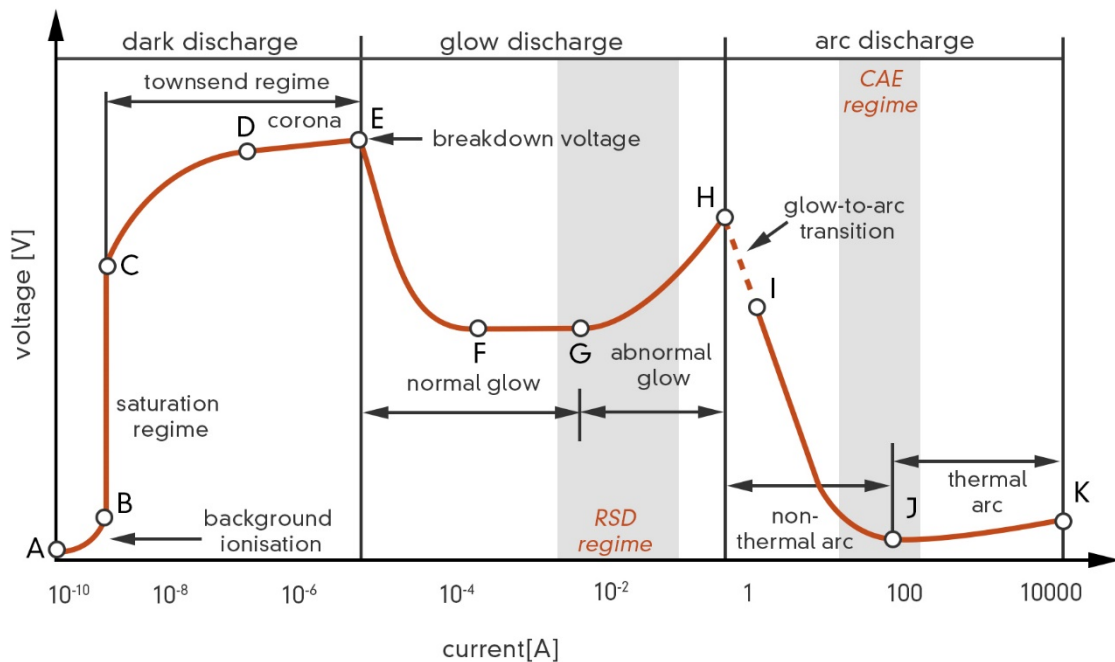


Fig. 19: Schematic voltage-current characteristics for plasma discharge PVD relevant regimes are marked with grey background, taken with permission from [50], originally from [125].

The initial condition of a PVD process is an evacuated vacuum chamber, in which subsequently a process gas (e.g., argon) is introduced, leading to a pressure of  $<10^{-1}$  mbar. The region between A – E in Fig. 19, is called dark discharge, since no visible light is emitted in this region, except for possible corona and breakdown discharges.

Although there is a really small number of particles present in the initial state, there is a low voltage observable which arises due to ubiquitous radiation, see point A in Fig. 19. When applying a voltage between an anode and a cathode, the current increases until all available charged species emerging by the background ionisation is attracted, point B. For a further increase of the current a significant higher voltage value (point C) is necessary. The region between point C and E is the so-called “Townsend regime” which is characterised by an exponential current increase. Within this regime the electric field strong enough to accelerate electrons, leading to ionisation of neutrals by collisions and hence the formation of ions and secondary electrons.

Point E represents the end of the dark discharge regime. There, the first technically important sector starts at the so-called “breakdown voltage”, characterised by a steep voltage decrease. From this point, the energy of particles and electromagnetic radiation is high enough to promote the emission of secondary electrons. The electrons required for the plasma are henceforth produced autonomously, leading to a stable plasma although, the voltage is decreasing (section E–F). As the

plasma present in the region starting at E is in the range of visible light this region is called “glow discharge”. The section between F and G, is characterised by an expansion of the plasma over the cathode, leading to an increase in ionised species at a constant voltage level. The so-called “abnormal glow” region, starting at G, defines the region in which (reactive) sputter deposition (RSD) typically takes place.

At point H the energy at the cathode surface is sufficiently high for thermally induced electron emission, so-called thermionic emission. This point is the origin of the arc discharge regime. Arc discharges are undesirable in sputter deposition but essential for cathodic arc evaporation. Therefore, this region, especially in the range of point J, represents the area in which arc evaporation takes place.

As can be observed from the voltage-current characteristic the process parameters for RSD and CAE are significantly differing. Whereas for RSD rather high voltages and a comparable low current is used, the CAE process requires just low voltages but a quite high current to strike an arc.

### 4.1.1 Magnetron Sputtering

Sputter deposition processes are based on a glow discharge which leads to the formation of an ionised inert gas. These gas ions, mainly  $\text{Ar}^+$ , are accelerated towards a negatively charged cathode equipped with the material which should be deposited. When Ar-ions hit the surface of the base material, also called target, atoms are ejected and therefore transformed to the vapour phase. These ejected atoms move through the plasma and adsorb on the substrate surface where the thin film is formed. A basic sputtering system consists of a pumping system, a gas inlet, a substrate holder with a heating element as well as the cathode where the target is mounted, see *Fig. 20*. The cathode can additionally be equipped with a magnetron. The magnetron enhances the effectivity of the sputter process as it helps to trap secondary electrons which leads to a higher amount of ionisation in the vicinity of the target and therefore to a higher sputtering rate.

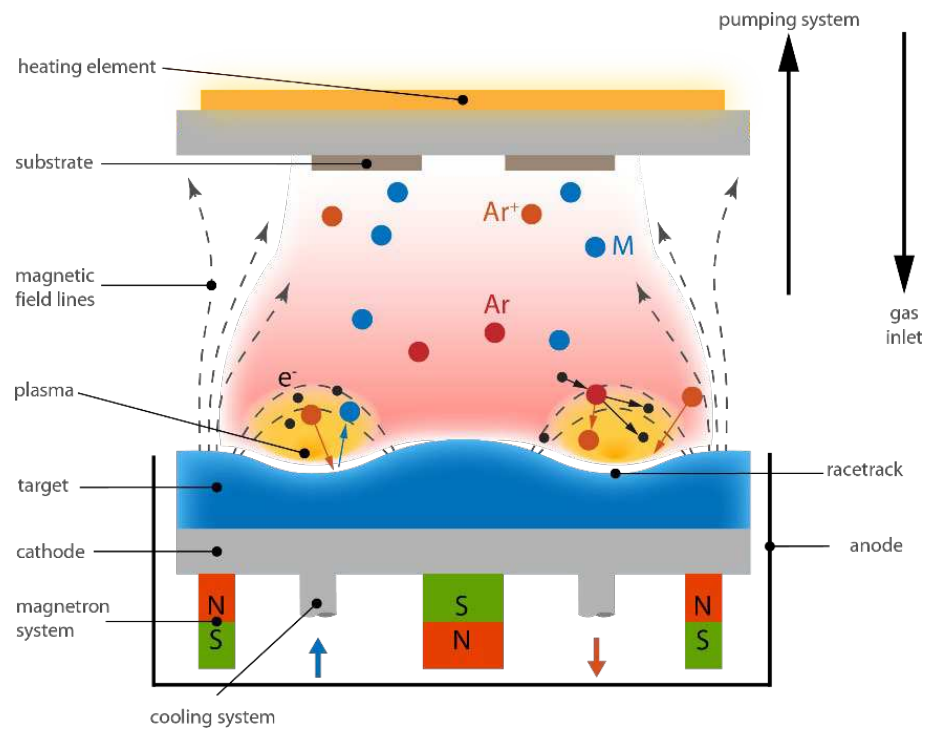


Fig. 20: Schematic illustration of a magnetron sputter process, taken with permission from [126].

As along the magnetic field of the magnetron the sputter rate is significantly increased, a preferred area of atom ejection evolves, the so-called racetrack. Nevertheless, the sputter rate is not just depending on the magnetic field or the degree of ionisation but especially on the sputter yield. The sputter yield is defined as ejected atoms per impinging ion and has a certain value for every single element and for a certain energy with which the ions arrive. As the sputter yield is strongly depending on element properties such as bonding strength and atomic weight, the sputter rate and therewith the deposition rate can vary in a wide range depending on the target material.

In addition to the working gas (Ar) a reactive gas can be introduced into the chamber to form ceramics e.g. nitrides, oxides, or carbides. In the case of nitrides, nitrogen ( $N_2$ ) is used as a reactive gas. As the reactive gas also reacts with the target surface, nitride layers are not only formed on the substrate but also on the target and within the whole deposition chamber. The formation of ceramic layers on the target surface is also known as poisoning. This poisoning effect leads to a significant reduction of the deposition rate as the sputter yield significantly decreases due to the formation of the strongly bonded ceramic layers [127].

## 4.1.2 Cathodic Arc Evaporation

The industrially most relevant PVD technique is cathodic arc evaporation (CAE). Compared to sputtering, CAE exhibits a much higher degree of ionisation of up to 99 %. This higher degree of ionisation results in a much higher deposition rate and leads to significantly improved coating properties as the ionised metal atoms help do densify the coating.

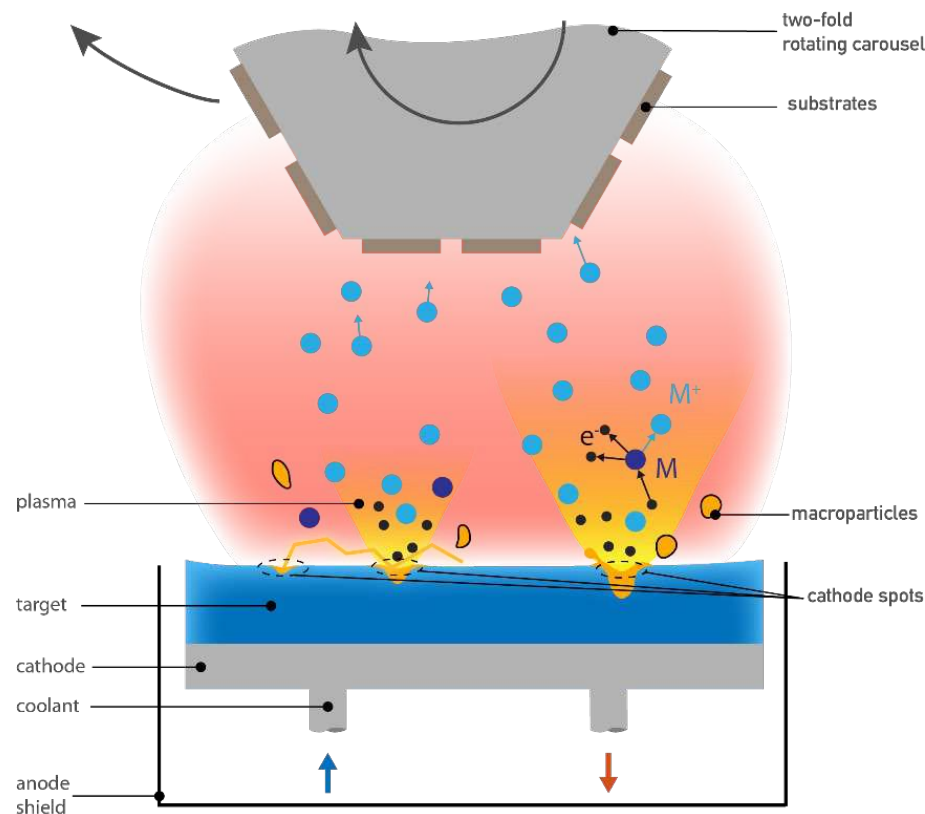


Fig. 21: Schematic illustration of an arc evaporation process including essential components, taken with permission from [50].

The arc evaporation process is characterised by a high current – low voltage discharge which leads to the striking of an arc on the target surface. The target material, acting as the cathode, is thereby evaporated. The active centres of the evaporation are called “cathode spots”, see Fig. 21. As these spots are limited to a few microns, the power input in these regions is very high causing the aforementioned high degree of ionised matter. Due to several phenomena, namely, thermionic emission, thermionic-field emission, field emission, and thermo-field emission, taking place in the vicinity of the active cathode spot, the conditions for a reignition of the arc are favoured. This continuous reignition together with the prevailing cathode surface leads to a “walk” of the arc over

the cathode surface. Usually the arc follows a “random walk” just depending on the cathode surface conditions. To control the arc’s motion, a magnetic field can be applied to the cathode leading to the so called “steered walk” of the arc.

The evaporation of the target material by the moving arc, not only leads to evaporated species but also causes the formation of macroparticles. These so-called “droplets” are generated due to a melting pool in the vicinity of the cathode spot. The liquid material in these melting pools is accelerated away from the target surface by a rapid compression induced by the plasma pressure. The size and number of droplets strongly depends on the target material and its microstructural composition. As these droplets are mainly metallic, also in reactive processes, and condense on the substrates and therefore affect the film growth, they are considered to be defects leading to reduced mechanical properties and adhesion of thin films.

## 4.2 Nucleation and Growth

Every film growth starts with the adsorption of atoms or ions (generated at the target) onto the substrate surface. Nucleation can be seen as a simultaneous process of adsorption, desorption, and adatom diffusion. If the atoms reach an energetically preferred site, they will accumulate and as soon as they overcome the nucleation barrier ( $r^*$ ), grain growth will take place. The energies responsible for the nucleation and growth mechanism are schematically illustrated in *Fig. 22*.

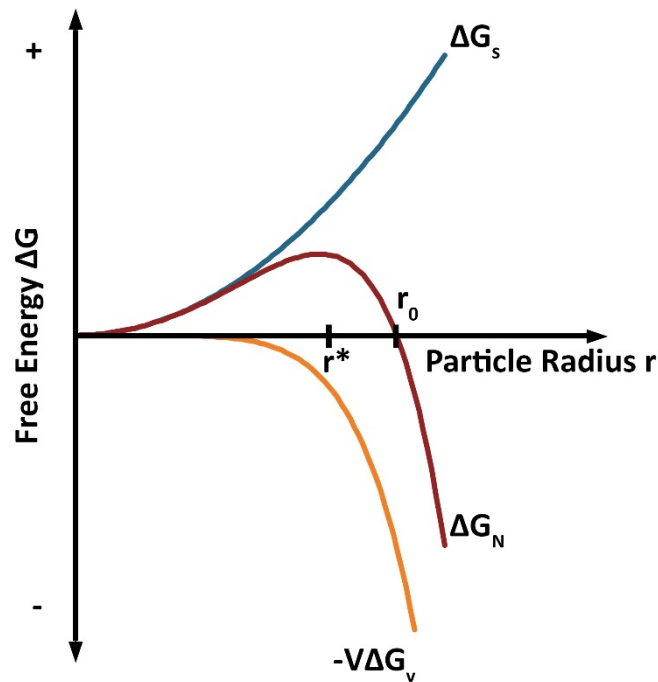


Fig. 22: Schematic diagram of the trends of the various contributors of the Gibbs free energy depending on the particle radius.

Particle growth takes place when the free energy  $\Delta G$  is a negative, meaning if the system gains energy by becoming larger. To reach this point the energy gained by the formation of chemical bonds and increasing the volume ( $\Delta G_V$ ) has to be larger than the energy which is required to form a new surface ( $\Delta G_S$ ). Assuming the formed nuclei to be spheres, this can be described as follows:

$$\Delta G_N = \Delta G_S - V \cdot \Delta G_V = 4r^2\pi \cdot \gamma - \frac{4r^3\pi}{3} \cdot \Delta G_V \quad \text{Eq. 19}$$

Within Eq. 19,  $r$  is the particle radius,  $\gamma$  the surface energy, and  $\Delta G_V$  the energy gain due to the formation of an energetically favoured phase. According to this equation it is obvious that at a certain size of the nucleus the formation of the new form is energetically preferred and therefore particle growth starts. The critical particle radius  $r^*$  is the point where the slope of  $\Delta G_N$  equals zero. Therefore, it can be obtained by the first derivation of  $\Delta G_N$ ,  $d\Delta G_N/dr = 0$ , which leads to:

$$r^* = \frac{2\gamma}{\Delta G_V} \quad \text{Eq. 20}$$



Particles smaller than  $r^*$  are unstable and will eventually dissolve under energy gain, whereas particles larger than  $r^*$  will grow. The formation of nuclei with a size larger than  $r_0$  is energetically always preferred.

Depending on the different surface energies, and deposition parameters, there are three different idealised growth modes which can occur:

- *layer-by-layer growth*
- *island growth*
- *mixed growth*

The *layer-by-layer growth* was first described by *Frank* and *van der Merwe*, see Fig. 23. This growth mode preferably occurs if the substrate surface energy is higher than the sum of the film-surface energy and the interface energy between substrate and film. Furthermore, the interface energy of substrate and film has to be higher than the interface energy of film and adatoms. Strictly speaking, the film atoms are more strongly bound to the substrate than to each other. Another parameter which promotes layer-by-layer growth is a high diffusion rate. Due to the high mobility of adatoms they rather migrate over the surface to form a thin layer, than accumulate to each other and form an island. The layer-by-layer growth is for many applications the preferred growth mode due to the high coverage of the substrate surface and thus the formation of dense films. But the fact that diffusion, if not promoted by a high substrate temperature or kinetic ion bombardment, is a rather slow process, the film growth rate for the ideal layer-by-layer growth is relatively low.

The second growth mode, namely *island growth*, was described by *Volmer* and *Weber*, see Fig. 23b. Island growth in contrast to layer-by-layer growth occurs preferably if the adatoms are more strongly bound to each other than to the substrate surface, and if the energy of the growth process is too low to activate fast diffusion.

The third growth mode is, a combination of the two previous modes and referred to as *Stranski-Krastanov* or *mixed growth mode*, see Fig. 23c. The mixed growth can be considered to be the most common growth mode, and present in many PVD processes. It is characterised by an initial layer-by-layer growth followed by the formation of three-dimensional islands. This again can be explained by the surface energy evolution.

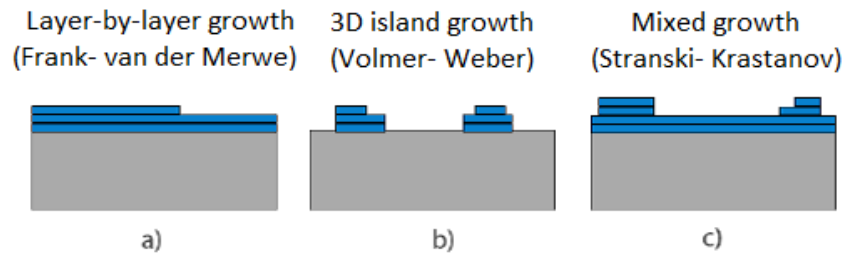


Fig. 23: Illustration of the three basic growth modes occurring in thin films: (a) Frank-van der Merwe, (b) Volmer-Weber, and (c) Stranski-Krastanov adapted from [125].

### 4.3 Structure Zone Diagram

To correlate the growth morphology of thin films with basic deposition parameters, so-called structure zone diagrams (SZD) have been developed. Thin films, even if they exhibit a similar chemical composition, can have entirely different properties, depending on their growth morphology. Deposition parameters such as substrate temperature, deposition pressure, and bias voltage can have a crucial impact on the growth behaviour of coatings. The first so-called structure zone model (SZM)—also referred to as structure zone diagram—was already established in 1969 by Movchan and Demchishin [128]. This SZD describes the influence of the substrate temperature (homologous temperature  $T_h$ ) on the morphology of “thick” (>100 nm) films synthesised by evaporation. The substrate temperature is thereby represented by the term  $T/T_m$  with  $T$  being the actual temperature and  $T_m$  the melting point of the respective material—both in Kelvin. Messier et al. [129] and Thornton [130] extended this model by introducing the substrate bias voltage, see Fig. 24a, respectively the argon pressure, see Fig. 24b.

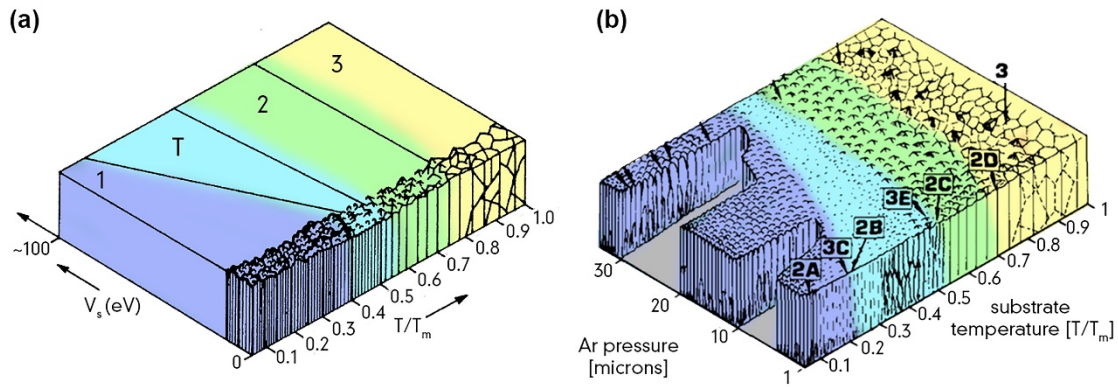


Fig. 24: Structure zone diagrams after a) Messier[129] and b) Thornton [130], adapted from [50].

Whereas in the SZD of Movchan and Demchishin are only three different zones and corresponding growth morphologies, in the SZDs of Messier and Thornton an additional zone, the transition zone (T). In zone 1 the microstructure is porous and/or amorphous due to poor surface mobility caused by the low temperature and low ion energy. With increasing temperature, the mobility of the atoms increases and leads to a denser microstructure. In zone 2 atoms are able to fill voids and overcome shadowing effects due their higher energy. Therefore, the morphology in zone 2 exhibits columnar grains and smooth surfaces. Between zone 1 and 2, the transition zone T is located. The particle energy in zone T is high enough to promote the surface diffusion, but insufficient for grain boundary diffusion, leading to V-shaped grains. However, because of competitive growth of different grains, they are subdivided and do not extend over the entire film thickness. The morphology in zone 3 can already be attributed to recrystallisation as the temperature is high enough for volume diffusion, leading to comparably big grains with random orientation.

The bias voltage as well as the Ar pressure have a strong influence on to the energy of the incoming particles. An increase of the bias voltage results in higher velocities for the impinging particles, hence the transition from zone 1 to T shifts to lower temperatures at the expense of zone 1. The effect of the Ar pressure can be described the kinetics of particles [131]. A low pressure is associated with a comparably long free mean path, leading to only few collisions on the way to the substrate, hence their energy is higher when arriving at the substrate surface. In contrast if the pressure, and therefore the number of particles, increases the corresponding energy distribution decreases [132]. In further consequence, the transition from zone 1 to zone 1 shifts to a higher temperature with increasing pressure.

More than 25 years later, Anders established a more advanced model by including plasma-based deposition and ion-etching processes [133], see Fig. 25. This model was developed due the rising usage of highly ionising and more energetic processes such as cathodic arc evaporation and high-power impulse magnetron sputtering (HiPIMS). The morphology of coatings deposited with aforementioned methods can thereby be more properly described than with other SZDs. The basic layout of the SZD developed by Anders contains the following parameters:

- The generalised temperature,  $T^*$ , which includes the homologous temperature (quotient of deposition temperature and melting temperature) plus a temperature shift caused by the potential energy of particles arriving on the surface.
- The normalised energy,  $E^*$ , describing displacement and heating effects by the kinetic energy of bombarding particles.
- The film thickness,  $t^*$ , which is shown on the z-axis, which allows to include "negative thickness" caused by ion etching processes.

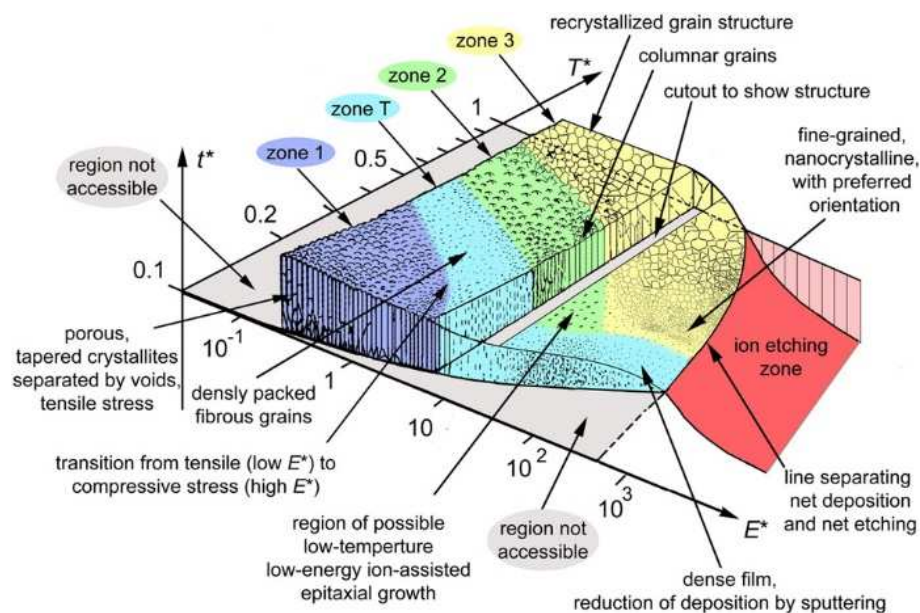


Fig. 25: Advanced structure zone diagram according to Anders [133].

## 5 Investigative Methods

Fundamental knowledge of properties of thin films such as morphology, crystal structure, chemical composition, and mechanical properties is of utmost importance to specifically tune the performance of coatings for individual applications. To gain this information many different methods are available. The methods used to investigate the properties presented in this thesis, their functionality as well as their limits will be described in the following subchapters.

### 5.1 Structural Analyses

Many properties of coatings are strongly related to their crystal structure as well as their growth morphology. Therefore, X-ray diffraction and electron microscopy were used to determine the crystal structure, grain size, coating thickness as well as the morphology of the synthesised thin films.

#### 5.1.1 X-Ray Diffraction

To determine the crystal structure and grain size of the coatings X-ray diffraction (XRD) is a powerful tool. XRD is based on the diffraction of X-rays by lattice planes of a crystalline material. As the diffraction of the beam occurs in distinct angles the lattice plane distance can according to Bragg be determined by:

$$n\lambda = 2d \sin\theta \quad \text{Eq. 21}$$

The Bragg-equation (Eq. 21) describes the correlation between the wavelength  $\lambda$  the lattice plane distance  $d$ , and the diffraction angle  $\theta$  [134]. By solving Eq. 21, it is possible to determine

lattice plane distances for a certain diffracting lattice plane ( $hkl$ ), using the wavelength of the incident X-ray beam and the diffraction angle. Within the Bragg-equation the integer  $n$  describes the order of diffraction.

In this thesis two different diffraction geometries were used to determine crystal structure and lattice parameters, see Fig. 26. The Bragg-Brentano (BB) configuration is usually used to investigate powdered samples or bulk materials. In this arrangement the X-ray source and the detector are placed symmetrically to the sample-surface normal. Due to the relatively high angle of incidence, the X-ray beam is penetrating the sample quite deep, leading to a significant contribution of the substrate to the XRD pattern. If sample peaks and substrate peaks are overlapping it is difficult to evaluate the crystal structure and lattice parameters of the sample. Therefore, it is reasonable to reduce the angle of incidence which leads to a lower penetration depth and therefore no undesirable substrate peaks occur. The arrangement where a small angle of incidence of  $\sim 2^\circ$  is used is called grazing incidence and is illustrated in Fig. 26 on the right.

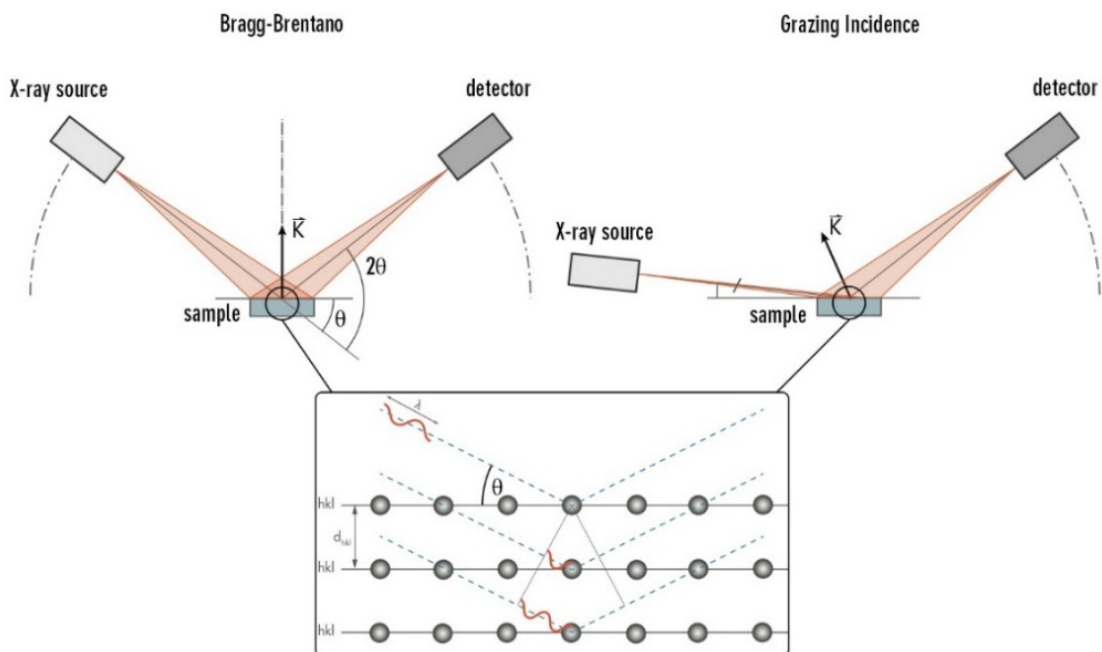
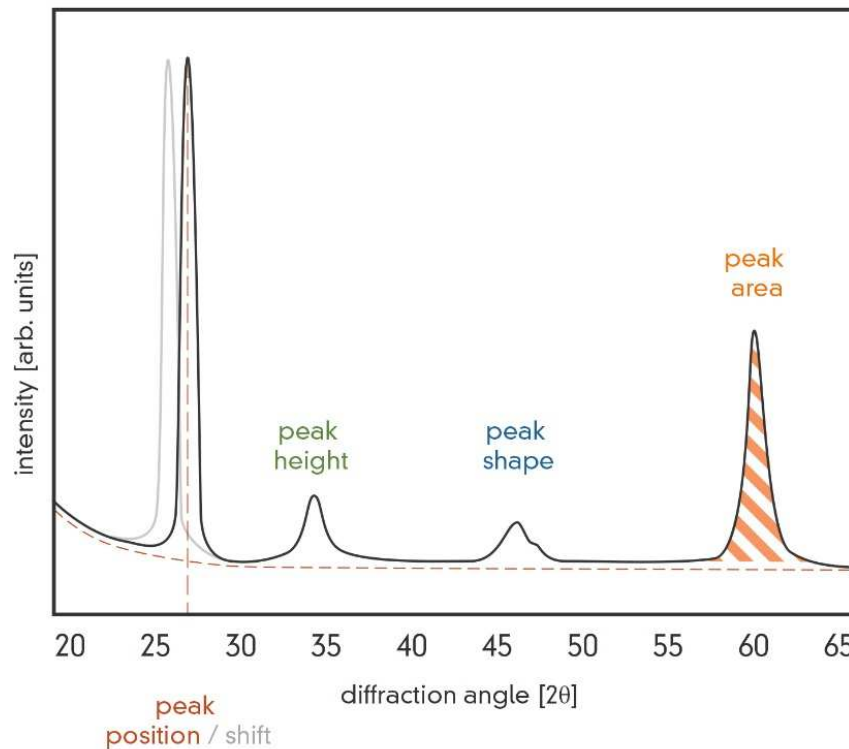


Fig. 26: Schematic illustration of the two most common XRD arrangements used to investigate thin films and powders, Bragg-Brentano (left) and Grazing Incidence (right), taken with permission from [50].

The information that can be gained from a diffraction pattern reaches from crystal structure and lattice parameters to crystallite size and even stresses can be determined by analysing X-ray diffractograms. Basic information that can be obtained from an XRD pattern is illustrated in Fig. 27.

The main information like crystal structure and lattice parameters can be obtained by analysing the peak position. Higher diffraction angles in the XRD pattern belong to smaller lattice plane distances and therefore to smaller lattice parameters, compare *Eq. 20*. In contrast lower diffraction angles are equivalent to larger lattice plane distances and therefore larger unit cells. Additionally, the peak height can be used to obtain information about the chemistry, due to the material specific diffraction. To gain information about the crystallite size the peak width, or more specifically the full width at half maximum (FWHM) can be considered to calculate the coherent diffracting domain size (CDS). Analysing the peak area can be used to get a quantification of the obtained phases. The peak shape e.g. shoulder formation would indicate the formation of a second phase out of solid solution as it occurs in Ti-Al-N [135]. Therefore, XRD can also be used to describe decomposition processes.



*Fig. 27: Schematic illustration of a XRD pattern including basic information used to determine crystal structure, lattice parameters, phase composition, and grain size, taken with permission from [50], originally from [136].*



## 5.1.2 Electron Microscopy

To investigate the morphology of thin films imaging methods such as microscopy are commonly used. The magnification and resolution are limited by the wavelength of the used radiation according to:

$$d = \frac{\lambda}{2n \sin(\alpha)} \quad \text{Eq. 22}$$

Within Eq. 22,  $\lambda$  is the wavelength,  $n$  the refracting index of the respective ambient medium and the term  $n \cdot \sin(\alpha)$  is called numerical aperture. According to the Abbe-equation, the resolution  $d$  can reach a minimum of around 140 nm based on a wavelength in the range of visible light of 400 nm [137]. Considering the above-mentioned limits, it is obvious that visible light, and therefore light microscopy, is not applicable for the investigation of coatings in the range of a view microns. Therefore, techniques such as scanning electron microscopy (SEM) and transmission electron microscopy (TEM) are used within this thesis to investigate the growth morphology of the synthesised thin films.

### 5.1.2.1 Scanning Electron Microscopy

Scanning electron microscopy uses a focused electron beam which interacts with the specimen surface leading to several useful phenomena. An electron source (electron gun) emits an electron beam, due to a high applied voltage of typically 5-30 keV, which is subsequently focused on the sample surface by magnetic lenses, see Fig. 28.



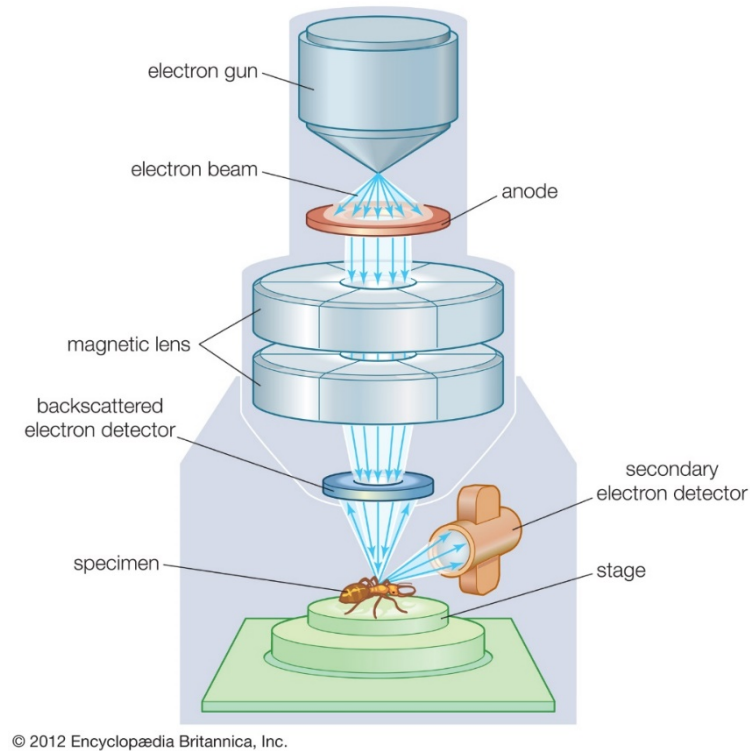


Fig. 28: Illustration of the basic setup of a scanning electron microscope [138].

To avoid the collision of electrons with air molecules SEM investigations are carried out under vacuum. The focused electron beam interacts with the sample surface leading to several phenomena which could be used to gain information about the sample, see Fig. 29.

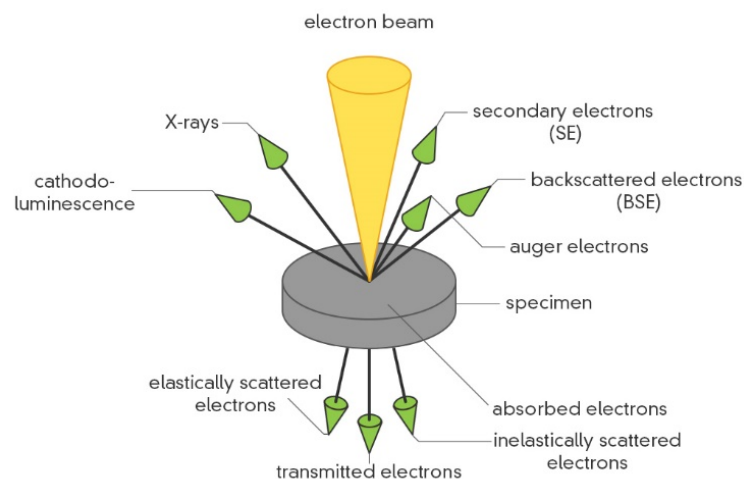


Fig. 29: Schematic illustration of basic electron-matter interaction processes during SEM investigations, taken with permission from [50], originally from [139].

Back scattered electrons (BSE) derive from to the reflection of electrons at the sample surface. Contrary, secondary electrons originate from impact ionisation, which means that these are

generated from the outer atomic shell (atoms of and close to the sample surface) by an incident electron beam. Besides BSE and SE, which are the most important ones, also so-called Auger electrons and cathodoluminescence can occur. Typically, back scattered electrons and secondary electrons are detected by specific devices and computationally processed to generate the image.

Imaging is the main but only one possible application of SEM. It is also often used for chemical analyses, making use of electromagnetic waves being generated through the previously mentioned electron-matter-interaction, see Fig. 29. Additionally, to the above-mentioned formation of secondary electrons by impact ionisation, another phenomenon due to the transition from outer to inner occupation occurs, namely the emission of characteristic X-ray radiation. The information gained of the occurring X-rays will be discussed in 5.2.1.

### 5.1.2.2 Transmission Electron Microscopy

Transmission electron microscopy (TEM) is due to its high resolution and magnification one of the most important investigation techniques in materials science to gain information of materials on the nanoscale. It allows for the analyses of extremely fine microstructural features, important for macroscopic properties.

Transmission electron microscopes consist, similar to a SEM, of an electron source from which electrons are emitted (e.g., a field emission gun) and subsequently accelerated towards the sample surface. As the electron beam reaches the sample surface, different effects come into play, which are used to gain further information/knowledge of the matter. In the basic transmission mode, electrons which transmit through the sample without being scattered or diffracted are used to create an image of the sample at the phosphor screen or a charge-coupled-device (CCD) camera. When operated in bright field (BF) transmission mode, the aperture allows the direct beam to pass, leading to images stemming from intensity reductions of the beam by interaction with the sample. In contrast, using the dark field (DF) mode leads, as the direct beam is blocked, to diffracted electrons which are used to create the image. Due to the strong interaction with the specimen, causing the diffracted beams, information about planar defects, stacking faults, or particle size could be gained from dark field images.

Information about the crystal structure of the specimen can be obtained by electron diffraction. By using an aperture with a defined diameter, it is possible to obtain information from a very small sample area. The technique is referred to as selected area electron diffraction (SAED), leading to diffraction patterns out of which structural information can be gained.

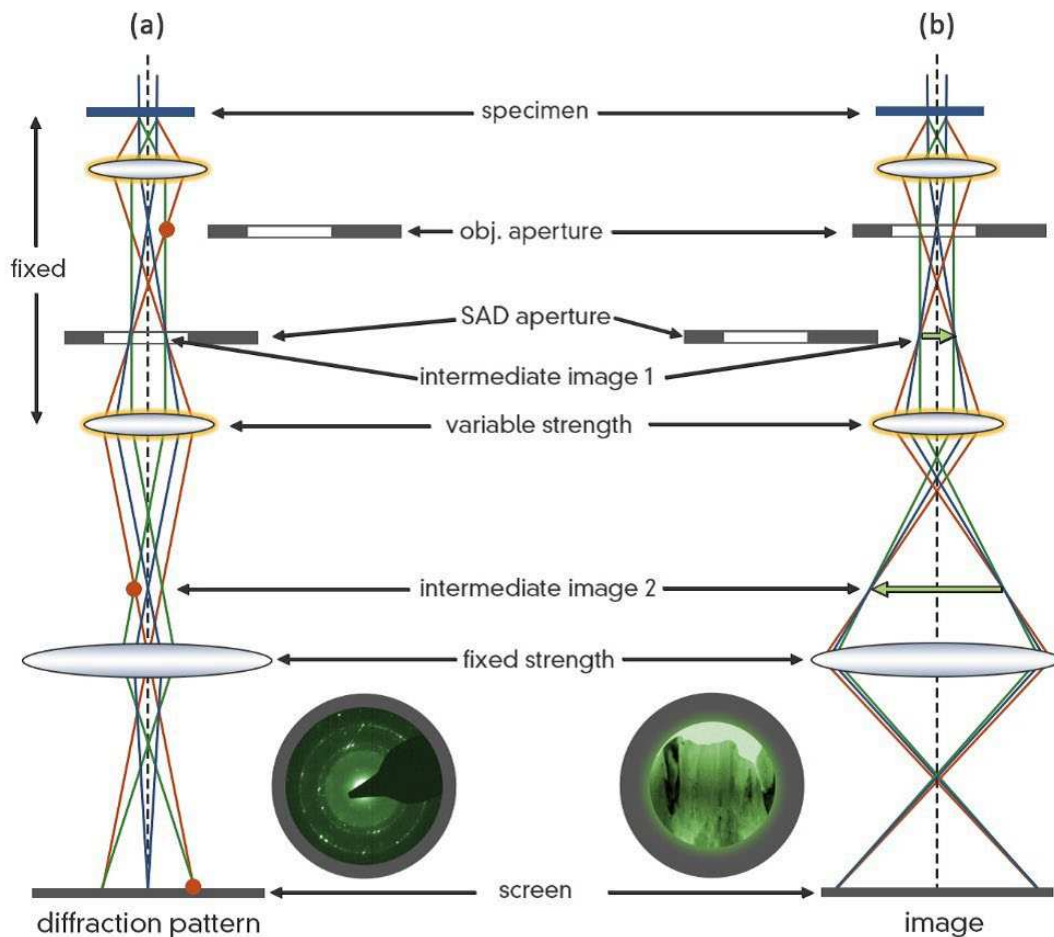


Fig. 30: Illustration of two TEM operation modes a) electron diffraction and b) bright field imaging taken with permission from [50], originally from [140].

Furthermore, similar to SEM, TEM features the possibility to perform chemical analysis. Therefore, the TEM is operated in the scanning mode. An EDS detector collects and processes X-ray signals that are generated due to the electron-matter-interaction within the specimen.

## 5.2 Chemical Analyses

To investigate the chemistry of the coatings in as deposited state and after annealing treatments several different methods are available. A very common technique to determine the chemical composition of coatings is energy dispersive X-ray spectroscopy (EDS). Other, more sophisticated, techniques are elastic recoil detection analysis or atom probe tomography. All these techniques were used to gain information of the chemical composition of the investigated coatings and will therefore be described in more detail.

### 5.2.1 Energy Dispersive X-Ray Spectroscopy

Energy dispersive X-ray spectroscopy is based on the emission of characteristic X-rays caused by irradiation by an electron beam. EDS can be conducted in combination with SEM or TEM. The required electron beam interacts with the sample surface atoms kicking out an electron from an inner electron shell. By replacing the ejected electron with an electron from a higher shell, the excess energy is emitted in form of X-rays with a characteristic wavelength, see Fig. 31.

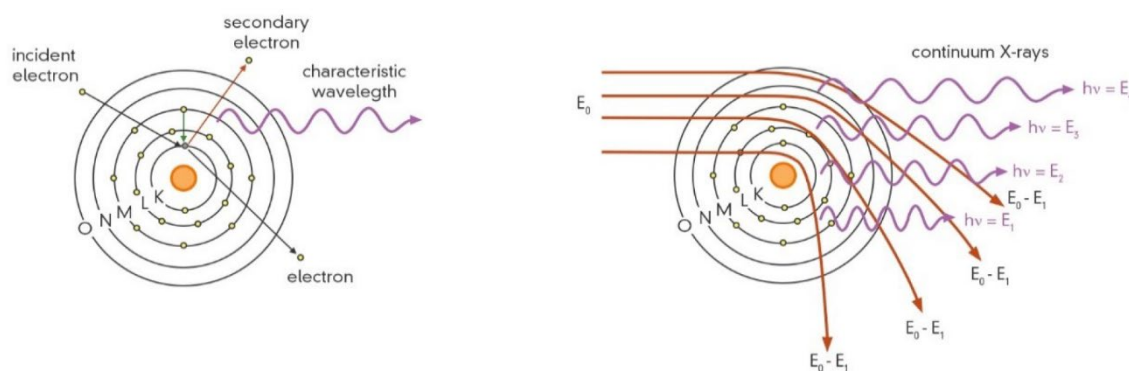


Fig. 31: Schematic illustration of electron atom interaction (left) and characteristic X-rays depending on the energy loss of the incident beam with energy  $E_0$  (right) taken with permission from [50], originally from [139].

Depending on the energy loss of the incident beam also the emitted X-rays differ in energy according to

$$E = h\nu = h \frac{c}{\lambda} \quad \text{Eq. 23}$$

In Eq. 23, E is the energy, h the Planck constant,  $\nu$  the frequency, c the speed of light, and  $\lambda$  the wavelength of the characteristic radiation. By detecting the characteristic X-rays and with the knowledge of the energy (acceleration voltage) of the incident beam the constituent elements can be determined according to the energy loss. Additionally, by analysing the intensity a quantitative statement can be given.

Although theoretically elements with an atomic number of  $Z \geq 5$  (boron) can be detected by windowless detectors, practically EDS is used to detect elements with  $Z \geq 10$  (sodium) and a quantity of at least 0.1 wt.%. Therefore, metal contents as well as their ratio can be considered as rather accurate, whereas the content of non-metals should be treated with caution. For non-metals such as nitrogen, oxygen, and boron an alternative method namely recoil detection analysis (ERDA) was used.

## 5.2.2 Atom Probe Tomography

Atom probe tomography (APT) is an analysis method used to generate 3D elemental maps of a sample. The resolution of this method is on the nanometre scale, making it the perfect tool for the visualisation nano-structures as well as precipitations in very small dimensions. Thereby, single atoms or atom clusters are field evaporated from a needle-shaped specimen. Besides the high positive voltage applied to the specimen, a voltage or laser pulse, depending on the electrical conductivity (conductive or insulating), with a frequency of several hundred kHz is used to evaporate the sample, see Fig. 32. By using a time-of-flight (ToF) setup to determine the mass-to-charge-ratio and therefore, the chemical nature of an atom or cluster. By using computer-assisted geometric algorithms, the position of the atom can be reconstructed, ideally in the initial tip shape, depending on the position where it hits the micro-channel plate detector. During the measurement the specimen is cryogenically cooled to keep a temperature of <100K to avoid diffusion.

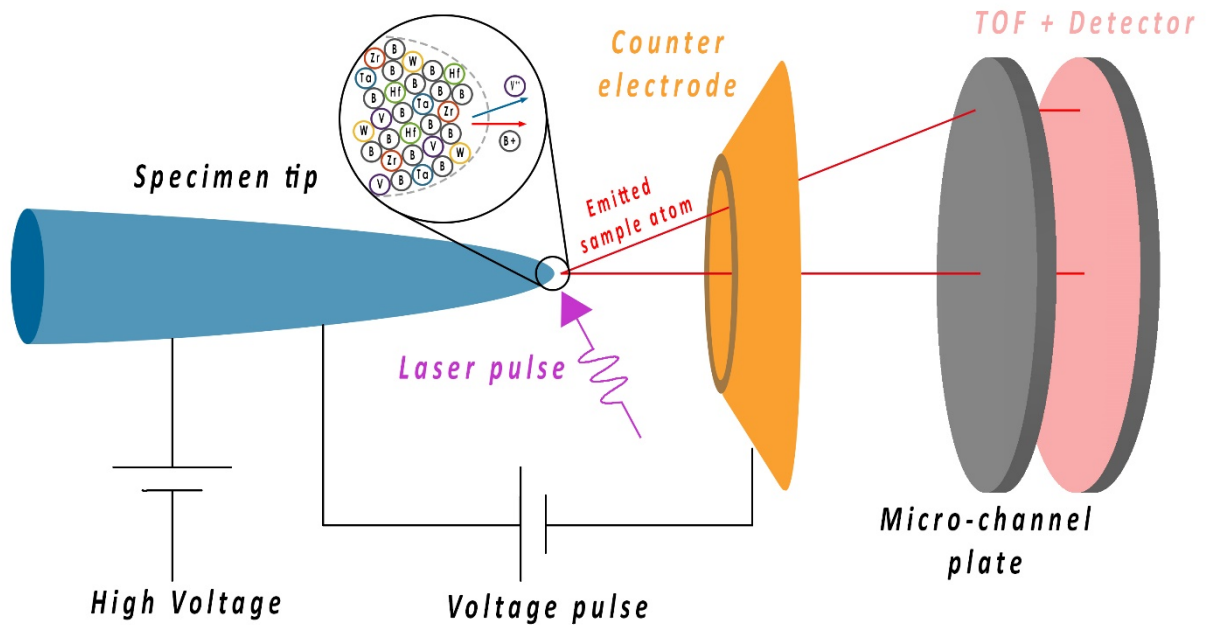


Fig. 32: Illustration of the basic components and the operating principle of atom probe tomography, adapted from [141].

However, the sample preparation has to be carried out using focussed ion beam (FIB) milling, which is rather time demanding. For thin films, this is a state-of-art technique to guarantee for proper specimen shapes. Limitations for APT arise from mass-to-charge overlaps, from the accuracy of the tip reconstruction as well as from inhomogeneous field evaporation rates of the sample material. Furthermore, it might be that strong clustering is not observable as the size of the clusters might exceed the sample size.

### 5.3 Mechanical Investigations

For most applications hard coatings are used for, the hardness, the Young's modulus as well as the fracture toughness are very important properties. To gain information about these nanoindentation and micro-cantilever tests are the methods of choice for thin film materials. These methods and information which could be gained from those tests will be addressed in the following paragraphs.

### 5.3.1 Nanoindentation

The knowledge of hardness and elastic modulus of coatings for protective application is essential. As the thickness of the applied coatings is less than 5  $\mu\text{m}$  conventional hardness measurement methods like Vickers or Brinell are not applicable. Therefore, nanoindentation is a commonly used method to gain information about the mechanical properties of thin films. In nanoindentation tests a Berkovich indenter tip is used to penetrate the sample surface. During the measurement the force as well as the penetration depth are simultaneous recorded. This results in a load displacement curve, see Fig. 33.

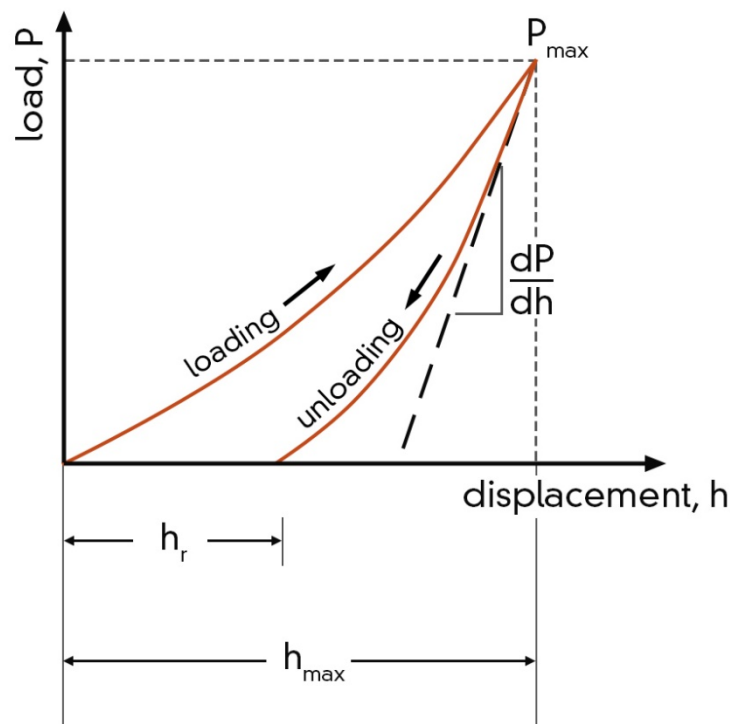


Fig. 33: Schematic illustration of a load-displacement curve of a nanoindentation test,  $P_{max}$  indicating the maximum load applied at the highest indentation depth  $h_{max}$ , and  $h_r$  being the residual displacement taken with permission from [50], originally from [142].

After recording load displacement curves for a certain loading range (typically 5-35 mN) the data is analysed after Oliver and Pharr [143]. As the influence of the substrate should be avoided to get accurate results of the film properties it is recommended that the penetration depth should not exceed 10 % of the coating thickness [144]. To correct the changes of the indenter geometry a so-called "area function" is periodically recorded. Therefore, indentation tests are done on fused silica



in different load ranges. By analysing the obtained load-displacement curves, a correction function, the area function, can be calculated which is used afterwards to correct measurements on samples to avoid the influence of changes of the indenter tip.

### 5.3.2 Micro-Cantilever Bending Tests

To gain information about the fracture toughness of thin films and coatings, micro-cantilever bending tests are a commonly used method. Thereby, the substrate is usually removed by etching with KOH to get free-standing coating material. Subsequently, cantilevers with an initial notch are prepared by FIB out of the free-standing coating material, see Fig. 34 a.

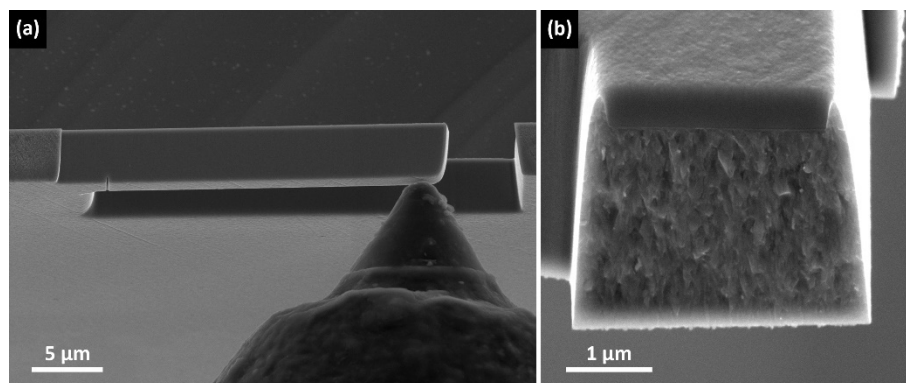


*Fig. 34: SEM images of a micro-cantilever bending test (a) free-standing cantilever with initial notch and picoindenter and (b) cross-section of fractured cantilever*

To evaluate the fracture toughness of the coating, the prepared cantilevers are loaded by a picoindenter which is placed in an SEM, see Fig. 34 a. The load is continuously increased and simultaneously the load as well as the displacement is recorded until the cantilever fractures. By evaluating the recorded load-displacement curves and the fracture cross-section of the cantilever, see Fig. 34 b, the fracture toughness of the coating material can be calculated according to Matoy et al. [145].



## 5.4 Thermal Analyses

To investigate the thermal stability of the deposited coatings, several techniques are available. Within this thesis, vacuum annealing of powdered coating material as well as of coatings on sapphire substrates with subsequently XRD and nanoindentation measurements was used to determine the structure and mechanical properties of coatings after being heated and held at a certain temperature. Additionally, differential scanning calorimetry (DSC) was carried out to observe the temperature range where phase transformations occur. The detailed procedure and operating modes will be described in the following paragraphs.

### 5.4.1 Vacuum Annealing

As the application of the investigated coatings usually takes place at elevated temperatures, the information about the behaviour of the coating after being heated is of utmost importance. To investigate the coatings' behaviour upon heat treatment, vacuum annealing treatments were carried out in a vacuum furnace. For the annealing treatments the vacuum chamber is pumped down to a certain vacuum ( $\sim 7 \cdot 10^{-4}$  Pa) and then heated up to the target temperature. Holding time as well as heating rate can be varied in a wide range. During the heating cycle, the samples undergo phase transitions or decomposition. After the heat treatment, the samples are passively cooled down with a cooling rate of about 50- 90 K/min to a temperature of  $\sim 300$  °C. The standard annealing program for vacuum annealing is shown in Fig. 35.

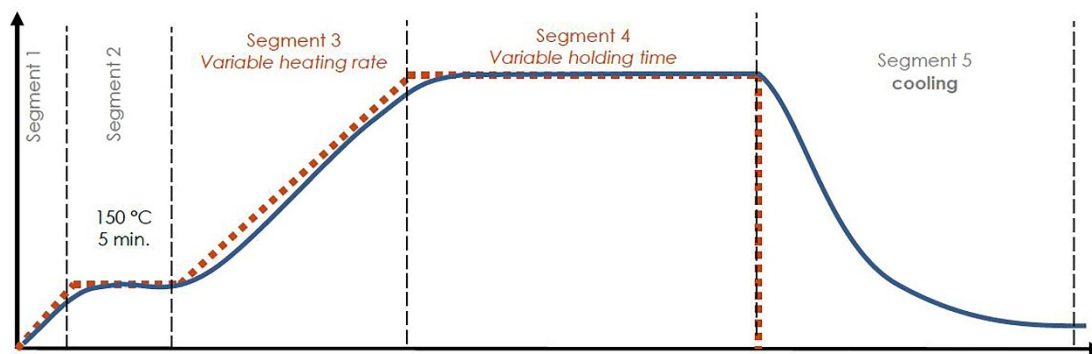


Fig. 35: Schematic illustration of a standard annealing treatment cycle.

As the cooling rate is rather high, the preceding phase transitions are non-reversible. As there is no active cooling system the cooling rate down to room temperature is significantly decreasing with decreasing furnace temperature. To investigate the occurring softening processes, phase transitions as well as decomposition processes, the samples are subsequently investigated by XRD and nanoindentation.

## 5.4.2 Differential Scanning Calorimetry

Differential scanning calorimetry (DSC) is a thermo-analytical technique that is based on the difference of the heat amount required to increase the temperature of a sample compared to a reference. Therefore, the enthalpy that is generated or consumed during physical processes or chemical reactions, such as oxidation or decomposition, can be measured. This includes reactions causing an increase of the enthalpy (endothermic reactions), like melting or evaporating, and reactions that decrease the enthalpy (exothermic reactions), such as oxidation and crystallisation.

Additionally, the sample mass is simultaneously measured by thermo-gravimetric analysis (TGA), allowing for an interpretation of the reactions in the temperature range of interest. This facilitates to investigate the gain and loss of weight by the incorporation or release of a species upon annealing (e.g., by oxidation or dissociation processes of nitrides to release nitrogen).

In this work a Netzsch Jupiter F1 differential scanning calorimeter with thermo-gravimetric analysis (TGA-DSC) equipped with a Rhodium furnace was used to investigate powdered free-standing coating material regarding the thermal stability and phase transformations.

## 6 References

- [1] B. Cantor, I.T.H. Chang, P. Knight, A.J.B. Vincent, *Mater. Sci. Eng. A* 375–377 (2004) 213–218.
- [2] J.-W. Yeh, S.-K. Chen, S.-J. Lin, J.-Y. Gan, T.-S. Chin, T.-T. Shun, C.-H. Tsau, S.-Y. Chang, *Adv. Eng. Mater.* 6 (2004) 299–303.
- [3] J.W. Yeh, *Ann. Chim. Sci. Des Mater.* 31 (2006) 633–648.
- [4] M.F. Ashby, in: *M.F.B.T.-M.S. in M.D.* (Fourth E. Ashby (Ed.), Butterworth-Heinemann, Oxford, 2011, pp. 97–124.
- [5] M. Telford, *III-Vs Rev.* 17 (2004) 36–39.
- [6] M.J. Yao, K.G. Pradeep, C.C. Tasan, D. Raabe, *Scr. Mater.* 72–73 (2014) 5–8.
- [7] Y.F. Ye, Q. Wang, J. Lu, C.T. Liu, Y. Yang, *Mater. Today* 19 (2016) 349–362.
- [8] K.M. Youssef, A.J. Zaddach, C. Niu, D.L. Irving, C.C. Koch, *Mater. Res. Lett.* 3 (2014) 95–99.
- [9] Y. Deng, C.C. Tasan, K.G. Pradeep, H. Springer, A. Kostka, D. Raabe, *Acta Mater.* 94 (2015) 124–133.
- [10] B. Gludovatz, A. Hohenwarter, D. Catoor, E.H. Chang, E.P. George, R.O. Ritchie, 345 (2014) 1153–1159.
- [11] C.Y. Hsu, W.R. Wang, W.Y. Tang, S.K. Chen, J.W. Yeh, *Adv. Eng. Mater.* 12 (2010) 44–49.
- [12] C.C. Juan, M.H. Tsai, C.W. Tsai, C.M. Lin, W.R. Wang, C.C. Yang, S.K. Chen, S.J. Lin, J.W. Yeh, *Intermetallics* 62 (2015) 76–83.
- [13] S. Rajasekhara, L.P. Karjalainen, A. Kyröläinen, P.J. Ferreira, in: Y. Weng, H. Dong, Y. Gan (Eds.), Springer Berlin Heidelberg, Berlin, Heidelberg, 2011, pp. 371–384.
- [14] O.N. Senkov, S. V. Senkova, C. Woodward, D.B. Miracle, *Acta Mater.* 61 (2013) 1545–1557.
- [15] O.N. Senkov, G.B. Wilks, J.M.M. cott, D.B. Miracle, *Intermetallics* 19 (2011) 698–706.
- [16] O.N. Senkov, C.F. Woodward, *Mater. Sci. Eng. A* 529 (2011) 311–320.
- [17] A. C. Vlasveld, S.G. Harris, E.D. Doyle, D.B. Lewis, W.D. Munz, *Surf. Coatings Technol.* 149 (2002) 217–224.
- [18] W. Münz, *J. Vac. Sci. Technol. A Vacuum, Surfaces, Film.* 4 (1986) 2717–2725.
- [19] S.A. Glatz, C.M. Koller, H. Bolvardi, S. Kolozsvári, H. Riedl, P.H. Mayrhofer, *Surf. Coatings Technol.* 311 (2017) 330–336.
- [20] S.A. Glatz, V. Moraes, C.M. Koller, H. Riedl, H. Bolvardi, S. Kolozsvári, P.H. Mayrhofer, *J. Vac. Sci. Technol. A Vacuum, Surfaces, Film.* 35 (2017) 061515.

- [21] R. Hollerweger, H. Riedl, J. Paulitsch, M. Arndt, R. Rachbauer, P. Polcik, S. Primig, P.H. Mayrhofer, *Surf. Coatings Technol.* 257 (2014) 78–86.
- [22] R. Rachbauer, D. Holec, P.H. Mayrhofer, *Surf. Coatings Technol.* 211 (2012) 98–103.
- [23] R. Rachbauer, D. Holec, P.H. Mayrhofer, *IEEE Trans. Inf. Theory* 39 (1993) 999–1013.
- [24] W.M. Seidl, M. Bartosik, S. Kolozsvári, H. Bolvardi, P.H. Mayrhofer, *Vacuum* 150 (2018) 24–28.
- [25] S.A. Glatz, H. Bolvardi, S. Kolozsvári, C.M. Koller, H. Riedl, P.H. Mayrhofer, *Surf. Coatings Technol.* 332 (2017) 275–282.
- [26] S.A. Glatz, R. Hollerweger, P. Polcik, R. Rachbauer, J. Paulitsch, P.H. Mayrhofer, *Surf. Coatings Technol.* 266 (2015) 1–9.
- [27] H. Asanuma, F.F. Klimashin, P. Polcik, S. Kolozsvári, H. Riedl, P.H. Mayrhofer, *Thin Solid Films* 688 (2019) 137239.
- [28] H. Asanuma, F.F. Klimashin, P. Polcik, S. Kolozsvári, H. Riedl, P.H. Mayrhofer, *Surf. Coatings Technol.* 372 (2019) 26–33.
- [29] T.K. Chen, T.T. Shun, J.W. Yeh, *Surf. Coatings Technol.* 188–189 (2004) 193–200.
- [30] K.H. Cheng, C.H. Weng, C.H. Lai, S.J. Lin, *Thin Solid Films* 517 (2009) 4989–4993.
- [31] S.-Y. Chang, M.-K. Chen, D.-S. Chen, *J. Electrochem. Soc.* 156 (2009) G37.
- [32] V. Braic, M. Balaceanu, M. Braic, A. Vladescu, S. Panseri, A. Russo, *J. Mech. Behav. Biomed. Mater.* 10 (2012) 197–205.
- [33] C.-H.H. Tsau, Y.-H.H. Chang, *Entropy* 15 (2013) 5012–5021.
- [34] B. Ren, S.Q. Yan, R.F. Zhao, Z.X. Liu, *Surf. Coatings Technol.* 235 (2013) 764–772.
- [35] D.-C. Tsai, M.-J. Deng, Z.-C. Chang, B.-H. Kuo, E.-C. Chen, S.-Y. Chang, F.-S. Shieu, (2015).
- [36] K. Yalamanchili, F. Wang, I.C. Schramm, J.M. Andersson, M.P. Johansson Jöesaar, F. Tasnádi, F. Mücklich, N. Ghafoor, M. Odén, *Thin Solid Films* (2017).
- [37] A.A. Bagdasaryan, A. V. Pshyk, L.E. Coy, M. Kempínski, A.D. Pogrebnyak, V.M. Beresnev, S. Jurga, *Mater. Lett.* 229 (2018) 364–367.
- [38] W.G. Fahrenholtz, G.E. Hilmas, *Scr. Mater.* 129 (2017) 94–99.
- [39] S. Jayaraman, Y. Yang, D.Y. Kim, G.S. Girolami, J.R. Abelson, *J. Vac. Sci. Technol. A Vacuum, Surfaces, Film.* 23 (2005) 1619–1625.
- [40] J. Sung, D.M. Goedde, G.S. Girolami, J.R. Abelson, *J. Appl. Phys.* 91 (2002) 3904–3911.
- [41] P.H. Mayrhofer, A. Kirnbauer, P. Ertelthaler, C.M. Koller, *Scr. Mater.* 149 (2018) 93–97.
- [42] V. Moraes, C. Fuger, V. Paneta, D. Primetzhofer, P. Polcik, H. Bolvardi, M. Arndt, H. Riedl, P.H.

- Mayrhofer, *Scr. Mater.* 155 (2018) 5–10.
- [43] V. Moraes, L. Zauner, T. Wojcik, M. Arndt, P. Polcik, H. Riedl, P.H. Mayrhofer, *Acta Mater.* 186 (2020) 487–493.
- [44] V. Moraes, H. Riedl, C. Fuger, P. Polcik, H. Bolvardi, D. Holec, P.H. Mayrhofer, *Sci. Rep.* 8 (2018) 1–9.
- [45] J. Alami, P. Eklund, J.M. Andersson, M. Lattemann, E. Wallin, J. Bohlmark, P. Persson, U. Helmersson, *Thin Solid Films* 515 (2007) 3434–3438.
- [46] M. Aguilar-Frutis, M. Garcia, C. Falcony, *Appl. Phys. Lett.* 72 (1998) 1700–1702.
- [47] P.J. Kelly, R.D. Arnell, *J. Vac. Sci. Technol. A Vacuum, Surfaces, Film.* 17 (1999) 945.
- [48] C.H. Lin, H.L. Wang, M.H. Hon, *Thin Solid Films* 283 (1996).
- [49] M.W. Zemansky, R.H. Dittman, *Heat and Thermodynamics*, The McGraw-Hill Companies : Inc., New York, 1997.
- [50] C.M. Koller, *Triggering the Phase Evolution within TiAlN- and (Al,Cr)<sub>2</sub>O<sub>3</sub>- Based Coatings by Alloying and Microstructural Concepts*, Vienna University of Technology, 2015.
- [51] H.J. Bargel, H. Hilbrans, G. Schulze, K.H. Hübner, O. Krüger, *Werkstoffkunde*, Springer Berlin Heidelberg, 2005.
- [52] P.H. Mayrhofer, *Werkstoffkunde Metallischer Werkstoffe*, 2019.
- [53] E. Arzt, *Acta Mater.* 46 (1998) 5611–5626.
- [54] R.L. Fleischer, *Acta Metall.* 9 (1961) 996–1000.
- [55] J.R. Greer, *Nat. Mater.* 12 (2013) 689–690.
- [56] E.O. Hall, *Nature* 173 (1954).
- [57] S.P. Taguchi, S. Ribeiro, *J. Mater. Process. Technol.* 147 (2004) 336–342.
- [58] E. Huber, S. Hofmann, *Surf. Coatings Technol.* 68–69 (1994) 64–69.
- [59] N. Boukis, N. Claussen, K. Ebert, R. Janssen, M. Schacht, *J. Eur. Ceram. Soc.* 17 (1997) 71–76.
- [60] A. Glaser, S. Surnev, F.P. Netzer, N. Fateh, G.A. Fontalvo, C. Mitterer, *Surf. Sci.* 601 (2007) 1153–1159.
- [61] Y.C. Chim, X.Z. Ding, X.T. Zeng, S. Zhang, *Thin Solid Films* 517 (2009) 4845–4849.
- [62] V. Shankar Rao, *Mater. Sci. Eng. A* 364 (2004) 232–239.
- [63] I.M. Wolff, L.E. Iorio, T. Rumpf, P.V.T. Scheers, J.H. Potgieter, *Mater. Sci. Eng. A* 241 (1998) 264–276.
- [64] D.A. Porter, K.E. Easterling, M.Y. Sherif, *Phase Transformations in Metals and Alloys*, Third Edition, 2009.

- [65] J.W. Martin, *Precipitation Hardening: Theory and Applications*, Butterworth-Heinemann, 2012.
- [66] P.H. Mayrhofer, R. Rachbauer, D. Holec, F. Rovere, J.M. Schneider, *Protective Transition Metal Nitride Coatings*, 2014.
- [67] M. Birks, G.H. Meier, *Introduction to High Temperature Oxidation of Metals*, Edwar Arnold Ltd., London, 1983.
- [68] K.R. Lawless, *Reports Prog. Phys.* 37 (1974) 231–316.
- [69] J.M. West, (1986).
- [70] H.J. Grabke, M. Schütze, *Oxidation of Intermetallics*, John Wiley & Sons, 2008.
- [71] N. Birks, G.H. Meier, F.S. Pettit, *Introduction to the High Temperature Oxidation of Metals*, 2nd ed., Cambridge University Press, Cambridge, 2006.
- [72] F.J. Harvey, *Met. Trans* 5 (1974) 1189–1192.
- [73] A.T. Nelson, E.S. Sooby, Y.J. Kim, B. Cheng, S.A. Maloy, *J. Nucl. Mater.* 448 (2014) 441–447.
- [74] J.-W.W. Yeh, S.-K.K. Chen, J.-Y.Y. Gan, S.-J.J. Lin, T.-S.S. Chin, T.-T.T. Shun, C.-H.H. Tsau, S.Y. Chang, J.-Y.Y. Gan, S.-K.K. Chen, T.-T.T. Shun, C.-H.H. Tsau, S.-Y. Chou, *Metall. Mater. Trans. A* 35 (2004) 2533–2536.
- [75] D.B. Miracle, O.N. Senkov, *Acta Mater.* 122 (2017) 448–511.
- [76] B.S. Murty, J.W. Yeh, S. Ranganathan, P.P. Bhattacharjee, *High-Entropy Alloy*. (2019) 1–12.
- [77] D.B. Miracle, J.D. Miller, O.N. Senkov, C. Woodward, M.D. Uchic, J. Tiley, *Entropy* 16 (2014) 494–525.
- [78] J.W. Yeh, *Ann. Chim. Sci. Des Mater.* 31 (2006) 633–648.
- [79] S. Ranganathan, *Curr. Sci.* 85 (2003) 1404–1406.
- [80] O.N. Senkov, C.F. Woodward, *Mater. Sci. Eng. A* 529 (2011) 311–320.
- [81] T.M. Butler, K.J. Chaput, J.R. Dietrich, O.N. Senkov, *J. Alloys Compd.* 729 (2017) 1004–1019.
- [82] O.N. Senkov, G.B. Wilks, D.B. Miracle, C.P. Chuang, P.K. Liaw, *Intermetallics* 18 (2010) 1758–1765.
- [83] Z.D.D. Han, N. Chen, S.F.F. Zhao, L.W.W. Fan, G.N.N. Yang, Y. Shao, K.F.F. Yao, *Intermetallics* 84 (2017).
- [84] Y. Mu, H. Liu, Y. Liu, X. Zhang, Y. Jiang, T. Dong, *J. Alloys Compd.* (2017).
- [85] O.N. Senkov, S. V. Senkova, D.M. Dimiduk, C. Woodward, D.B. Miracle, *J. Mater. Sci.* 47 (2012) 6522–6534.
- [86] Y. Zou, P. Okle, H. Yu, T. Sumigawa, T. Kitamura, S. Maiti, W. Steurer, R. Spolenak, *Scr. Mater.*

- 128 (2017) 95–99.
- [87] R. Feng, M.C. Gao, C. Zhang, W. Guo, J.D. Poplawsky, F. Zhang, J.A. Hawk, J.C. Neuefeind, Y. Ren, P.K. Liaw, *Acta Mater.* 146 (2018) 280–293.
- [88] D. Raabe, C.C. Tasan, H. Springer, M. Bausch, Ā. Cemal, C.C. Tasan, H. Springer, M. Bausch, *Steel Res. Int.* (2015).
- [89] N.D. Stepanov, D.G. Shaysultanov, G.A. Salishchev, M.A. Tikhonovsky, *Mater. Lett.* 142 (2015) 153–155.
- [90] N.D. Stepanov, N.Y. Yurchenko, V.S. Sokolovsky, M.A. Tikhonovsky, G.A. Salishchev, *Mater. Lett.* 161 (2015) 136–139.
- [91] K.K. Tseng, Y.C. Yang, C.C. Juan, T.S. Chin, C.W. Tsai, J.W. Yeh, *Sci. China Technol. Sci.* (2017) 1–5.
- [92] Y. Lederer, C. Toher, K.S. Vecchio, S. Curtarolo, *Acta Mater.* 159 (2018) 364–383.
- [93] L. Chen, J. Paulitsch, Y. Du, P.H. Mayrhofer, *Surf. Coatings Technol.* 206 (2012).
- [94] L. Chen, Z.Q. Liu, Y.X. Xu, Y. Du, *Surf. Coatings Technol.* 275 (2015) 289–295.
- [95] C.M. Koller, R. Hollerweger, C. Sabitzer, R. Rachbauer, S. Kolozsvári, J. Paulitsch, P.H. Mayrhofer, *Surf. Coatings Technol.* 259 (2014) 599–607.
- [96] P. Villars, K. Cenzual, eds., (n.d.).
- [97] K. Momma, F. Izumi, *J. Appl. Crystallogr.* 44 (2011) 1272–1276.
- [98] W. Hofmann, W. Jäniche, *Naturwissenschaften* 23 (1935) 851.
- [99] M. Frotscher, W. Klein, J. Bauer, C.M. Fang, J.F. Halet, A. Senyshyn, C. Baehtz, B. Albert, *Zeitschrift Fur Anorg. Und Allg. Chemie* 633 (2007) 2626–2630.
- [100] C. Fuger, V. Moraes, R. Hahn, H. Bolvardi, P. Polcik, H. Riedl, P.H. Mayrhofer, *MRS Commun.* 9 (2019) 375–380.
- [101] D. Music, J.M. Schneider, (2017).
- [102] B.S. Murty, J.W. Yeh, S. Ranganathan, *High Entropy Alloys*, Elsevier, 2014.
- [103] S.Y. Chang, Y.C. Huang, C.E. Li, H.F. Hsu, J.W. Yeh, S.J. Lin, *Jom* 65 (2013) 1790–1796.
- [104] S.Y. Chang, M.K. Chen, D.S. Chen, *J. Electrochem. Soc.* 156 (2009).
- [105] P.K. Huang, J.W. Yeh, *Surf. Coatings Technol.* 203 (2009) 1891–1896.
- [106] S.C. Liang, Z.C. Chang, D.C. Tsai, Y.C. Lin, H.S. Sung, M.J. Deng, F.S. Shieu, *Appl. Surf. Sci.* 257 (2011) 7709–7713.
- [107] Y. Liang, P. Wang, Y. Wang, Y. Dai, Z. Hu, D.E. Tranca, R. Hristu, S.G. Stanciu, A. Toma, G.A. Stanciu, X. Wang, E. Fu, *Materials (Basel)*. 12 (2019).



- [108] M.H. Tsai, C.W. Wang, C.H. Lai, J.W. Yeh, J.Y. Gan, *Appl. Phys. Lett.* 92 (2008) 90–93.
- [109] M.-H. Tsai, C.-W. Wang, C. Tsai, W. Shen, J. Yeh, J.-Y. Gan, W.-W. Wu, *J. Electrochem. Soc.* 158 (2011) 1161–1165.
- [110] J. Gild, A. Wright, K. Quiambao-Tomko, M. Qin, J.A. Tomko, M. Shafkat bin Hoque, J.L. Braun, B. Bloomfield, D. Martinez, T. Harrington, K. Vecchio, P.E. Hopkins, J. Luo, *Ceram. Int.* 46 (2020) 6906–6913.
- [111] S. Failla, P. Galizia, S. Fu, S. Grasso, D. Sciti, *J. Eur. Ceram. Soc.* 40 (2020) 588–593.
- [112] L. Feng, W.G. Fahrenholtz, G.E. Hilmas, *J. Am. Ceram. Soc.* 103 (2020) 724–730.
- [113] Y. Zhang, W.M. Guo, Z. Bin Jiang, Q.Q. Zhu, S.K. Sun, Y. You, K. Plucknett, H.T. Lin, *Scr. Mater.* 164 (2019) 135–139.
- [114] C.M. Rost, E. Sachet, T. Borman, A. Moballegh, E.C. Dickey, D. Hou, J.L. Jones, S. Curtarolo, J.P. Maria, *Nat. Commun.* 6 (2015) 1–8.
- [115] J.L. Braun, C.M. Rost, M. Lim, A. Giri, D.H. Olson, G.N. Kotsonis, G. Stan, D.W. Brenner, J.P. Maria, P.E. Hopkins, *Adv. Mater.* 30 (2018) 1–8.
- [116] M.R. Chellali, A. Sarkar, S.H. Nandam, S.S. Bhattacharya, B. Breitung, H. Hahn, L. Velasco, *Scr. Mater.* 166 (2019) 58–63.
- [117] K. Chen, X. Pei, L. Tang, H. Cheng, Z. Li, C. Li, X. Zhang, L. An, *J. Eur. Ceram. Soc.* 38 (2018) 4161–4164.
- [118] J. Dąbrowa, M. Stygar, A. Mikuła, A. Knapik, K. Mroczka, W. Tejchman, M. Danielewski, M. Martin, *Mater. Lett.* 216 (2018) 32–36.
- [119] P. Sarker, T. Harrington, C. Toher, C. Oses, M. Samiee, J.P. Maria, D.W. Brenner, K.S. Vecchio, S. Curtarolo, *Nat. Commun.* 9 (2018) 1–10.
- [120] A. Sarkar, Q. Wang, A. Schiele, M.R. Chellali, S.S. Bhattacharya, D. Wang, T. Brezesinski, H. Hahn, L. Velasco, B. Breitung, *Adv. Mater.* 1806236 (2019).
- [121] Y. Sharma, B.L. Musico, X. Gao, C. Hua, A.F. May, A. Herklotz, A. Rastogi, D. Mandrus, J. Yan, H.N. Lee, M.F. Chisholm, V. Keppens, T.Z. Ward, *Phys. Rev. Mater.* 2 (2018) 060404.
- [122] M.I. Lin, M.H. Tsai, W.J. Shen, J.W. Yeh, *Thin Solid Films* 518 (2010) 2732–2737.
- [123] C.H. Tsau, Z.Y. Hwang, S.K. Chen, *Adv. Mater. Sci. Eng.* 2015 (2015) 1–7.
- [124] C.H. Tsau, Y.C. Yang, C.C. Lee, L.Y. Wu, H.J. Huang, *Procedia Eng.* 36 (2012) 246–252.
- [125] P.H. Mayrhofer, *Skriptum Zur Vorlesung: Oberflächentechnik*, TU Wien, 2014.
- [126] C.M. Koller, *Thermal Stability and Oxidation Resistance of Ti-Al-N / Ta-Al-N Multilayers*, Montanuniversität Leoben, 2012.



- [127] M. Ohring, *Mater. Sci. Thin Film.* (2002) 203–275.
- [128] B.A. Movchan, A. V Demchishin, (1969).
- [129] R. Messier, *J. Vac. Sci. Technol. A Vacuum, Surfaces, Film.* 2 (1984) 500.
- [130] J. A. Thornton, *J. Vac. Sci. Technol.* 11 (1974) 666.
- [131] J. Musil, *Vacuum* 50 (1998) 363–372.
- [132] D. Depla, S. Mahieu, *Reactive Sputter Deposition*, Springer, 2008.
- [133] A. Anders, *Thin Solid Films* 518 (2010) 4087–4090.
- [134] P.W.H. Bragg, W.L. Bragg, 17 (1913) 428–438.
- [135] P.H. Mayrhofer, A. Hörling, L. Karlsson, J. Sjöln, T. Larsson, C. Mitterer, L. Hultman, *Appl. Phys. Lett.* 83 (2003) 2049–2051.
- [136] F. Girgsdies, *X-Ray Powder Diffraction in Catalysis, Lecture Notes*, 2006.
- [137] E. Abbe, *Arch. Für Mikroskopische Anat.* 9 (1873) 413–418.
- [138] *Encyclopædia Britannica*, (n.d.).
- [139] U. JEOL, *Energy Table EDS Anal.* 100 (n.d.) 14001.
- [140] D.B. Williams, C.B. Carter, *Mater. Sci.* 1–4 (2009) 760.
- [141] E. Aschauer, *Dissertation Mo-Si-B Based Coatings : Compositional and Architectural Approaches for High Temperature Environments*, 2018.
- [142] S. V Hainsworth, H.W. Chandler, T.F. Page, *J. Mater. Res.* 11 (1996) 1987–1995.
- [143] W.C. Oliver, G.M. Pharr, (1992).
- [144] DIN-Normenausschuss *Materialprüfung (NMP)\*Materials Testing Standards Committee*, (2015) 54.
- [145] K. Matoy, H. Schönherr, T. Detzel, T. Schöberl, R. Pippan, C. Motz, G. Dehm, *Thin Solid Films* 518 (2009) 247–256.

# 7 Contribution to the Field

## 7.1 First Author Publications

### Publication I

A. Kirnbauer, A. Kretschmer, C.M. Koller, T. Wojcik, V. Paneta, M. Hans, J.M. Schneider, P. Polcik, P.H. Mayrhofer

*Mechanical properties and thermal stability of reactively sputtered multi-principal-metal Hf-Ta-Ti-V-Zr nitrides*

*Surface and Coatings Technology, doi: 10.1016/j.surfcoat.2020.125674*

Crystalline (Hf,Ta,Ti,V,Zr)N nitride thin films, with a high-entropy metal-sublattice, were synthesised at 440 °C by reactive magnetron sputtering using an equimolar Hf-Ta-Ti-V-Zr-compound target. The coatings show a single-phase fcc structure with a Me:N ratio of 1:1 for  $N_2/(Ar+N_2)$  flow-rate-ratios ( $f_{N_2}$ ) between 30 and 45 %. For higher  $f_{N_2}$  a small fraction of an additional phase besides the fcc-matrix is detected by X-ray diffraction (XRD) and selected area electron diffraction (SAED). The chemical composition for all coatings studied (prepared with  $f_{N_2}$  between 30 and 60 %) is very similar. Furthermore, also the hardness (H) values between 30.0 and 34.0 GPa and indentation moduli of ~460 GPa are very similar for all coatings. Detailed atom probe tomography (APT) investigations show a homogenous distribution of all elements within our fcc-(Hf,Ta,Ti,V,Zr)N even after vacuum-annealing at 1300 °C. While H decreased from 32.5 to 28.1 GPa upon annealing, the coating is still single-phase fcc structured and still exhibits a high defect density (expressed by XRD and SAED features, transmission electron microscopy contrast, and grain sizes). Only after vacuum-annealing at 1500 °C, XRD as well as APT reveal the formation of hexagonal structured (Ta,V)<sub>2</sub>N. The onset for the observed nitrogen-loss – detected by thermogravimetric analysis – is ~1350 °C.

Based on our results we can conclude that the sluggish diffusion within our fcc-(Hf,Ta,Ti,V,Zr)N guarantees the single-phase fcc structure up to 1300 °C, although *ab initio* based calculations would suggest the lower-entropy products [fcc-(Hf,Zr)N, fcc-(Ta,V)N, and fcc-TiN] and [fcc-(Hf,Zr)N and fcc-(Ta,Ti,V)N] to be energetically more stable up to 1302 K.

## Publication II

R. Hahn, A. Kirnbauer, M. Bartosik, S. Kolozsvári, and P.H. Mayrhofer

*Toughness of Si alloyed high-entropy nitride coatings*

*Mater. Lett.* 251 (2019) 238–240. doi: 10.1016/j.matlet.2019.05.074.

In this contribution, we present micromechanical experiments of reactively magnetron sputtered high-entropy nitride thin films. Single-phase fcc-(Al,Ta,Ti,V,Zr)N with nearly equimolar metal-fractions as well as a Si-alloyed sample were investigated. The (Al,Ta,Ti,V,Zr)N coating exhibits a hardness of  $30.7 \pm 1.5$  GPa and a fracture toughness of  $2.4 \text{ MPa}\sqrt{m}$ . By alloying 5 at% Si to this high-entropy nitride a nanocrystalline microstructure is observed in the fracture cross-sections. Although the hardness ( $29.2 \pm 0.8$  GPa) and fracture toughness ( $2.3 \pm 0.1 \text{ MPa}\sqrt{m}$ ) are not significantly influenced, the increase of the elastic response leads to an increase of the elastic strain to failure of 33 %. This indicates a significantly improved damage tolerance for the Si alloyed (Al,Ta,Ti,V,Zr)N. This is of high significance, as the elastic deformability of hard coatings also determines its damage tolerance.

Furthermore, this study shows that the addition of Si—considering the decrease of Young’s modulus by 100 GPa, the essentially constant  $K_{IC}$ , and the relation  $K_{IC} \propto \sqrt{G \cdot E}$ —provides mechanisms to increase the dissipated energy during fracture.

## Publication III

A. Kirnbauer, C. Spadt, C. M. Koller, S. Kolozsvári, P. H. Mayrhofer

*High-entropy oxide thin films based on Al-Cr-Nb-Ta-Ti*

*Vacuum* (2019) doi: 10.1016/j.vacuum.2019.108850

Single-phase crystalline (Al,Cr,Nb,Ta,Ti)O<sub>2</sub> high-entropy oxide thin films were synthesised at 400 °C by reactive magnetron sputtering of an equimolar Al–Cr–Nb–Ta–Ti-compound target. All the coatings similar chemistry as well as the same rutile structure, even when varying the relative oxygen flow-rate ratio ( $f_{O_2}$ ) from 30 – 80 %. Upon increasing  $f_{O_2}$ , the hardness of the coatings slightly increases from 22 to 24 GPa and their indentation moduli increased from 380 to 410 GPa. Annealing treatments up to 1200 °C and subsequent X-ray diffraction measurements reveal that the coatings stay single-phase crystalline with the rutile structure. The hardness slightly decreases upon annealing to 21 GPa, whereas the indentation modulus increases significantly to  $\sim 450$  GPa. This can

be attributed to the strong 101-texturing occurring upon annealing. Based on our results we can conclude, that the high-entropy effect significantly stabilises our (Al,Cr,Nb,Ta,Ti)O<sub>2</sub> coatings in their rutile structure (being a stable structure for TiO<sub>2</sub>, and a metastable one for CrO<sub>2</sub>, NbO<sub>2</sub>, and TaO<sub>2</sub>).

## Publication IV

A. Kirnbauer, V.Moraes, D.Primetzhofer, M. Hans, J.M. Schneider, P. Polcik, P.H. Mayrhofer

*Thermal stability and mechanical properties of sputtered (Hf,Ta,V,W,Zr)-diborides*

*Manuscript in final preparation*

Within this paper we present single-phase AlB<sub>2</sub>-structured diborides with a high-entropy metal-sublattice, (Hf,Ta,V,W,Zr)B<sub>2</sub>, which were developed by nonreactive magnetron sputtering of a powder-metallurgically prepared diboride target composed of 20 mol% HfB<sub>2</sub>, TaB<sub>2</sub>, VB<sub>2</sub>, W<sub>2</sub>B<sub>5</sub>, and ZrB<sub>2</sub>. The chemical composition, growth morphology (dense fine-fibrous), crystal structure (AlB<sub>2</sub>-type) as well as the mechanical properties ( $E \sim 580$  GPa and  $H \sim 45.4$  GPa) are essentially independent on the applied bias potential ( $U_{\text{bias}} = -40, -60, -80, -100$  V). The B-content obtained by EDS and ERDA is with  $\sim 62$  at.% close to MeB<sub>2</sub> stoichiometry, leading to a configurational entropy of the metal-sublattice of  $1.53 \cdot R$  for the obtained (Hf<sub>0.25</sub>Ta<sub>0.17</sub>V<sub>0.14</sub>W<sub>0.33</sub>Zr<sub>0.11</sub>)B<sub>2</sub>, and thus these coatings can be classified as high entropy ( $> 1.5 \cdot R$ ). *Ab initio* based calculations indicate that the high-entropy metal-sublattice ensures that the (Hf,Ta,V,W,Zr)B<sub>2</sub> is energetically more stable than the decomposition products (Hf,Ta,Zr)B<sub>2</sub> and (V,W)B<sub>2</sub>, which together would have actually a lower energy of formation.

The coatings stay single-phased AlB<sub>2</sub>-structured – with essentially the same lattice parameters and lattice distortions as in the as-deposited state – even when vacuum-annealed at temperatures up to 1300 °C. APT indicates that also the distribution of the elements is random as in the as-deposited state after vacuum-annealed at  $T_a = 1200$  °C. Only after annealing at higher temperatures ( $T_a \geq 1400$  °C) the formation of a separate phase can be detected by XRD, which was proven by APT to be a (V,W)B monoboride with soluted Ta, whereas the remaining matrix is mainly an AlB<sub>2</sub>-structured (Hf,Ta,Zr)B<sub>2</sub> (with soluted V and W). Due to this decomposition the indentation modulus and hardness of our (Hf,Ta,V,W,Zr)B<sub>2</sub> decreased to  $\sim 570$  GPa and  $\sim 39.5$  GPa, respectively, when annealed at 1500 and 1600 °C. As the volume fraction of the newly-formed W-enriched regions with  $T_a = 1400$  °C is rather small, it has almost no influence on the mechanical properties, which are still very high with  $E \sim 610$  GPa and  $H \sim 44.3$  GPa.

Based on our results we can conclude that our (Hf,Ta,V,W,Zr) $B_2$  coatings are superior to binary or ternary diborides on account of their thermal stability and maintained mechanical properties. The high-entropy metal-sublattice guarantees for a maintained severe lattice distortion even when annealed at 1300 °C, allowing for the exceptional high hardness.

## 7.2 Thesis-Related Co-Author Publications

### Publication V

P. H. Mayrhofer, A. Kirnbauer, Ph. Ertelthaler, C. M. Koller

*High entropy ceramic thin films; A case study on transition metal diborides*  
*Scripta Materialia*, doi: 10.1016/j.scriptamat.2018.02.008

Within this work, a first approach on high-entropy diborides was done by synthesising diborides with a high-entropy metal-sublattice. The coatings were prepared by magnetron sputtering using a  $ZrB_2$  target and placing pieces of  $HfB_2$ ,  $TaB_2$ ,  $TiB_2$ , and  $VB_2$ , on the racetrack. As benchmark coatings,  $ZrB_2$  and  $(Zr,Ti)B_2$  coatings were deposited. Subsequently to the deposition, all the coatings were investigated by X-ray diffraction, scanning electron microscopy, and nanoindentation. The XRDs of all the coatings reveal that they crystallise in a single-phase  $\alpha$ -structure ( $AlB_2$ -prototype). The hardness values starting from  $43.2 \pm 1.0$  GPa for  $ZrB_2$  increase to  $44.8 \pm 2.3$  GPa for  $(Zr,Ti)B_2$  and further to  $47.2 \pm 1.8$  GPa for the high-entropy diboride. Upon vacuum annealing at 1100 °C and 1500 °C the high-entropy diboride shows significant boron loss and therefore, additional XRD peaks related to boron depleted phases. The hardness for all the coatings is  $\sim 40$  GPa after annealing at 1100 °C. For  $ZrB_2$  the hardness after 1500 °C is 28 GPa and for  $(Zr,Ti)B_2$  36 GPa, whereas for the HEB the coating spall off the substrate. However, based on the obtained results, we conclude that if B-loss and O-uptake can be limited (or even avoided),  $HEB_2$  can guarantee high thermal stability against decomposition towards their binary or ternary diborides.

## 7.3 Further First Author Publication

### Publication VI

A. Kirnbauer, V. Dalbauer, P. Kutrowatz, S. Kolozsvári, J. Ramm, C. M. Koller, P. H. Mayrhofer

*Oxygen dependent morphology and mechanical properties of AlCr(Fe)-based coatings*  
*Surface and Coatings Technology*, doi.org/10.1016/j.surfcoat.2018.05.041

Al–Cr coatings alloyed with Fe were synthesised by reactive arc evaporation in order to investigate the impact of Fe and the oxygen flow rate during deposition on the structural evolution and mechanical properties of intermetallic as well as substoichiometric oxides (with respect to  $M_2O_3$  stoichiometry).

All intermetallic coatings, prepared in non-reactive conditions, crystallise in a  $\gamma_2$ -type  $Al_8Cr_5$  structure with Fe substitutionally incorporated in the lattice featuring hardness values of around  $11 \pm 1$  GPa. By introducing oxygen to the process, the growth morphology significantly changes from columnar to a nano-composite-like structure consisting of small Cr-enriched crystallites embedded in an amorphous Al-enriched matrix. Simultaneously, the number of droplets and therewith associated defects increases and accordingly the hardness values of these films decrease to  $8.5 \pm 1$  GPa. For higher oxygen flow rates, close to the transition from substoichiometric to stoichiometric sesquioxides ( $\sim 0.7$ – $0.9$  Pa), the crystallinity as well as the fraction of strong oxide bonds increase and leading to the highest hardness values among all coatings investigated ( $> 20$  GPa). Furthermore, small additions (5 – 10 at.%) of Fe to  $Al_{0.7}Cr_{0.3}$  cathodes effectively improve the structural and mechanical properties of substoichiometric oxide films.

## 8 Publications

<b>Publication I:</b> <i>Mechanical properties and thermal stability of reactively sputtered multi-principal-metal Hf-Ta-Ti-V-Zr nitrides</i> .....	72
<b>Publication II:</b> <i>Toughness of Si alloyed high-entropy nitride coatings</i> .....	82
<b>Publication III:</b> <i>High-entropy oxide thin films based on Al-Cr-Nb-Ta-Ti</i> .....	86
<b>Publication IV:</b> <i>Thermal stability and mechanical properties of sputtered (Hf,Ta,V,W,Zr)-diborides</i> .....	92
<b>Publication V:</b> <i>High entropy ceramic thin films; A case study on transition metal diborides</i> .....	103

---

# Publication I



*Mechanical properties and thermal stability of reactively sputtered multi-principal-metal Hf-Ta-Ti-V-Zr nitrides*

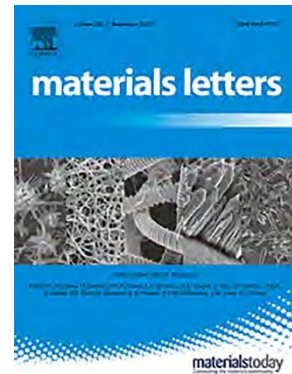
**A. Kirnbauer**, A. Kretschmer, C.M. Koller, T. Wojcik, V. Paneta, M. Hans, J.M. Schneider, P. Polcik, P.H. Mayrhofer

10.1016/j.surfcoat.2020.125674



---

## Publication II



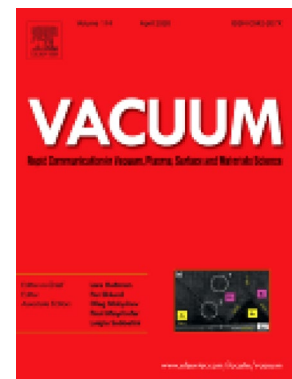
### *Toughness of Si alloyed high-entropy nitride coatings*

R. Hahn, **A. Kirnbauer**, M. Bartosik, S. Kolozsvári, and P.H. Mayrhofer

doi:10.1016/j.matlet.2019.05.074.

---

## Publication III



### *High-entropy oxide thin films based on Al-Cr-Nb-Ta-Ti*

**A. Kirnbauer, C. Spadt, C. M. Koller, S. Kolozsvári, P. H. Mayrhofer**

*10.1016/j.vacuum.2019.108850*

---

## Publication IV

*Thermal stability and mechanical properties of sputtered (Hf,Ta,V,W,Zr)-diborides*

**A. Kirnbauer, V. Moraes, D. Primetzhofer, M. Hans, J. M. Schneider, P. Polcik, P. H. Mayrhofer**

Manuscript in final preparation

(manuscript in final preparation)

## Thermal stability and mechanical properties of sputtered (Hf,Ta,V,W,Zr)-diborides

A. Kirnbauer<sup>a,\*</sup>, V. Moraes<sup>a</sup>, D. Primetzhofer<sup>b</sup>, M. Hans<sup>c</sup>, J.M. Schneider<sup>c</sup>, P. Polcik<sup>d</sup>, P.H. Mayrhofer<sup>a</sup>

<sup>a)</sup> Materials Science and Technology, TU Wien, 1060 Vienna, Austria

<sup>b)</sup> Department of Physics and Astronomy, Uppsala University, 75120 Uppsala, Sweden

<sup>c)</sup> Materials Chemistry, RWTH Aachen University, Kopernikusstrasse 10, 52074 Aachen, Germany

<sup>d)</sup> Plansee Composite Materials GmbH, Siebenbürgerstrasse 23, 86983 Lechbruck am See, Germany

### Abstract

Nonreactive magnetron sputtering of a diboride target composed of TaB<sub>2</sub>, HfB<sub>2</sub>, VB<sub>2</sub>, W<sub>2</sub>B<sub>5</sub>, and ZrB<sub>2</sub> with equimolar composition leads to the formation of crystalline single-phase solid-solution diboride thin films, (Hf,Ta,V,W,Zr)B<sub>2</sub>, with a high-entropy metal-sublattice. Their growth morphology (dense and fine-fibrous), crystal structure (AlB<sub>2</sub>-type), as well as mechanical properties (indentation modulus E of ~580 GP and hardness H of ~45.4 GPa), and chemical compositions are basically independent on the bias potential applied (varied between -40 and -100 V) during the deposition at 450 °C.

Detailed X-ray diffraction (XRD) and atom probe tomography (APT) studies indicate that our (Hf,Ta,V,W,Zr)B<sub>2</sub> thin films remain single-phase AlB<sub>2</sub>-structured (with random distribution of the elements) during vacuum-annealing at temperatures up to 1200 °C. Only when increasing the annealing temperature to 1400 °C, the formation of small orthorhombic structured (V,W)B-based regions can be detected, indicating the onset of decomposition of our (Hf,Ta,V,W,Zr)B<sub>2</sub> thin films. This leads to a decrease in H to ~39.5 GPa with T<sub>a</sub> = 1500 and 1600 °C. After annealing at 1400 °C the hardness is still very high with ~44.3 GPa, as the volume fraction of the newly formed W-enriched domains is small and the majority of the coating is still solid-solution (Hf,Ta,V,W,Zr)B<sub>2</sub> with a severe lattice distortion.

\*) electronic mail: [alexander.kirnbauer@tuwien.ac.at](mailto:alexander.kirnbauer@tuwien.ac.at)

Keywords: high-entropy alloys (HEAs), high entropy diborides, magnetron sputtering, multi-element diborides, thermal stability

### 1 Introduction

The demand for materials able to withstand high temperatures and mechanical loads is tightly connected with new technological developments. Therefore, these are in focus of many research activities. The development of protective thin film materials has the advantage of combining basic materials science concepts with the huge and versatile variety in process conditions accessible through physical vapor deposition (like magnetron sputtering). A relatively new alloying concept – equiatomic multicomponent alloys with at least five principal elements – was introduced by Cantor in 2004 [1]. As these alloys exhibit a configurational entropy  $\Delta S_{\text{conf}}$  of  $> 1.5 \cdot R$ , with R being the universal gas constant, the term high-entropy alloys (HEA) was introduced by Yeh et al. [2] also in 2004. We want to mention that it is probably not the high configurational entropy per se that leads to significantly improved materials properties like strength, toughness, thermal stability, and oxidation resistance. But only if the single-phase alloy (or its matrix) is composed of at least 5 principal elements (leading to  $\Delta S_{\text{conf}} > 1.5 \cdot R$ ) they outperform conventional alloys (which are typically based only on 1, 2, or 3 principal elements). Connected with this condition (at least 5 principal elements) is not just a high configurational entropy but also a severe lattice distortion, a sluggish diffusion, and a cocktail effect (cumulative properties and positive deviation from the

arithmetic mean value, i.e., like a cocktail being more colourful and arched or more colourful and tastier than its components). Together, these form the often cited four core effects of high-entropy alloys.

In addition to HEAs a corresponding high-entropy concept is also applied to ceramic materials including borides, carbides, oxides, and nitrides. Generally, ceramics are considered as high-entropy materials if they consist of five binary ceramics, or more precisely if they have a high-entropy metal-sublattice [3]. Based on this concept, borides, carbides, and oxides in bulk form have been studied regarding their mechanical properties, thermal stability, and oxidation resistance. Also these often show significantly improved materials characteristics compared to their constituting binary materials [4–10]. Later, such a high-entropy concept for ceramic materials was also applied to thin films. First investigations concentrated on (Al,Cr,Ta,Ti,Zr)N coatings. These actually showed only a slight dependence of their structural and mechanical properties on varying the deposition parameters such as reactive gas flow, substrate bias potential, and substrate temperature [11–13]. Additionally, this material system shows excellent thermal stability and diffusion barrier abilities for Cu [14]. Studies on high-entropy thin films include also the investigations of amorphous or crystalline oxides with good mechanical properties and high thermal stability [15,16]. Recent investigations on diborides highlighted

the potential in improving also this sort of thin film materials through the high-entropy concept [17].

Here we discuss in detail the chemical and structural development and mechanical properties of single-phase solid-solution (Hf,Ta,V,W,Zr) $B_2$  developed by nonreactive magnetron sputtering of a powder-metallurgically produced compound target. These show no significant dependence on the bias potential used during deposition, based on investigations by X-ray diffraction (XRD), scanning electron microscopy (SEM), and nanoindentation. Therefore, only the coating prepared with a bias potential of -60 V was further investigated with respect to thermal stability, for which we used detailed XRD, nanoindentation, elastic recoil detection analysis, and atom probe tomography (APT).

## 2 Experimental and methods

The (Hf,Ta,V,W,Zr) $B_2$  thin films were deposited by unbalanced nonreactive magnetron sputtering with a modified Leybold Z400 deposition system using four different bias potentials ( $U_{\text{bias}} = -40, -60, -80, -100$  V). We used one powder-metallurgically produced 3-inch composite diboride target consisting of 20 mol% Hf $B_2$ , Ta $B_2$ , V $B_2$ , W $B_2$ , and Zr $B_2$ . The target-to-substrate distance (in a parallel concentric arrangement) is 6 cm. The substrates (polycrystalline Al $_2$ O $_3$  and sapphire (1 $\bar{1}02$ ) platelets, and low alloyed steel foil) were ultrasonically cleaned in acetone and ethanol for 10 min each prior to loading to the deposition chamber. After reaching a base pressure of  $\leq 3$  mPa they were Ar-ion etched with -150 V pulsed DC at an Ar gas pressure of 1.3 Pa. During deposition, the substrate temperature ( $T_s$ ) was 450 °C, the Ar gas pressure was 0.35 Pa (Ar gas flow rate of 30 sccm), the DC sputter power density was 4.7 W/cm $^2$ , and the substrate bias potentials were either -40, -60, -80, or -100 V. If we assume an average melting temperature  $T_m$  of around 3240 K (from a linear interpolation of all corresponding diborides [18–22]), the 450 °C ( $\sim 723$  K) substrate temperature yields an homologues temperature ( $T_s/T_m$ ) of  $\sim 0.22$ .

Fracture cross sections of our coatings are studied with a FEI Quanta 200 scanning electron microscope (SEM) – equipped with a field emission gun (FEG) and operated at an acceleration voltage of 10 keV – for their growth morphology. Their chemical composition was obtained by top-view investigations via energy dispersive X-ray spectroscopy (EDS) using a FEI Philips XL30 SEM equipped with an EDAX EDS detector. Especially the boron content (but also the metal content) was additionally evaluated for the sample prepared with -60 V bias potential by time-of-flight elastic recoil detection analysis (TOF-ERDA) with a recoil detection angle of 45 ° using a 36 MeV I $^{8+}$  ion beam. This coating was studied in its as-deposited state as well as after the 10-min-vacuum-annealing at 1200, 1400, and 1600 °C (next but one paragraph) by TOF-ERDA.

Coatings on sapphire substrates as well as coating materials removed from their low alloy steel foil substrates (by chemically dissolving the foil with a diluted HNO $_3$ ) are characterized by X-ray diffraction (XRD) using a

PANalytical XPert Pro MPD ( $\theta$ - $\theta$  diffractometer) equipped with a Cu-K $_{\alpha}$  ( $\lambda = 1.54$  Å) radiation source. Mechanical properties, indentation moduli  $E$  and hardness  $H$ , of our coatings on sapphire substrates (in their as-deposited state and after vacuum-annealing, next paragraph) were obtained by evaluating nanoindentation load-displacement curves according to Oliver and Pharr [23]. We recorded 45 load-displacement curves (obtained with a UMIS II nanoindentation system) for each measurement point, starting at a load of 32 mN and decreasing the load in 0.5 mN steps down to 10 mN.

Coatings on sapphire substrates as well as powdered free-standing coating material (prepared with -60 V bias potential) were vacuum-annealed in a Centorr LF22-2000 vacuum furnace for 10 min holding time at various annealing temperatures,  $T_a$  (varied between 900 and 1600 °C in 100 °C steps). The heating rate was 20 K/min and the cooling rate (passively, by turning-off the heater) down to 200 °C was  $> 50$  K/min. After these heat treatments the samples were again investigated by XRD, nanoindentation, and EDS. This coating ( $U_{\text{bias}} = -60$  V and grown on sapphire) was additionally investigated in its as-deposited state and after vacuum-annealing at 1400 °C by cross-sectional transmission electron microscopy (TEM) and selected area electron diffraction (SAED), for which we used a TECNAI F20 FEG TEM operated at an acceleration voltage of 200 keV.

Coatings prepared with -60 V bias potential are studied in detail for their chemical homogeneity in their as-deposited state and after vacuum-annealing at 1200, 1400, and 1600 °C with atom probe tomography (APT). We used a CAMECA local electrode atom probe 4000 XHR to obtain three-dimensional spatially-resolved chemical composition analysis at the nanometre scale of these samples, (Hf,Ta,V,W,Zr) $B_2$ . Laser-assisted field evaporation was employed with 50 pJ laser pulse energy, 200 kHz laser pulse frequency, 60 K base temperature and 1.0% average detection rate. The required specimen shape was obtained by focused ion beam (FIB) milling [24], during which the region of interest was protected with a 350-nm-thin Pt layer against Ga implantation.

The energy of formation of (Hf,Ta,V,W,Zr) $B_2$ , (Hf,Ta,Zr) $B_2$ , and (V,W) $B_2$  in their Al $B_2$  prototype structure [space group 191 (P6/mmm), shortly  $\alpha$ -type structure] is obtained by density functional theory (DFT) calculations employing the Vienna Ab Initio Simulation Package (VASP) [25]. Structure optimization is obtained by applying the projector augmented wave method within the GGA suggested by Perdew, Burke, Ernzerhof [26], of solid solutions treated with the special quasirandom structure approach (applying the ATAT simulation package [27]). Energy cutoff and k-point mesh were chosen carefully, to ensure energy convergence of a few meV/at, for all calculations of the 3x3x3 supercells (containing 81 atoms).



### 3 Results and discussions

The EDS obtained chemical compositions of our (Hf,Ta,V,W,Zr) diboride coatings suggest an almost MeB<sub>2</sub> stoichiometry with boron contents between 65 and 66 at.%, independent of the bias potential used, Fig. 1. The additional ERDA of the sample prepared with  $U_{bias} = -60$  V reveals  $63 \pm 1.7$  at.% B, in excellent agreement with EDS. The contents of the metallic elements are  $\sim 12$  at.% W,  $\sim 9$  at.% Hf,  $\sim 6$  at.% Ta,  $\sim 5$  at.% V, and  $\sim 4$  at.% Zr. Due to the similar energies of W and Zr they are hard to separate by EDS, but ERDA indicates a Zr content of 6.6 at.% and a V content of 7.8 at.%. However, by ERDA the elements Hf, Ta, and W (neighbours in the periodic table) are difficult to separate.

The individual samples show chemical compositions within the error of measurement; therefore, we conclude that their chemistry is independent on the bias potential used during this investigation. Based on EDS, and normalizing to stoichiometric MeB<sub>2</sub>, our coatings correspond to  $(\text{Hf}_{0.25}\text{Ta}_{0.17}\text{V}_{0.14}\text{W}_{0.33}\text{Zr}_{0.11})\text{B}_2$ . Thus, the configurational entropy  $\Delta S_{conf}$  of the metal-sublattice is  $1.53 \cdot R$ , and our diborides can be classified as high-entropy metal-sublattice diborides (HEB) according to the above-mentioned definition ( $\Delta S_{conf} \geq 1.5 \cdot R$ ). Using the Zr and V contents from ERDA, the configurational entropy of the metal-sublattice is even higher.

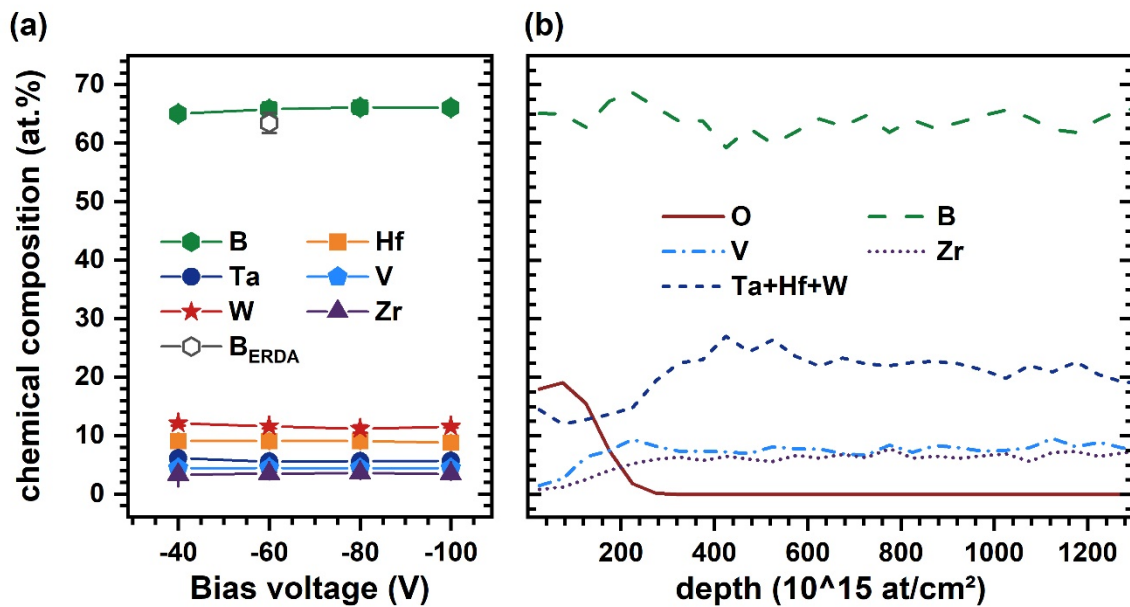


Fig. 1: (a) EDS obtained chemical compositions of our (Hf,Ta,V,W,Zr)B<sub>2</sub> coatings on sapphire substrates, prepared with  $U_{bias} = -40, -60, -80,$  and  $-100$  V. For comparison also the ERDA obtained B content is added for the sample prepared with  $U_{bias} = -60$  V. (b) ERDA obtained depth profile for this sample.

All coatings show a very dense and fine-fibrous growth morphology (independent on the bias potential used, Fig. 2) with a nearly featureless appearance for the ini-

tial growth region at the sapphire substrate. With increasing bias potential from  $-40$  to  $-100$  V the growth rate only slightly decreases from  $\sim 110$  to  $\sim 80$  nm/min.

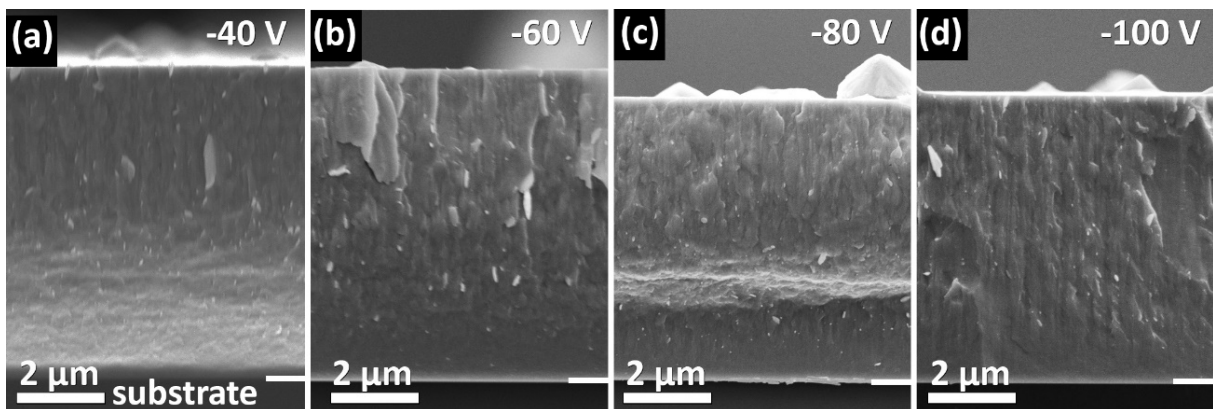


Fig. 2: SEM fracture cross-sections of (Hf,Ta,V,W,Zr)B<sub>2</sub> coatings deposited with  $U_{bias} =$  (a)  $-40$  V, (b)  $-60$  V, (c)  $-80$  V, and (d)  $-100$  V on sapphire substrates.

XRD investigations of our coatings clearly show a single-phased solid-solution diboride with  $\alpha$ -structure, see Fig. 3, which exemplarily shows the XRD patterns of coatings grown on sapphire. For  $U_{\text{bias}} = -40$  V these indicate a preferred 112-orientation growth that changes towards a 111-oriented growth with increasing  $U_{\text{bias}}$  to -100 V, Fig. 3. The XRD peak positions of our high-entropy metal-sublattice diborides (HEB) suggest lattice parameters of  $a = 3.09$  Å and  $c = 3.28$  Å. These are in very good agreement with the linearly interpolation lattice parameters between  $\text{HfB}_2$ ,  $\text{TaB}_2$ ,  $\text{VB}_2$ ,  $\text{WB}_2$ , and  $\text{ZrB}_2$  (from ICDD reference data) – using their above-mentioned mole fractions – which are  $a = 3.08$  Å and  $c = 3.24$  Å.

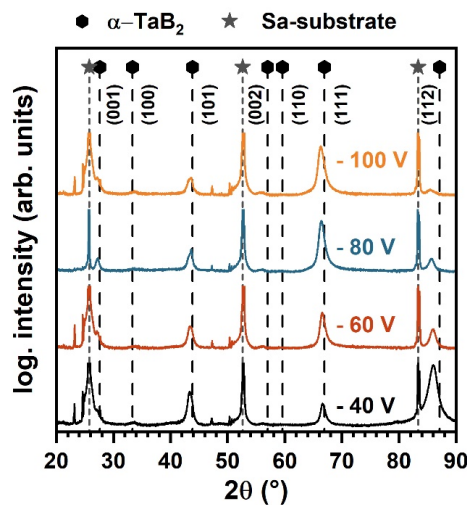


Fig. 3: XRD patterns of  $(\text{Hf,Ta,V,W,Zr})\text{B}_2$  coatings deposited on sapphire substrates with  $U_{\text{bias}} = -40, -60, -80, \text{ and } -100$  V. The  $\alpha$ -structure is indicated by an  $\alpha\text{-TaB}_2$  (ICDD 00-038-1462), substrate peak positions are indicated by grey stars. The peak positions suggest lattice parameters of  $a = 3.09$  Å and  $c = 3.28$  Å.

Indentation moduli  $E$  and hardness  $H$  of our diborides are  $\sim 580$  GPa and  $\sim 45.4$  GPa, respectively, independent on the substrate bias potential applied, Fig. 4. The individual values are within the error of measurement of about  $\pm 20$  GPa for  $E$  and  $\pm 1.5$  GPa for  $H$ . This is because the growth morphology is nearly independent on the bias potential used, and already for a relatively low  $U_{\text{bias}}$  of -40 V a rather dense fine-fibrous growth morphology is obtained, Fig. 2.

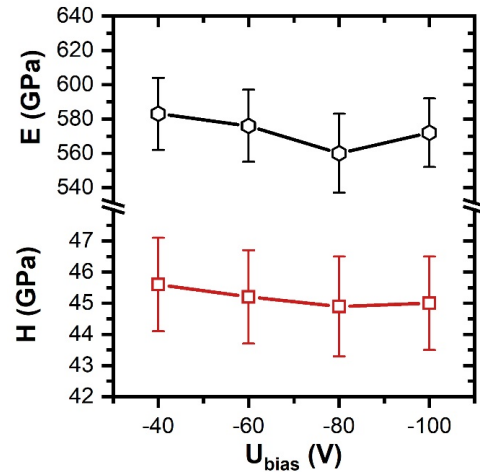


Fig. 4: Indentation modulus  $E$  and hardness  $H$  of our single-phased solid-solution  $(\text{Hf,Ta,V,W,Zr})\text{B}_2$  coatings on sapphire substrates deposited with  $U_{\text{bias}} = -40, -60, -80, \text{ and } -100$  V.

Detailed cross-sectional TEM studies of our coating prepared with  $U_{\text{bias}} = -60$  V clearly confirm the dense fine-fibrous growth morphology, Fig. 5. At the interface to the substrate, their grain size is small, typical for random nucleation, followed by a competitive growth region. But even near to the coating surface, the column diameters are still only about 80 – 100 nm, Fig. 5a.

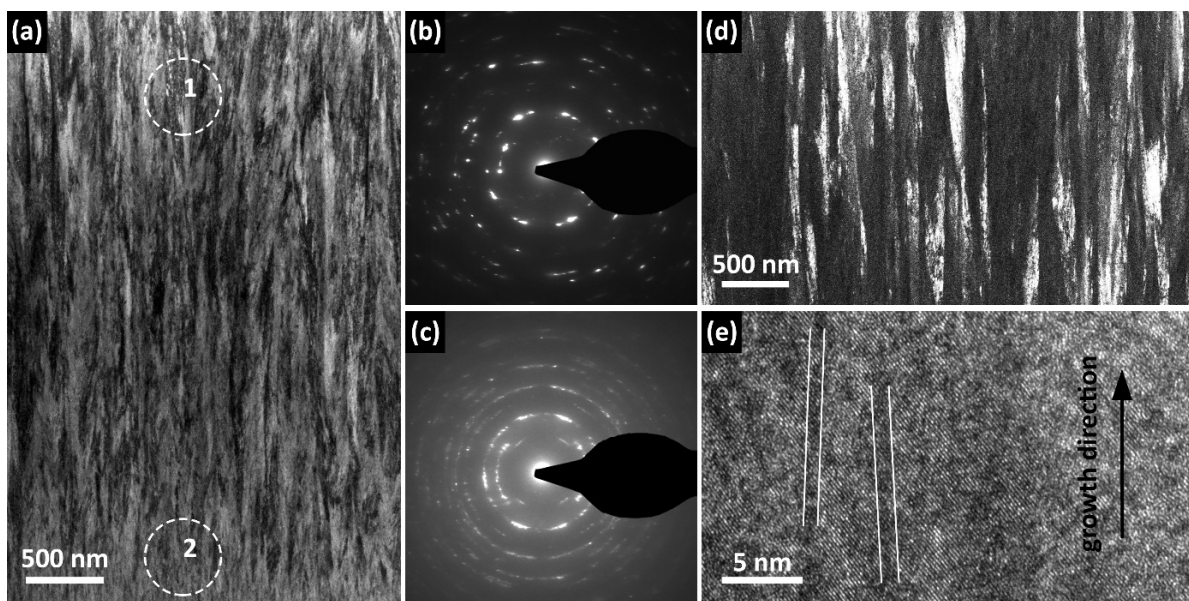


Fig. 5: Cross-sectional TEM investigations of our  $(\text{Hf,Ta,V,W,Zr})\text{B}_2$  deposited with  $U_{\text{bias}} = -60$  V. (a) Bright field TEM image; (b) SAED pattern of area 1 indicated by dashed circle in (a); (c) SAED pattern of area 2 indicated by dashed circle in (a); (d) dark field TEM image; (e) high-resolution TEM image where schematically lower density regions are indicated with white lines.



The corresponding SAED investigations show distinct diffraction spots, Fig. 5b, highlighting the oriented columns with a large aspect ratio. The aperture size is indicated with a dashed circle in Fig. 5a, which is easily exceeded by a column length. Contrary, close to the substrate interface the aperture size covers several column lengths and thus the corresponding SAED pattern is more ring-like rather than having distinct diffraction spots, Fig. 5c. The large aspect ratio of the columns close to the coating's surface is easily seen in the higher resolution dark field TEM image, Fig. 5d, suggesting for  $\sim 1 \mu\text{m}$  long and 50 nm wide columns.

High-resolution TEM investigations reveal that the relatively dense columns are separated by tissue-like phases elongated in growth direction (indicated by white lines in Fig. 5e). A similar (in growth direction elongated) microstructural feature was found for overstoichiometric  $\text{TiB}_2$ , where detailed high-resolution TEM combined with electron energy loss spectroscopy (EELS) line scans indicated these elongated regions as

B-rich tissue phases. This B-rich tissue phase encapsulates  $\sim 5\text{-nm}$ -wide  $\text{TiB}_2$  nanocolumns leading to their highly oriented growth and a hardness above 40 GPa [28]. Therefore, we envision that the darker-contrast regions (aligned in growth direction) could stem from segregated boron also in the HEB films investigated here. However, this requires further detailed high-resolution TEM studies being actually a separate standalone research (out of the focus here).

After vacuum-annealing at  $T_a = 1200, 1400,$  and  $1600 \text{ }^\circ\text{C}$ , our coatings still show the same overall chemical composition as in their as-deposited state, see the ERDA results summarized in Fig. 6a. Even the boron content stays at  $\sim 62 \text{ at.}\%$ , contrary to previous studies on high-entropy diborides or Ti-B-N where a significant B-loss upon vacuum-annealing was on the account of volatile  $\text{H}_3\text{BO}_3$  formation [29,30]. Also, the ERDA depth profile of the coating annealed at  $1200 \text{ }^\circ\text{C}$  suggests only for a small oxygen enriched region near the surface (from residuals of the vacuum-annealing atmosphere).

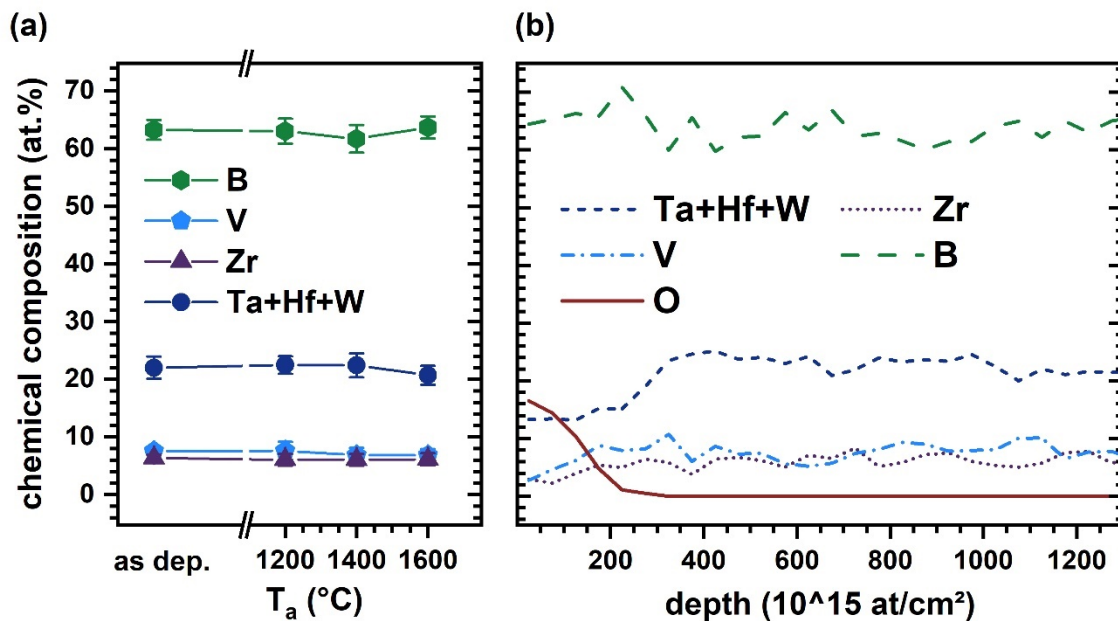


Fig. 6: (a) ERDA obtained chemical composition of our  $(\text{Hf,Ta,V,W,Zr})\text{B}_2$  coating deposited with  $U_{\text{bias}} = -60 \text{ V}$  on sapphire substrates after vacuum-annealing at  $T_a = 1200, 1400,$  and  $1600 \text{ }^\circ\text{C}$ . (b) ERDA obtained depth profile of the sample annealed at  $1200 \text{ }^\circ\text{C}$ .

Nanoindentation measurements of these coatings ( $U_{\text{bias}} = -60 \text{ V}$ , sapphire substrate) after vacuum-annealing also suggest excellent thermal stability, at least up to  $1400 \text{ }^\circ\text{C}$ . Their indentation modulus slightly increases from 580 to 610 GPa upon annealing at  $T_a$  up to  $1400 \text{ }^\circ\text{C}$ , respectively, Fig. 7. If no phase transformation takes place, this indicates that the vacancy content decreases and/or the cohesive strength of grain or column boundary regions increases [30]. Both would be caused by the annealing treatment as thin films prepared by magnetron sputtering (at low homologues temperatures, as in our case) typically exhibit an extensive vacancy content and underdense boundary regions [31]. Further increasing  $T_a$  to  $1500$  and  $1600 \text{ }^\circ\text{C}$  leads to a noticeable reduction in  $E$  to  $\sim 570 \text{ GPa}$ .

The hardness of our  $(\text{Hf,Ta,V,W,Zr})\text{B}_2$  coating initially increases from  $45.4 \pm 1.5$  to  $47.0 \pm 1.6 \text{ GPa}$  upon vacuum-annealing at  $T_a = 900 \text{ }^\circ\text{C}$ . Upon increasing  $T_a$  further to  $1400 \text{ }^\circ\text{C}$  the hardness slightly, but continuously decreases to  $44.3 \pm 2.1 \text{ GPa}$ . Similar to the behaviour of the indentation modulus, also the hardness shows a more distinct reduction upon further increasing  $T_a$  to  $1500$  and  $1600 \text{ }^\circ\text{C}$ . After which the hardness was "only" about  $39.5 \text{ GPa}$ , see Fig. 7.

These results indicate that a relatively small grain size and a high defect density (point defects due to the high-entropy metal-sublattice, the corresponding XRD studies are presented later, and dislocations) is maintained leading to the preserved superhardness ( $H \geq 40 \text{ GPa}$ )



up to  $T_a = 1400$  °C. Thermally-induced recovery effects may essentially influence the vacancy content (to reach thermal equilibrium) and underdense boundary regions upon which the indentation modulus and hardness even increase up to  $T_a = 1400$  °C. The more distinct decrease in  $E$  and  $H$  upon annealing at  $T_a = 1500$  and  $1600$  °C is due to the decomposition of our high-entropy metal-sublattice diboride,  $(\text{Hf,Ta,V,W,Zr})\text{B}_2$ , towards a  $(\text{Hf,Ta,Zr})\text{B}_2$  diboride and  $(\text{V,W})\text{B}$  monoboride (the corresponding XRD studies are presented later). The binary  $\text{ZrB}_2$  or ternary  $(\text{Zr,Ti})\text{B}_2$  (prepared with the same deposition equipment) show a significantly lower thermal stability, with a more pronounced impact of the annealing temperature especially on the hardness [29].

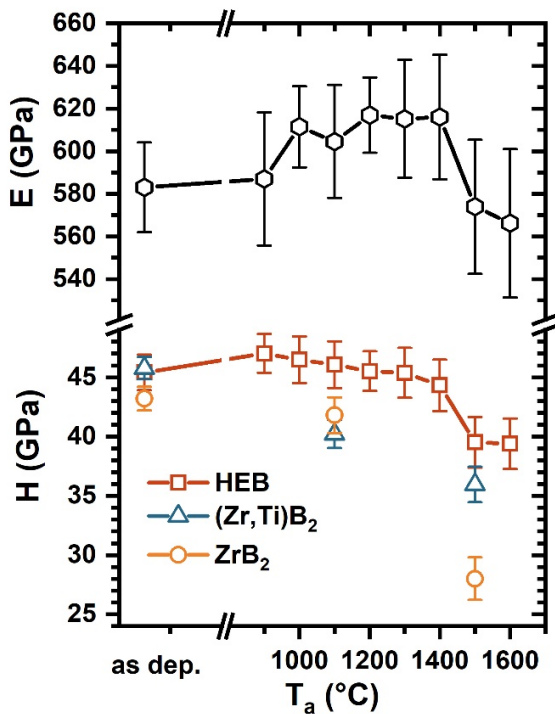


Fig. 7: Indentation modulus  $E$  and hardness  $H$  of our  $(\text{Hf,Ta,V,W,Zr})\text{B}_2$  (HEB) deposited with  $U_{\text{bias}} = -60$  V on sapphire substrates after vacuum-annealing at  $T_a = 900, 1000, 1100, 1200, 1300, 1400, 1500,$  and  $1600$  °C for 10 min. For comparison we added the data of  $\text{ZrB}_2$  and  $(\text{Zr,Ti})\text{B}_2$  from Ref. 29.

The high-entropy metal-sublattice helps stabilizing the solid-solution  $(\text{Hf,Ta,V,W,Zr})\text{B}_2$  phase with respect to the diborides  $(\text{Hf,Ta,Zr})\text{B}_2$  and  $(\text{V,W})\text{B}_2$  having actually a lower energy of formation ( $E_f$ ), Fig. 8 (y-axis value for 0 K). This is valid for the equimolar situation as well as the one close to our experimentally obtained chemical composition. The y-axis values at 0K represent the energy of formation of these phases as obtained by *ab initio*. Simply using the configurational entropy (with  $\Delta S_{\text{conf}} = -R \sum_{i=1}^5 x_i \ln x_i$  and  $x_i$  being the molar fraction of the constituting binary diborides) and the energy of formation  $E_f$  of the solid solutions for the mixing enthalpy ( $\Delta H_{\text{mix}}$ ) we obtained the Gibbs free energy of mixing ( $\Delta G_{\text{mix}} = \Delta H_{\text{mix}} - T\Delta S_{\text{conf}}$ ).

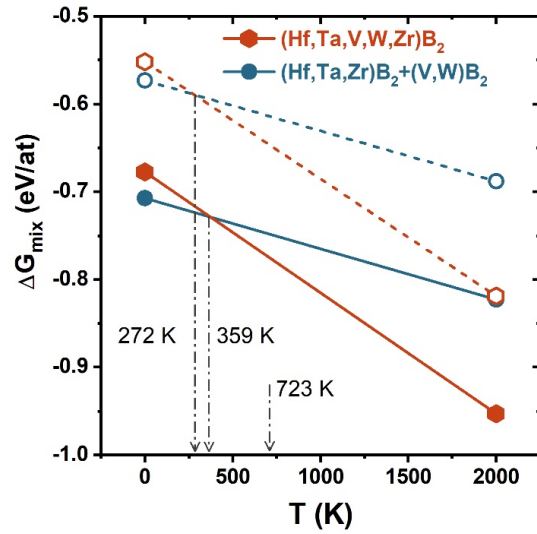


Fig. 8:  $G$  vs.  $T$  curve for a high-entropy metal-sublattice  $(\text{Hf,Ta,V,W,Zr})\text{B}_2$  and the sum of the diborides  $(\text{Hf,Ta,Zr})\text{B}_2$  and  $(\text{V,W})\text{B}_2$ . The latter two actually have a lower energy of formation than  $(\text{Hf,Ta,V,W,Zr})\text{B}_2$ . The solid lines are for an equimolar composition and the dashed lines are for a chemical composition close to our experimentally obtained values (by ERDA and EDS). The substrate temperature during deposition (723 K) is also indicated.

Both scenarios (equimolar as well as that close to our experimentally obtained chemical composition) show that the high-entropy metal-sublattice helps stabilizing the quinary solid-solution diboride (HEB) at elevated temperatures (above 272 K for the experimental chemical composition and 359 K for the equimolar case). Consequently, these *ab initio*-based calculations suggest that as long as the  $\text{MeB}_2$  stoichiometry is maintained, the high-entropy metal-sublattice becomes the more stable one with increasing temperature (being one of the four core effects: entropy stabilization). Important to mention is that upon annealing and especially due to surface reactions with ambient atmosphere also phases with lower or higher boron content can form, which are not considered here. But staying with the material class (here diborides) the high-entropy concept is beneficial in stabilising the solid solution. These calculations (leading to Fig. 8) clearly show that already at the deposition temperature the formation of a solid-solution  $(\text{Hf,Ta,V,W,Zr})\text{B}_2$  with a high-entropy metal-sublattice is clearly preferred over the corresponding diborides (not shown, but these even have a less negative energy of formation than our HEB, thus lose already by their mixing enthalpy) and the sum of the lower-enthalpy  $(\text{Hf,Ta,Zr})\text{B}_2$  and  $(\text{V,W})\text{B}_2$ . But even if that is not the case, through PVD, metastable and supersaturated phases are easily accessible due to the restricted kinetics (especially if the homologues temperature is low, as in our case).

Detailed XRD studies of our powdered free-standing coating material after the individual vacuum-annealing

treatments allow drawing a picture of their thermal stability and decomposition processes, Fig. 9. In the as-deposited state, the pattern clearly shows a single-phase solid solution with  $AlB_2$ -prototype structure having lattice parameters of  $a = 3.09 \text{ \AA}$  and  $c = 3.28 \text{ \AA}$ . Exactly the same as obtained for this coating grown on sapphire substrates (Fig. 3), but here no preferred growth orientation can be detected as we analysed powdered coating material. The latter is essential to minimize (actually completely avoid) detrimental substrate interference and interactions during annealing at these rather high temperatures up to  $1600 \text{ }^\circ\text{C}$ . The coatings remain single-phased up to  $T_a = 1300 \text{ }^\circ\text{C}$  and also the XRD peak positions and shapes are relatively unaffected, suggesting for constant lattice parameters and lattice distortions.

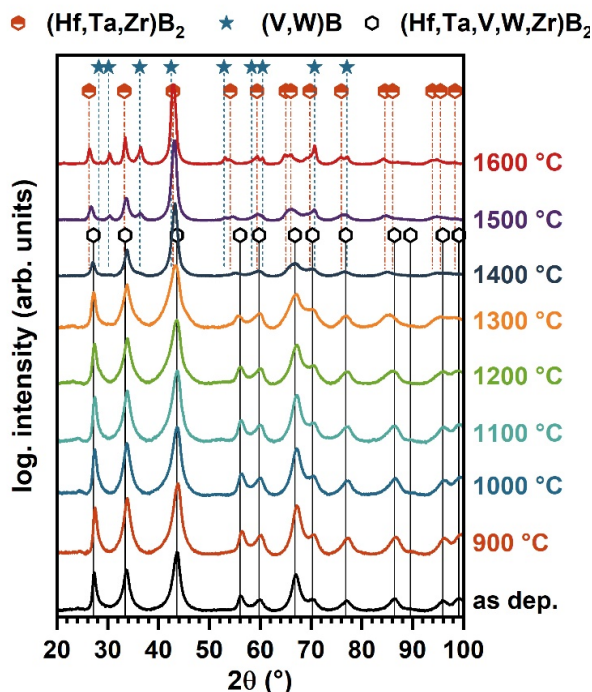


Fig. 9 XRD patterns of vacuum-annealed (at different temperatures, indicated next to the individual patterns) powdered free-standing coating material. The empty black hexagons indicate the XRD peak positions for an  $AlB_2$ -structure with lattice parameters of  $a = 3.09 \text{ \AA}$  and  $c = 3.28 \text{ \AA}$ . The half-filled red hexagons indicate the XRD peak positions for an  $AlB_2$ -structure with lattice parameters of  $a = 3.11 \text{ \AA}$  and  $c = 3.39 \text{ \AA}$ . Based on APT investigations (presented later) this structure is labelled with  $(Ta,Zr,Hf)B_2$ . The blue stars mark the XRD peak positions for an orthorhombic structure with lattice parameters of  $a = 3.16 \text{ \AA}$ ,  $b = 8.41 \text{ \AA}$ , and  $c = 3.06 \text{ \AA}$ , which is labelled with  $(V,W)B$ , also based on the APT investigations (presented later).

Only when increasing  $T_a$  further to  $1400 \text{ }^\circ\text{C}$  the formation of additional small XRD peaks at diffraction angles of  $\sim 30$  and  $\sim 33$  deg can be detected. After annealing at even higher temperatures these small XRD peaks further increase in intensity and additional ones can be detected (see the pattern for  $T_a = 1600 \text{ }^\circ\text{C}$ ), from which it was possible to identify the crystal structure. The additional XRD peaks (indicated by blue stars in Fig. 9) suggest the formation of an orthorhombic structure

with lattice parameters of  $a = 3.16 \text{ \AA}$ ,  $b = 8.41 \text{ \AA}$ , and  $c = 3.06 \text{ \AA}$ . Detailed APT investigations (presented later) indicate a separation of our high-entropy metal-sublattice  $(Hf,Ta,V,W,Zr)B_2$  towards  $(Ta,Zr,Hf)B_2$  and  $(V,W)B$  upon annealing at  $T_a \geq 1400 \text{ }^\circ\text{C}$ . Therefore, we used the WB reference pattern (ICDD 00-006-0541) and slightly modified the lattice parameter [considering the formation of a solid-solution  $(V,W)B$ ], which perfectly matches the additional XRD peaks. Simultaneously with the formation of this new phase, the XRD peak positions of the solid-solution  $AlB_2$ -structure shift to lower diffraction angles. Based on detailed APT investigations (presented later) we named the remaining matrix  $(Ta,Zr,Hf)B_2$ . The XRD peak positions of this solid solution suggests for lattice parameters of  $a = 3.11 \text{ \AA}$  and  $c = 3.39 \text{ \AA}$  (indicated by half-filled red hexagons in Fig. 9). The interpolated lattice parameters, according to ICDD reference data of  $TaB_2$ ,  $ZrB_2$ , and  $HfB_2$  (using mole fractions relevant for our chemical composition) are with  $a = 3.13 \text{ \AA}$  and  $c = 3.41 \text{ \AA}$  in excellent agreement.

Even after annealing at  $1400 \text{ }^\circ\text{C}$  – where already first indications for a phase separation of our solid-solution  $(Hf,Ta,V,W,Zr)B_2$  could be detected by XRD – the coating (for this study we used a coated sapphire substrate) still shows a dense fine-fibrous growth morphology. This is very similar to the as-deposited state (compare Fig. 10a and Fig. 5a). However, the TEM investigations suggest that the microstructural feature (being elongated in growth direction and presumably caused by boron segregation, already present in the as-deposition state) is more distinct after annealing at  $1400 \text{ }^\circ\text{C}$ , see Fig. 10b and especially the higher magnification inset. Although with  $T_a = 1400 \text{ }^\circ\text{C}$ , detailed XRD studies indicated already the onset of the formation of an additional phase (Fig. 9) no such formation could be identified during TEM and SEAD investigations. Also the columnar structure is not influenced suggesting that their volume fraction is very small, too small to be detected by SAED (not shown).

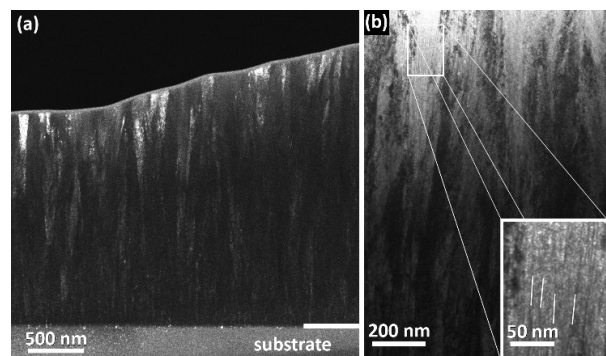


Fig. 10: Cross-sectional TEM investigations of  $(Hf,Ta,V,W,Zr)B_2$  on sapphire substrates after vacuum-annealing at  $1400 \text{ }^\circ\text{C}$ . (a) Dark field TEM image and (b) bright field TEM image with a higher resolution inset illustrating the more distinct (as compared to the as-deposited state) nanocolumnar structure elongated in growth direction.



Detailed APT investigations of powdered free-standing coating material show a random distribution of the elements in the as-deposited state, represented by the reconstructed W atomic positions in Fig. 11a. Also, after annealing at 1200 °C the distribution of elements is still random, whereas with  $T_a = 1400$  °C the formation of W-enriched clusters can be detected by APT. The concentration profile of the elements after annealing at 1400 °C, Fig. 11b, shows that especially Hf follows the profile of Zr, and V follows the profile of W. Tantalum is somehow ambivalent as it follows the Zr as well as W profiles. Further characteristic is that with increasing W content also the B content decreases, leading to the

formation of an almost monoboride with MeB stoichiometry. Annealing at an even higher temperature ( $T_a = 1600$  °C) causes the growth of these W-enriched regions indicating proceeding decomposition of our (Hf,Ta,V,W,Zr) $B_2$  solid solution. Basically, those regions with the highest W content show no Hf or Zr but an enrichment in V, Fig. 11c. Tantalum is as well present in these regions, however, with an opposing profile to V. Whereas the Ta content is higher in the remaining matrix than in the newly formed W-enriched regions (in which Zr and Hf are essentially not soluted), the V content is higher in these newly formed regions than in the remaining matrix.

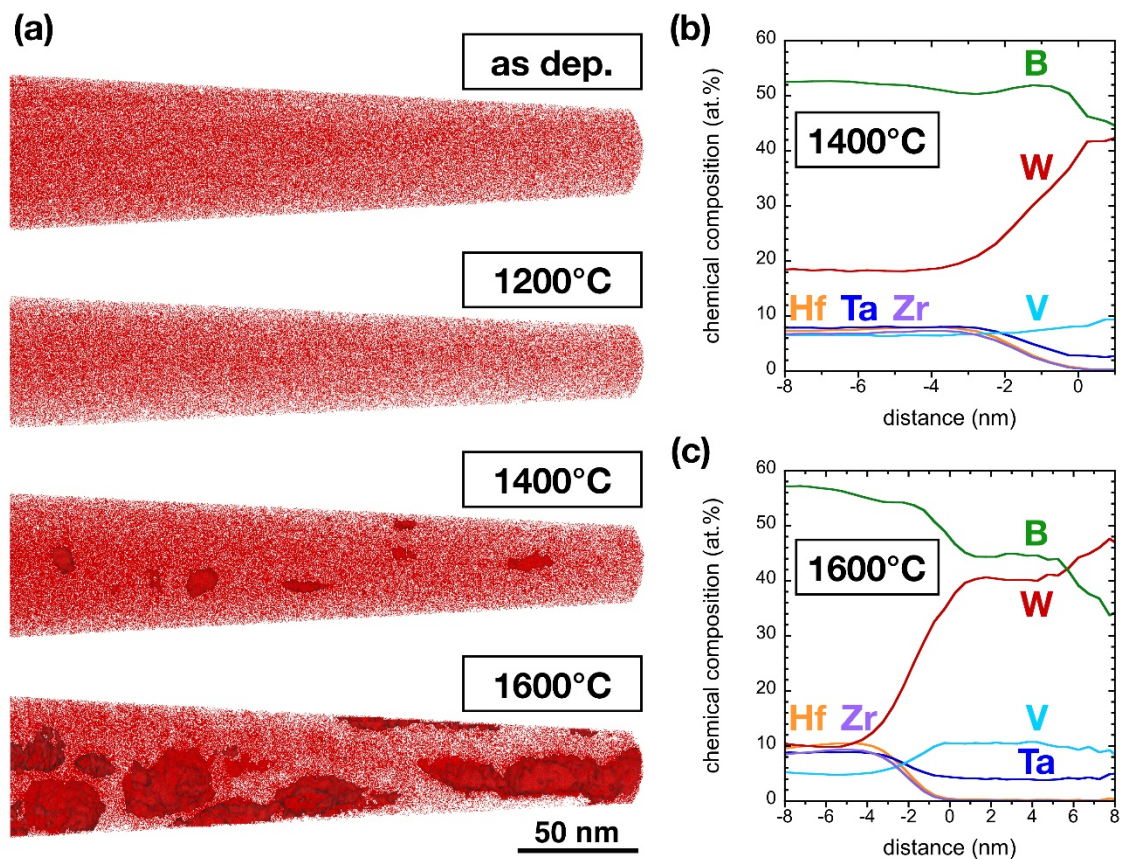


Fig. 11: Local element distribution of  $(\text{Hf,Ta,V,W,Zr})\text{B}_2$  at the nanometer scale. a) Reconstruction of W atomic positions for the as deposited thin film as well as after annealing at  $T_a = 1200, 1400$  and  $1600^\circ\text{C}$ . W-rich regions are indicated by isoconcentration surfaces with  $\geq 35$  at.%. b) Proximity histogram of W-rich regions after annealing at  $T_a = 1400^\circ\text{C}$ . c) Proximity histogram of W-rich regions after annealing at  $T_a = 1600^\circ\text{C}$ .

Based on these investigations we identified the remaining matrix primarily as  $(\text{Ta,Zr,Hf})\text{B}_2$  (with soluted V and W) and the newly formed regions as  $(\text{V,W})\text{B}$  (with soluted Ta). Again we want to highlight that the W-enriched regions exhibit a lower B content, with close to MeB stoichiometry, whereas the B content of the remaining matrix,  $(\text{Ta,Zr,Hf})\text{B}_2$ , is essentially close to the original  $\text{MeB}_2$  stoichiometry. Remarkably now is that ERDA indicates no B-loss due to annealing at 1400 or 1600 °C, see Fig. 6a. Hence, the overall B content is still at the original value of ~62 at.%. This would support the formation of B-rich tissue phases, as indicated

by the TEM investigation of the 1400 °C annealed sample. As these are elongated in growth direction they could be missed by the concentration profile analyses of the APT data (which are taking in the same direction like these regions are elongated).

#### 4 Summary and conclusions

Single-phase  $\text{AlB}_2$ -structured diborides with a high-entropy metal-sublattice,  $(\text{Hf,Ta,V,W,Zr})\text{B}_2$ , were developed by nonreactive magnetron sputtering of a powder-metallurgically prepared diboride target composed of 20 mol%  $\text{HfB}_2$ ,  $\text{TaB}_2$ ,  $\text{VB}_2$ ,  $\text{W}_2\text{B}_5$ , and  $\text{ZrB}_2$ . Chemical

composition, growth morphology (dense and fine-fibrous), crystal structure (AlB<sub>2</sub>-type), as well as mechanical properties (E ~580 GPa and H ~45.4 GPa) are essentially independent on the bias potential (U<sub>bias</sub> = -40, -60, -80, -100 V) used during their preparation (at a substrate temperature of 450 °C). The EDS and ERDA obtained B content is with ~62 at.% close to MeB<sub>2</sub> stoichiometry. The configurational entropy of the metal-sublattice yields to 1.53·R for our (Hf<sub>0.25</sub>Ta<sub>0.17</sub>V<sub>0.14</sub>W<sub>0.33</sub>Zr<sub>0.11</sub>)B<sub>2</sub>, and thus can be classified clearly as high entropy (> 1.5·R). *Ab initio* based calculations indicate that the high-entropy metal-sublattice ensures that the (Hf,Ta,V,W,Zr)B<sub>2</sub> is energetically more stable than the sum of (Hf,Ta,Zr)B<sub>2</sub> and (V,W)B<sub>2</sub>, which together would have actually a lower energy of formation.

The coatings stay single-phased AlB<sub>2</sub>-structured – with essentially the same lattice parameters and lattice distortions as in the as-deposited state – even when vacuum-annealed at temperatures up to 1300 °C. APT indicates that also the distribution of the elements is random as in the as-deposited state after vacuum-annealed at T<sub>a</sub> = 1200 °C. Only after annealing at higher temperatures (T<sub>a</sub> ≥ 1400 °C) the formation of a separate phase can be detected by XRD, which was proven by APT to be a (V,W)B monoboride with soluted Ta. The remaining matrix is essentially an AlB<sub>2</sub>-structured (Hf,Ta,Zr)B<sub>2</sub> (with soluted V and W). Due to this decomposition, the indentation modulus and hardness of our (Hf,Ta,V,W,Zr)B<sub>2</sub> decreased to ~570 GPa and ~39.5 GPa, respectively, when annealed at 1500 and 1600 °C. The rather small volume fraction of the newly-formed W-enriched regions with T<sub>a</sub> = 1400 °C has almost not influence on the mechanical properties, which are still very high with E ~610 GPa and H ~44.3 GPa.

Based on our results we can conclude that our (Hf,Ta,V,W,Zr)B<sub>2</sub> coatings are superior to binary or ternary diborides on account of their thermal stability and maintained mechanical properties. The high-entropy metal-sublattice guarantees for a maintained severe lattice distortion even when annealed at 1300 °C, allowing for the exceptional high hardness.

### Acknowledgements

This work was partly funded by the Austrian COMET Program (project K2 Xtribology, no. 849109 and project K2 Intribology, no. 872176). The authors acknowledge the use of the X-ray center (XRC) and USTEM at TU Wien. Support by the Swedish research council (Contract No. 821-2012-5144) and the Swedish Foundation for Strategic Research (Contract No. RIF14-0053) supporting accelerator operation is gratefully acknowledged. Plansee Composite Materials GmbH is acknowledged for support with target materials. J.M.S. acknowledges funding from the German research foundation (DFG) within the priority program SPP 2006 CCA-HEA.

### References

- [1] B. Cantor, I.T.H. Chang, P. Knight, A.J.B. Vincent, Microstructural development in equiatomic multicomponent alloys, *Mater. Eng. A.* 375–377 (2004) 213–218. doi:10.1016/j.msea.2003.10.257.
- [2] J.-W. Yeh, S.-K. Chen, S.-J. Lin, J.-Y. Gan, T.-S. Chin, T.-T. Shun, C.-H. Tsau, S.-Y. Chang, Nanostructured High-Entropy Alloys with Multiple Principal Elements: Novel Alloy Design Concepts and Outcomes, *Adv. Eng. Mater.* 6 (2004) 299–303. doi:10.1002/adem.200300567.
- [3] B.S. Murty, J.W. Yeh, S. Ranganathan, High Entropy Alloys, Elsevier, 2014. doi:10.1016/B978-0-12-800251-3.00002-X.
- [4] J. Gild, Y. Zhang, T. Harrington, S. Jiang, T. Hu, M.C. Quinn, W.M. Mellor, N. Zhou, K. Vecchio, J. Luo, High-Entropy Metal Diborides: A New Class of High-Entropy Materials and a New Type of Ultrahigh Temperature Ceramics, *Sci. Rep.* 6 (2016) 2–11. doi:10.1038/srep37946.
- [5] Y. Zhang, W.M. Guo, Z. Bin Jiang, Q.Q. Zhu, S.K. Sun, Y. You, K. Plucknett, H.T. Lin, Dense high-entropy boride ceramics with ultra-high hardness, *Scr. Mater.* 164 (2019) 135–139. doi:10.1016/j.scriptamat.2019.01.021.
- [6] G. Anand, A.P. Wynn, C.M. Handley, C.L. Freeman, Phase stability and distortion in high-entropy oxides, *Acta Mater.* 146 (2018) 119–125. doi:10.1016/j.actamat.2017.12.037.
- [7] A. Sarkar, Q. Wang, A. Schiele, M.R. Chellali, S.S. Bhattacharya, D. Wang, T. Brezesinski, H. Hahn, L. Velasco, B. Breitung, High-Entropy Oxides: Fundamental Aspects and Electrochemical Properties, *Adv. Mater.* 1806236 (2019). doi:10.1002/adma.201806236.
- [8] A. Sarkar, R. Djenadic, D. Wang, C. Hein, R. Kautenburger, O. Clemens, H. Hahn, Rare earth and transition metal based entropy stabilised perovskite type oxides, *J. Eur. Ceram. Soc.* 38 (2018) 2318–2327. doi:10.1016/j.jeurceramsoc.2017.12.058.
- [9] T.J. Harrington, J. Gild, P. Sarker, C. Toher, C.M. Rost, O.F. Dippo, C. McElfresh, K. Kaufmann, E. Marin, L. Borowski, P.E. Hopkins, J. Luo, S. Curtarolo, D.W. Brenner, K.S. Vecchio, Phase stability and mechanical properties of novel high entropy transition metal carbides, *Acta Mater.* 166 (2019) 271–280. doi:10.1016/j.actamat.2018.12.054.
- [10] P. Sarker, T. Harrington, C. Toher, C. Oses, M. Samiee, J.P. Maria, D.W. Brenner, K.S. Vecchio, S. Curtarolo, High-entropy high-hardness metal carbides discovered by entropy descriptors, *Nat. Commun.* 9 (2018) 1–10. doi:10.1038/s41467-018-07160-7.
- [11] C.-H. Lai, M.-H. Tsai, S.-J. Lin, J. Yeh, Influence of substrate temperature on structure and mechanical, properties of multi-element (AlCrTaTiZr)N coatings, 201 (2007) 6993–6998. doi:10.1016/j.surfcoat.2007.01.001.
- [12] C.-H. Lai, S.-J. Lin, J.-W. Yeh, A. Davison, Effect of substrate bias on the structure and properties of multi-element (AlCrTaTiZr)N coatings, *J. Phys. D: Appl. Phys.* 39 (2006) 4628–4633. doi:10.1088/0022-3727/39/21/019.
- [13] C.H. Lai, S.J. Lin, J.W. Yeh, S.Y. Chang, Preparation and characterization of AlCrTaTiZr multi-element nitride coatings, *Surf. Coatings Technol.* 201 (2006) 3275–3280. doi:10.1016/j.surfcoat.2006.06.048.
- [14] S.Y. Chang, M.K. Chen, D.S. Chen, Multiprincipal-element AlCrTaTiZr-nitride nanocomposite film of extremely high thermal stability as diffusion barrier for Cu metallization, *J. Electrochem. Soc.* 156 (2009). doi:10.1149/1.3097186.
- [15] M.I. Lin, M.H. Tsai, W.J. Shen, J.W. Yeh, Evolution of structure and properties of multi-component (AlCrTaTiZr)Ox films, *Thin Solid Films.* 518 (2010) 2732–2737. doi:10.1016/j.tsf.2009.10.142.
- [16] A. Kirnbauer, C. Spadt, C.M. Koller, S. Kolozsvári, P.H. Mayrhofer, High-entropy oxide thin films based on Al–Cr–Nb–Ta–Ti, *Vacuum.* 168 (2019) 108850. doi:10.1016/j.vacuum.2019.108850.
- [17] P.H. Mayrhofer, A. Kirnbauer, P. Ertelthaler, C.M. Koller, High-entropy ceramic thin films; A case study on transition metal diborides, *Scr. Mater.* 149 (2018) 93–97. doi:10.1016/j.scriptamat.2018.02.008.
- [18] P. Rogl, M. Materials Science International Team, Calculated B-Zr phase diagram: Datasheet from MSI Eureka in SpringerMaterials ([https://materials.springer.com/msi/phase-diagram/docs/sm\\_msi\\_r\\_10\\_011534\\_02\\_full\\_LnkDia1](https://materials.springer.com/msi/phase-diagram/docs/sm_msi_r_10_011534_02_full_LnkDia1)), (n.d.). [https://materials.springer.com/msi/phase-diagram/docs/sm\\_msi\\_r\\_10\\_011534\\_02\\_full\\_LnkDia1](https://materials.springer.com/msi/phase-diagram/docs/sm_msi_r_10_011534_02_full_LnkDia1).

A. Kirnbauer, V. Moraes, D. Primetzhofer, M. Hans, J.M. Schneider, P. Polcik, P.H. Mayrhofer, *Thermal stability and mechanical properties of sputtered (Hf,Ta,V,W,Zr)-diborides*, (2020) manuscript in final preparation

- [19] P. Rogl, M. Materials Science International Team, Calculated phase diagram B-W: Datasheet from MSI Eureka in SpringerMaterials ([https://materials.springer.com/msi/phase-diagram/docs/sm\\_msi\\_r\\_10\\_018563\\_02\\_full\\_LnkDia0](https://materials.springer.com/msi/phase-diagram/docs/sm_msi_r_10_018563_02_full_LnkDia0)), (n.d.). [https://materials.springer.com/msi/phase-diagram/docs/sm\\_msi\\_r\\_10\\_018563\\_02\\_full\\_LnkDia0](https://materials.springer.com/msi/phase-diagram/docs/sm_msi_r_10_018563_02_full_LnkDia0).
- [20] P. Rogl, M. Materials Science International Team, The B-V phase diagram: Datasheet from MSI Eureka in SpringerMaterials ([https://materials.springer.com/msi/phase-diagram/docs/sm\\_msi\\_r\\_10\\_011530\\_02\\_full\\_LnkDia2](https://materials.springer.com/msi/phase-diagram/docs/sm_msi_r_10_011530_02_full_LnkDia2)), (n.d.). [https://materials.springer.com/msi/phase-diagram/docs/sm\\_msi\\_r\\_10\\_011530\\_02\\_full\\_LnkDia2](https://materials.springer.com/msi/phase-diagram/docs/sm_msi_r_10_011530_02_full_LnkDia2).
- [21] B. Predel, B - Ta (Boron - Tantalum): Datasheet from Landolt-Börnstein - Group IV Physical Chemistry · Volume 12B: “B - Ba ... Cu - Zr” in SpringerMaterials ([https://doi.org/10.1007/978-3-540-44756-6\\_39](https://doi.org/10.1007/978-3-540-44756-6_39)), (n.d.). doi:10.1007/978-3-540-44756-6\_39.
- [22] B. Predel, B - Hf (Boron - Hafnium): Datasheet from Landolt-Börnstein - Group IV Physical Chemistry · Volume 12B: “B - Ba ... Cu - Zr” in SpringerMaterials ([https://doi.org/10.1007/978-3-540-44756-6\\_17](https://doi.org/10.1007/978-3-540-44756-6_17)), (n.d.). doi:10.1007/978-3-540-44756-6\_17.
- [23] W.C. Oliver, G.M. Pharr, An improved technique for determining hardness and elastic modulus using load and displacement sensing indentation experiments, *J. Mater. Res.* 7 (1992) 1564–1583. doi:10.1557/JMR.1992.1564.
- [24] K. Thompson, D. Lawrence, D.J. Larson, J.D. Olson, T.F. Kelly, B. Gorman, In situ site-specific specimen preparation for atom probe tomography, *Ultramicroscopy*. 107 (2007) 131–139. doi:10.1016/j.ultramicro.2006.06.008.
- [25] G.. Kresse, D. Joubert, From ultrasoft pseudopotentials to the projector augmented-wave method, *Phys. Rev. B - Condens. Matter Mater. Phys.* 59 (1999) 1758–1775. doi:10.1103/PhysRevB.59.1758.
- [26] J.P. Perdew, K. Burke, M. Ernzerhof, Generalized gradient approximation made simple, *Phys. Rev. Lett.* 77 (1996) 3865–3868. doi:10.1103/PhysRevLett.77.3865.
- [27] A. Van de Walle, M. Asta, G. Ceder, The alloy theoretic automated toolkit: A user guide, *Calphad Comput. Coupling Phase Diagrams Thermochem.* 26 (2002) 539–553. doi:10.1016/S0364-5916(02)80006-2.
- [28] P.H. Mayrhofer, C. Mitterer, J.G. Wen, J.E. Greene, I. Petrov, Self-organized nanocolumnar structure in superhard TiB<sub>2</sub> thin films, *Appl. Phys. Lett.* 86 (2005) 1–3. doi:10.1063/1.1887824.
- [29] P.H. Mayrhofer, A. Kirnbauer, P. Ertelthaler, C.M. Koller, High-entropy ceramic thin films: A case study on transition metal diborides, *Scr. Mater.* 149 (2018) 93–97. doi:10.1016/j.scriptamat.2018.02.008.
- [30] P.H. Mayrhofer, C. Mitterer, J.G. Wen, I. Petrov, J.E. Greene, Thermally induced self-hardening of nanocrystalline Ti-B-N thin films, *J. Appl. Phys.* 100 (2006). doi:10.1063/1.2222406.
- [31] A. Anders, A structure zone diagram including plasma-based deposition and ion etching, *Thin Solid Films*. 518 (2010) 4087–4090. doi:10.1016/j.tsf.2009.10.145.

---

# Publication V



*High entropy ceramic thin films; A case study on transition metal diborides*

P. H. Mayrhofer, **A. Kirnbauer**, Ph. Ertelthaler, C. M. Koller

doi: [10.1016/j.scriptamat.2018.02.008](https://doi.org/10.1016/j.scriptamat.2018.02.008).



---

# Dipl.-Ing. Alexander Kirnbauer

**Anschrift:** Friedlbrunnngasse 14  
7301 Deutschkreutz  
**Staatsbürgerschaft:** Österreich  
**Geburtsdatum:** 18. Jänner 1990  
**Telefon:** +43 699 10 55 09 85  
**Email:** alexander.kirnbauer@gmx.at



---

<b>Berufliche Erfahrung</b>	März 2017 – März 2020	TU Wien, Projektassistent Lehrstuhl für Werkstoffwissenschaften
	Juli – September 2016	Forschungs -und Entwicklungsabteilung Plansee Composite Materials GmbH
	April 2013 – Februar 2017	TU Wien, Projektmitarbeiter CD – Labor für anwendungsorientierte Schichtenentwicklung unter der Leitung von Univ.Prof. Dr.mont. Paul Mayrhofer
	August 2012 – September 2012	Forschungs- und Entwicklungsabteilung Ulbrich of Austria GmbH
	Juli 2005 und August 2008	Baugesellschaft Porr AG, Wien Buchhaltung- und IT-Abteilung Ferialpraktikant

---

<b>Ausbildung</b>	März 2017 – April 2020	Doktoratsstudium Maschinenbau Thema Dissertation: High-entropy ceramic thin films synthesised by magnetron sputtering
	April 2015 – Februar 2017	Masterstudium Verfahrenstechnik; Thema Diplomarbeit: Impact of Fe on the oxide phase formation and oxidation behaviour of cathodic arc evaporated Al-Cr films
	Oktober 2010 -April 2015	Bachelorstudium Verfahrenstechnik an der TU Wien, Thema BA-Arbeit: Thermally induced phase transitions of Ta-Al-N coatings
	Juli 2009 – August 2010	Wehrdienst, Eisenstadt Militärmusik
	September 2004 – Juni 2009	HTBLA Eisenstadt Mechatronik, Matura 2009

---

<b>Weiterbildung</b>	November 2015	Innova Training
	Juni 2010	Seminar Teambuilding und Kommunikation
	März 2009	Workshop Präsentationstechnik

---

**Projekt an der HTBLA**      September 2008 – Juni 2009      Entwicklung eines Roboters zur halbautomatischen Reinigung von Rotorblättern an Windkraftanlagen

---

**Kenntnisse und Fähigkeiten**

Sprachen:      Deutsch: Muttersprache  
Englisch: verhandlungssicher

EDV Kenntnisse:      MS Office, Auto CAD, Inventor, Origin, Photoshop

Interessen:      Technik, Sport, Musik,

Freiwillige Tätigkeiten:      Flügelhornist in der Musikkapelle Deutschkreutz

---

**Teilnahme an internationalen Konferenzen**

Vorträge:

**Spring Meeting of the European Materials Research Society 2018**  
Strasbourg; 18.06.2018 - 22.06.2018.  
*Thermal stability of reactively sputtered HfTaTiVZr high-entropy nitride coatings*  
A. Kirnbauer, C.M. Koller, S. Koloszári, P.H. Mayrhofer

**16th International Conference on Plasma Surface Engineering**  
Garmisch-Patenkirchen, 17.09.2018  
*Structure, mechanical properties and thermal stability of reactively sputtered AlTaTiVZr high-entropy nitride coatings*  
A. Kirnbauer, C.M. Koller, S. Koloszári, P.H. Mayrhofer

**46th International Conference on Metallurgical Coatings and Thin Films**  
San Diego, 19.05.2019 – 24.05.2019  
*Structure, mechanical properties and thermal stability of magnetron sputtered HfTaVWZr high-entropy boride coatings*  
A. Kirnbauer, C.M.Koller, P. Polcik, P.H. Mayrhofer

**Materials Research Society- Fall Meeting 2019 (MRS 2019),**  
Boston, 1.12.2019 – 6.12.2019  
*High-entropy ceramic thin films synthesized by magnetron sputtering*  
A. Kirnbauer, P.H. Mayrhofer

Poster Präsentationen:

**46th International Conference on Metallurgical Coatings and Thin Films**  
San Diego, 19.05.2019 – 24.05.2019  
*Multielement rutile-structured AlCrNbTaTi-oxide coatings synthesised by reactive magnetron sputtering*  
A. Kirnbauer, C.M. Koller, S. Koloszári, P.H. Mayrhofer

---



**Auszeichnungen** Young Scientist Award E-MRS Spring Meeting 2018  
*Thermal stability of reactively sputtered HfTaTiVZr high-entropy nitride coatings*

---

**Betreute  
Studenten**

Matthias Selinger	Structure, mechanical properties, and thermal stability of reactively sputtered AlTaTiVZr high-entropy nitride thin films; Bachelor Thesis
Bernhard Girsule	Influence of deposition parameters on structure and mechanical properties of Hf-Ta-Ti-V-Zr-N; Bachelor Thesis
Lena Dorner	Structure, mechanical properties and thermal stability of reactively sputtered (Al,Cr,Nb,Ta,Ti)N thin films; Bachelor Thesis
Christoph Spadt	High-Entropy Oxid-Schichten basierend auf (Al,Cr,Nb,Ta,Ti); Bachelorarbeit